# Effects of Dynamic Material Strength on Hydrodynamic Instability and Damage Evolution in Shock Loaded Copper

by

Sudrishti Gautam

A Thesis Presented in Partial Fulfillment
of the Requirements for the Degree
Master of Science

Approved February 2016 by the
Graduate Supervisory Committee:

Pedro Peralta, Chair
Jay Oswald
Kiran Solanki

ARIZONA STATE UNIVERSITY

May 2016

ABSTRACT

Characterization and modeling of deformation and failure in metallic materials under extreme conditions, such as the high loads and strain rates found under shock loading due to explosive detonation and high velocity-impacts, are extremely important for a wide variety of military and industrial applications. When a shock wave causes stress in a material that exceeds the elastic limit, plasticity and eventually spallation occur in the material. The process of spall fracture, which in ductile materials stems from strain localization, void nucleation, growth and coalescence, can be caused by microstructural heterogeneity. The analysis of void nucleation performed from a microstructurally explicit simulation of a spall damage evolution in a multicrystalline copper indicated triple junctions as the preferred sites for incipient damage nucleation revealing 75% of them with at least two grain boundaries with misorientation angle between $20 - 55°$. The analysis suggested the nature of the boundaries connecting at a triple junction is an indicator of their tendency to localize spall damage. The results also showed that damage propagated preferentially into one of the high angle boundaries after voids nucleate at triple junctions. Recently the Rayleigh-Taylor Instability (RTI) and the Richtmyer-Meshkov Instability (RMI) have been used to deduce dynamic material strength at very high pressures and strain rates. The RMI is used in this work since it allows using precise diagnostics such as Transient Imaging Displacement Interferometry (TIDI) due to its slower linear growth rate. The Preston-Tonks-Wallace (PTW) model is used to study the effects of dynamic strength on the behavior of samples with a fed-thru RMI, induced via direct laser drive on a perturbed surface, on stability of the shock front and the dynamic evolution of the amplitudes and velocities of the perturbation imprinted on the back (flat)

surface by the perturbed shock front. Simulation results clearly showed that the amplitude of the hydrodynamic instability increases with a decrease in strength and vice versa and that the amplitude of the perturbed shock front produced by the fed-thru RMI is also affected by strength in the same way, which provides an alternative to amplitude measurements to study strength effects under dynamic conditions. Simulation results also indicate the presence of second harmonics in the surface perturbation after a certain time, which were also affected by the material strength.

ACKNOWLEDGMENTS

I wish to express my gratitude towards my advisor, Dr. Pedro Peralta for his constant guidance and encouragement. Special thanks to Kapil Krishnan, who's work and guidance helped me in establishing a solid understanding of the project and to Saul Opie who helped me selflessly during the course of my research. I would also like to thank Andrew Brown and Leda Wayne from ASU and Eric Loomis from Los Alamos National Laboratory (LANL) for their contribution towards this project by providing experimental data, which was crucial for my work. I really appreciate my co-workers Jay Patel, Elizabeth Fortin, Jenna Lynch, Robert McDonald and Harn Lim for the countless joyful hours. This work was funded by Los Alamos National Laboratory under the Laboratory Directed Research and Development – Directed Research (LDRD-DR) program, project #20060021DR, by the United States Department of Energy under National Nuclear Security Administration grants # DE-FG52-06NA26169, DE-FG52-10NA29653, and DE-NA0002005, and Office of Fusion Energy Science grant # DE-SC0008683.

TABLE OF CONTENTS

Page

LIST OF TABLES

Table Page

LIST OF FIGURES

# 1. INTRODUCTION

## 1.1. Motivation

Understanding highly complex multi-component devices that experience extreme loading conditions like nuclear weapons is of utmost importance for national security. For the very same purpose, the National Nuclear Security Administration (NNSA) established the Advanced Simulation and Computing (ASC) program in 1995. The ASC's main functions were to provide NNSA with leading edge and high-end simulation capabilities to extend the lifetime of nuclear weapons in the stockpile. The ASC implemented modern advancements in high performance computing (HPC) and super computers to quickly and accurately simulate the results of new nuclear weapon designs and as well as effects of aging on existing nuclear weapons, while adhering to international bans on the testing of such weapons. Along with HPC, the ASC also requires complex numerical simulations to be supplemented by theory, data from past nuclear tests, and new experimental results [1].

To understand the effects of a nuclear blast event, one must understand the physics behind the formation of shock and release waves, and their synergistic interactions with material behavior. Los Alamos National Laboratory (LANL), which is a part of the ASC program, plays a key role in the material characterization and failure modeling in metallic materials under extreme conditions, such as the high loads and strain rates that are typically found during shock loading. Since recreating such drastic condition in a laboratory under controlled environments can be difficult and expensive, development of reliable computational models becomes necessary [1].

When a shock wave causes stresses in a material that exceed the elastic limit; plasticity and eventually spallation occurs in the material [2]. Spall damage depends on a lot of factors such as loading conditions, impact zone, duration of pulse, etc., on a macroscopic scale and microstructure, grain size, intrinsic (grain boundaries, triple points) and extrinsic (precipitates, inclusions) defects on a microscopic scale [2]. Therefore to understand the initiation of spall failure, also known as incipient spall, becomes extremely important as it sheds light on methods that can be implemented to improve materials strength to withstand high dynamic loads.

Experimental results [3-4] have shown that failure mechanisms like trans-granular and inter-granular can cause damage initiation. In particular, the grain boundaries may act as barriers to the propagation of failure modes that originate inside the grains or as sites of damage initiation [4]. Elastic and plastic anisotropy can affect the failure modes by inducing heterogeneous deformation at and around the grain boundary [5]. The study of spall damage nucleation at the incipient stage around the microstructural weak links such as grain boundaries and triple junctions can provide accurate statistical data for the preferred sites of damage nucleation.

In addition to stockpile stewardship of nuclear weapons, other important application require a deep understanding of the synergy between shock waves and material behavior. One of these applications is Inertial Confinement Fusion (ICF), which is a process that attempts to initiate nuclear fusion reactions by heating and compressing a fuel target. However, there is not a successful ignition of an ICF capsule yet and large efforts have been undertaken to study all the different challenges that ICF is facing [6]. Hydrodynamic instabilities, such as Rayleigh-Taylor (RT), destroy the imploding shell of

an ICF capsule and hinder the formation of the central hot spot by prematurely mixing hot and cold fuel [6]. This is one of the most critical challenges that ICF is facing and large efforts have been made by many researchers to mitigate this problem, and effects of material strength might be key to these efforts [6].

Rayleigh-Taylor (RT) and Richtmyer-Meshkov (RM) are two hydrodynamic instabilities where sustained or impulse forces act across a perturbed bimaterial interface. In the RT instability, a less dense material pushes/supports a more dense material, e.g., oil supporting water and once acceleration is sustained, e.g., by gravity, any perturbation on the material interface can lead to exponential perturbation growth [6]. The RT instability requires opposite density and pressure gradients, which can be explained with an example of a vessel containing two immiscible liquids of different densities where the upper fluid is heavier than the lower fluid. When the upper fluid is heavier than the lower one, the small perturbations present in the interface grow rapidly in time introducing RT instability [6]. In the RM instability, an impulse force such as a shock wave passing through a perturbed bimaterial interface can produce a linear perturbation growth when the passage of the shock suddenly distorts the boundary and suddenly produces a non-uniform velocity, causing amplification of perturbation [6]. The RM instability is similar to RT instability; however, the RM instability can also occur when density and pressure gradients have the same sign. This can also be explained for the case of two immiscible liquids of different densities as explained in the RT instability where the density gradients of the two fluids can be either positive or negative [6]. In many applications either one or both materials can be solids, which possess significant strength (resistance to shear) that can significantly change the evolution of perturbation growth from that predicted by

strictly fluid (hydrodynamic) analysis [7-9]. Solids often have strength anisotropy and rate dependence, which can seed perturbations and affect perturbation growth. Many researchers have explored the effect of strength on hydrodynamic instabilities; however, there are still many challenges left for instability modeling.

Recently, many researchers have used RM [12-18] and RT [9-11,16] instability experiments to infer the material strength under dynamic conditions. These experimental techniques are used for material model calibration and validation. The rest of the chapter will help understand different phenomena during shock loading leading to plasticity and spall damage. Fundamentals of shock loading, anisotropic effect, experimental techniques to produce shock loading, strength models to capture plasticity in high strain rate applications and finally mechanisms of spall damage produced due to the shock loading from the localization of plastic strain will be discussed individually.

The following sections will discuss more detail about the different phenomena involved in shock loading that produce hydrodynamic instabilities, strength models to capture the material behavior during shock loading, and spall damage.

## 1.2. Fundamentals of Shock Physics

Materials get locally excited when impacted by a hammer or dropped to the ground, resulting in a wave propagation phenomenon. Once excited, the wave as a disturbance in the material, propagates through the material as a stress wave with a speed given by [2]

$$C = \left(\frac{1}{\rho}\frac{\partial \sigma}{\partial \varepsilon}\right)^{\frac{1}{2}} \tag{1.1}$$

where $C$ is the wave speed, $\sigma$ is the stress, $\varepsilon$ is the resulting strain from the stress wave and $\rho$ is the density of the material. During the propagation of the stress wave, at one point, the amplitude of the stress wave may result in a stress state that greatly exceeds the dynamic strength of the material. Stress waves like this are usually highly dominated by the compressive mean stress component and, therefore, the shear stresses can be neglected. When the component of the mean stress contribution of the mean stress component is predominant, materials can be treated as fluids, i.e., no shear resistance [2]. For an ideal gas, an isentropic process is described by $PV^{\gamma} = \text{constant}$. Differentiating this equation we have [2]

$$\frac{dP}{dV} = -\gamma \frac{P}{V} \tag{1.2}$$

where $P$is the pressure, $V$ is the volume, $\gamma$ is the ideal gas constant, $dP$ and $dV$ are the changes in pressure and volume, respectively.

From the above equation (1.2) we can say that, value of $P/V$ and $|dP/dV|$ increase with pressure. Assuming a disturbance is occurring isentropically, the velocity of the disturbance provided by equation (1.1) is equivalent to $\left(\frac{\frac{dP}{dV}}{\rho}\right)^{1/2}$ for an ideal gas in one-dimensional configuration, which implies that the velocity disturbance is proportional to $\left(\frac{dP}{dV}\right)^{1/2}$ [2]. It can be concluded that a high amplitude isentropic disturbance travels faster than the lower amplitude one, which is an essential requirement for the development of shock waves. Due to this, the disturbance front will 'steepen up' as it travels through the material resulting in the rapid change of pressure. This leads to the shock wave, defined as the discontinuity in pressure, temperature (or internal energy) and density [2].

Also, the geometrical constraints produced by sample shape (thin plate) lead to uniaxial strain condition which in turn result to the convexity of the stress-strain slope [2] given by the equation

$$\left|\frac{d\sigma}{dV}\right| \uparrow \text{ as } \sigma \uparrow \cong \frac{\partial}{\partial \varepsilon}\left(\left.\frac{\partial \sigma}{\partial \varepsilon}\right|_s\right) > 0 \tag{1.3}$$

Equation (1.3) shows that the wave speed increases with pressure, which is an important condition for shock waves to exist. A schematic profile of a shock front is shown in figure 1.1 [19].

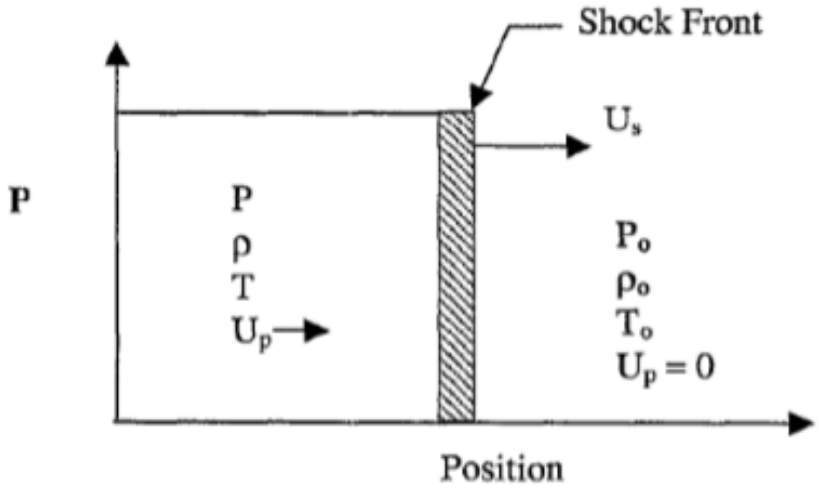


Figure 1.1. Profile of a shock front propagating through a material [19].

where $\rho_0$ is the density of the material at reference state, $\rho$ density of the material at the current state, $U_s$ is the shock velocity, $U_p$ is the particle velocity, $E_0, E,\ P_0$ and $P$ are the energies and pressures at reference and current states, respectively. The subscript $'o'$ indicates the properties of the material ahead of the shock front.

In solids, shock waves exist in three different pressure regimes defined by purely elastic (acoustic), elastic-plastic, and hydrodynamic [2]. The purely elastic regime is

defined as that below the critical pressure at which plasticity occurs and is known as Hugoniot Elastic Limit (HEL) [21]. The elastic-plastic regime consists of both elastic and plastic waves resulting into a combined state of a speed for the wave propagation. This wave structure is known as elastic-plastic wave structure consisting of a leading elastic zone followed by a plastic zone [2]. During the propagation of the stress wave, when the contribution of the mean component of the stress is predominant, shear stresses of the solid can be neglected resulting in the hydrodynamic regime of the shock wave, where the solid can be treated as a fluid and the wave speed is determined by an equation of state (EOS) [2].

In the elastic-plastic regime, the main shock wave is preceded by an elastic wave known as the elastic precursor, which "conditions" the material ahead of the main shock, which usually propagates at a lower speed [2]; therefore, it is important to study and understand the elastic wave. Below the HEL, the wave is elastic in nature and the longitudinal wave velocity $C_l$ at which it propagates is a function of bulk modulus $(K)$, shear modulus $(G)$, and the density $(\rho)$ given by [22]

$$C_l = \left(\frac{K+\frac{4}{3}G}{\rho}\right)^{\frac{1}{2}} \tag{1.4}$$

However, for pressures above the HEL, shear effects can be neglected giving the longitudinal wave speed as a function of bulk modulus and density [22]

$$C_0 = \left(\frac{K}{\rho}\right)^{\frac{1}{2}} \tag{1.5}$$

As mentioned earlier, a shock wave is defined as a discontinuity in pressure, temperature and density where the expressions governing sound wave behavior, i.e.,

acoustic approximations are not valid unless the pressure involves are low. The discontinuity is expressed by Rankine-Hugoniot equations using the conservation of mass, momentum, and energy [2] given by

Conservation of mass: $\rho_0 U_s = \rho\left(U_s - U_p\right)$ (1.6)

Conservation of momentum: $P - P_0 = \rho_0 U_s U_p$ (1.7)

Conservation of Energy: $E - E_0 = \frac{1}{2}(P + P_0)\left(\frac{1}{\rho_0} - \frac{1}{\rho}\right)$ (1.8)

From equations (1.6-1.8), there are five variables: pressure $(P)$, specific volume $(V)$ or density $(\rho)$, energy $(E)$, particle velocity $(U_p)$, and shock wave velocity $(U_s)$. The subscript $'o'$ indicates the properties of the material ahead of the shock front. Hence an additional equation is needed to determine all the parameters as a function of one, which is given by equation (1.9) [2]. Equation (1.9) is expressed as a relationship between shock and particle velocities and was experimentally determined.

$U_s = C_0 + S\,U_p$ (1.9)

where $C_0$ is the wave velocity of the material at zero (low) pressure and $S$ is the slope of the $U_s - U_p$ line that is a function of the material, which is empirically determined. Equation (1.9) is often known as equation of state (EOS) of a material. For metals, equation (1.9) is often linear describing the shock response of material that does not undergo phase transition [2].

When the material is isotropic in nature, equations (1.4-1.5) can be used. However, anisotropic material behavior can affect the wave propagation as it encounters different grains in a polycrystal. The disturbance can propagate with different speeds through different individual grains and also when it encounters the interfaces between

adjacent grains. Many researchers [21,23-25] have studied the effects of anisotropy and other microstructural defects on the propagation of shock wave resulting in significant differences in plasticity and spall. Therefore, it becomes important to study the effects of anisotropy on the propagation of shock waves [21,23-25].

### 1.3. Anisotropy Effects on Shock Wave

Anisotropy is defined by the directional dependence of a property on the applied field [24], resulting in different values of a physical property of a material when measured along different axes. Meyers [21] studied the anisotropy effect on elastic precursors during the shock loading of a polycrystalline cubic material. He noted the presence of irregularities in the rise time of elastic precursor waves when the shock wave is propagating through the grain boundary of a polycrystalline cubic material. There are other effects of anisotropy that change the wave speed such as crystallographic direction, wave refraction at grain boundaries, scattering at grain boundaries and scattering due to mode conversion between longitudinal and shear waves while traversing different grains [21].

As per previous comments, wave velocity changes with the crystallographic orientation. One can take the cubic crystallographic orientations with the highest symmetry, i.e., $< 100 >, < 110 >, \text{and} < 111 >$, the wave speeds of which are different from each other and can be defined as functions of the components of the elastic stiffness tensor $C_{11},\ C_{12}, and\ C_{44}$ and the density of a material, $\rho$ [21]. The longitudinal velocities of these crystallographic orientations are given by [21]

$$C_{<100>} = \left(\frac{C_{11}}{\rho}\right)^{\frac{1}{2}}, C_{<110>} = \left(\frac{C_{11}+C_{12}+2C_{44}}{\rho}\right)^{\frac{1}{2}}, C_{<111>} = \left(\frac{C_{11}+2C_{12}+4C_{44}}{\rho}\right)^{\frac{1}{2}} \quad (1.10)$$

When a longitudinal wave comes across an interface or free surface of a material, reflected and transmitted waves are generated and the wave speed for these waves can vary with crystallographic orientation as given by equation (1.10) [21]. The study done by Meyers for iron [21], he noticed that the wave velocity for an iron along crystallographic directions $< 111 >$ and $< 100 >$ have highest and lowest values respectively. This difference in crystallographic orientation can give rise to mismatch in velocities leading to strain localization, which can be an important phenomenon in plastic deformation and failure produced by shock loading [22]. Figure 1.2 is a surface plot for $C_l^2$ depicting the variation of wave velocities along different crystallographic directions for copper. The distance from the center to the surface is proportional to the longitudinal sound speed along direction defined by the vector joining the two points. Hence, the surface plot shows that grains along the direction $< 100 >$ have the lowest wave speed while those along the direction $< 111 >$ have the highest.

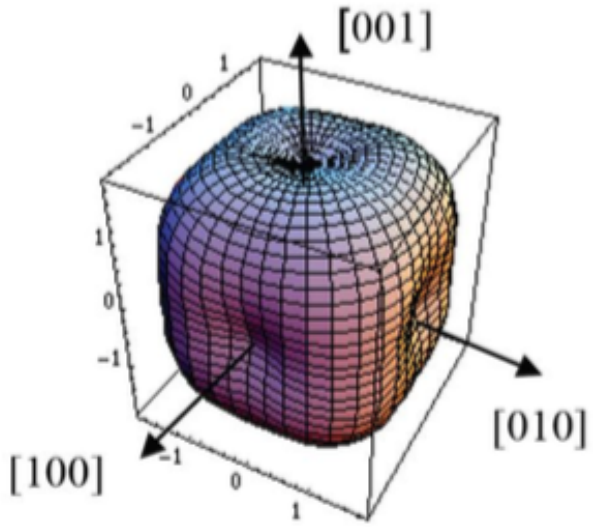


Figure 1.2. Surface plot of $C_l^2$ for copper varying with the crystallographic orientation [25].

Loomis et.al [23] studied the refraction and reflection of elastic waves in NiAl bicrystal grain boundaries using a slowness approach as well as finite element simulations. They calculated amplitude of the longitudinal waves using the slowness method and compared with stresses obtained from a finite element simulation of the bicrystal, and found that the scattering of the elastic waves could lead to stress concentration at the interfaces [23]. This is really important when dealing with strong shock waves as it can lead to localization of strain resulting to damage in many poly-crystalline and multi-crystalline materials.

One of the most common ways to produce a shock wave in a material is the flyer-plate impact test [2, 22]; however, many recent applications have used laser energy to induce shocks. These methods are described briefly in the section below.

## 1.4. Experimental Methods to Study Shock Dynamics

There are many ways to produce shock wave in a material. Traditionally, flyer-plate impact experiments [22] have been conducted to generate shocks, as they lead to uniaxial strain conditions. These tests are used to generate the planar shock waves for dynamic experiments and spall measurements, by impacting a target with a flyer plate [26]. However, such processes have the expected strain rates limited to a maximum of $10^5\ s^{-1}$ [27]. This can be overcome by using high-energy laser short pulses to generate a pressure wave.

Many applications such as ICF use the laser ablation method that produces a shock wave in the material where strain rates can reach up to $10^{12}s^{-1}$ [28]. A typical set-up for the laser ablation is represented by figure 1.3. In this set-up, a laser beam ablates a thin layer on the surface of the sample and as the gas expands off the surface of the specimen, an equal reaction shock wave is generated into the material. As this shock wave propagates through the thickness, conditions for uniaxial strain are similar to those achieved in a flyer-plate impact test, to a very good approximation by maintaining sample width to thickness ratio of at least 10:1 [29]. This uniaxial condition driven by the geometric constraints is usually satisfied only for the center region [29]. At some radial distance from the center, lateral release waves interact with the longitudinal waves and the uniaxial strain conditions are violated. The Aspect ratio (width to thickness) of the sample can be increased to have the radial release waves confined to the circumference [30].

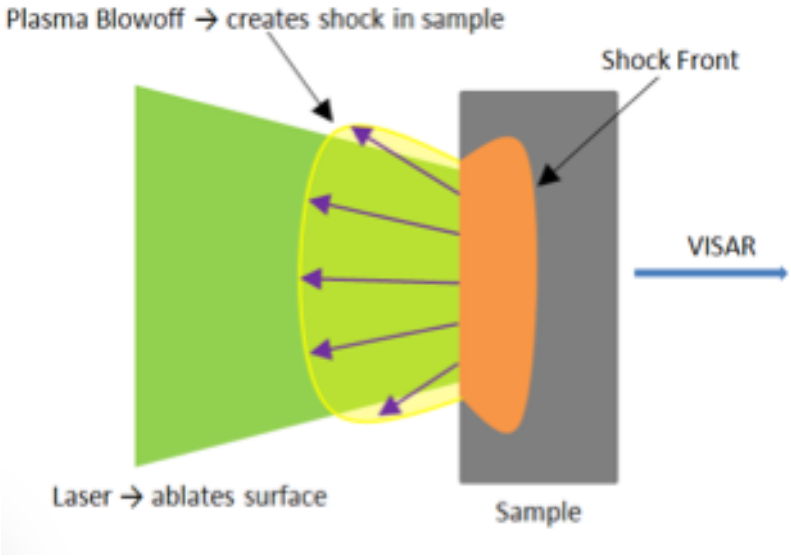


Figure 1.3. Typical laser ablation setup used for shock experiments [31].

Velocity interferometry systems, typically the well-known velocity interferometry system for any reflector (VISAR), are commonly used in many shock experiments to record the dynamic evolution of the free surface of the sample, mainly through particle velocity measurements [32]. A typical VISAR dataset depicting the evolution of particle velocity at a free surface of a shocked sample is shown in figure 1.4.

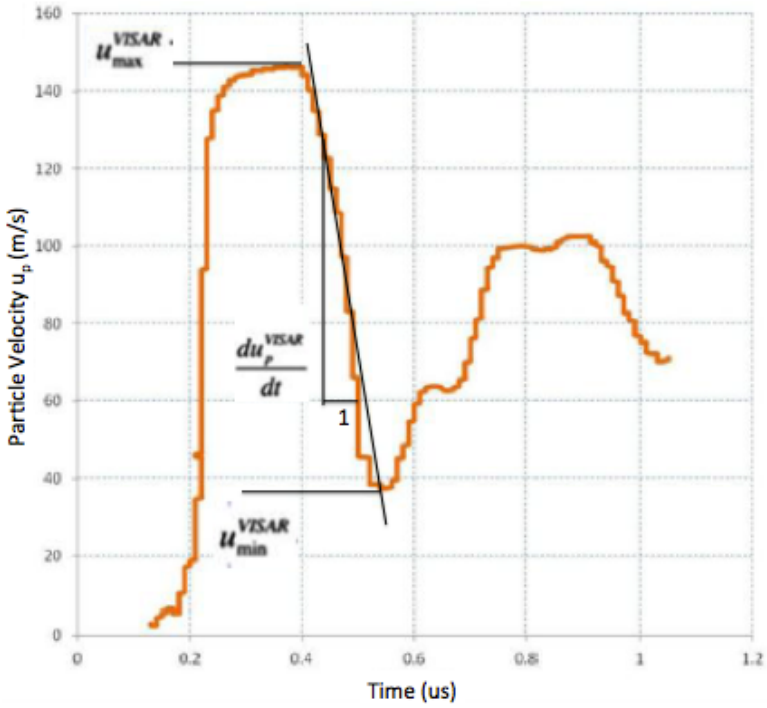

Figure 1.4. A typical VISAR data for the evolution of the free surface particle velocity [5].

For uniaxial strain, the amplitude for stress at HEL is given by [2]

$$\sigma_{HEL} = \rho_0 C_l U_p \tag{1.11}$$

where $\sigma_{HEL}$ is the amplitude of stress at HEL, $C_l$ is the longitudinal wave speed in the elastic regime given by equation (1.4), and $\rho_0$ is the density of the material. In the boundary of the elastic region, the yield stress $S_y$ can be directly related to the stress amplitude at the HEL for uniaxial strain, as given by [2]

$$S_y = \sigma_{HEL} \frac{1-2v}{1-v} \tag{1.12}$$

where $v$ is Poisson's ratio. But once the wave speed reaches plastic region, the velocity for the stress wave given by equation (1.4) is no longer valid and the wave speed

is given by the $U_s - U_p$ relationship provided by equation (1.9). The axial stress is given by [2]

$$\sigma_{axial} = \rho_0 U_S U_p = \rho_0 C_0 U_p + \rho_0 S U_p^2 \tag{1.13}$$

Yield stress can be obtained from the von Mises criterion, which for the state of stress during uniaxial strain in isotropic materials is given by $S_y = |\sigma_{xx} - \sigma_{yy}|$. If this increases as the axial stress increases then there the material experiences hardening. Material strength is typically strain and strain rate dependent as shown in figure 1.5. The stress-strain curve in many metals is described by a power law. If the material is strain rate dependent, the flow stress can have power law dependences with strain and strain rate as given by [2]

$$\sigma = \sigma_0 + k\varepsilon^n \dot{\varepsilon}^m \tag{1.14}$$

where $m$ and $n$ are the strain rate sensitivity and strain hardening exponent, respectively.

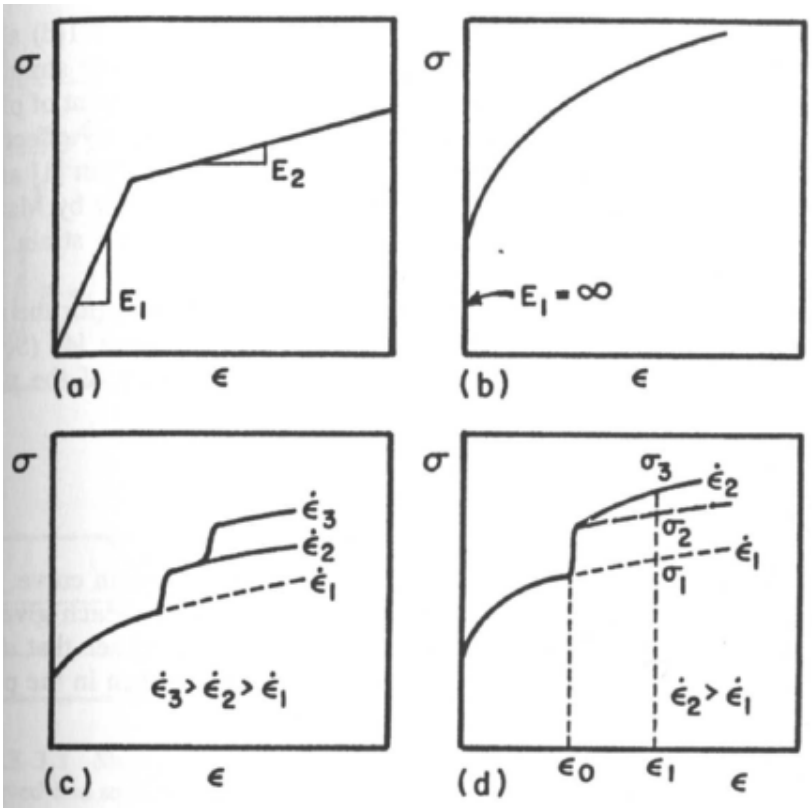


Figure 1.5. Stress-strain curves for ductile materials: (a) Bilinear elastoplastic, (b) Power law work hardening, (c) Strain-rate-dependent flow stress, (d) Strain rate history dependence of flow stress [2].

Applying the conservation equations (1.6-1.8) with equation (1.9), one can obtain plots of pressure versus specific volume and pressure versus particle velocity. This establishes a relation for pressure $(P)$ and density $(\rho)$ immediately behind the shock front, which is usually known Rankine-Hugoniot or "Hugoniot". The Rankine-Hugoniot is shown as a P-V curve in figure 1.6. In figure 1.6, the straight-line joining $(P_0, V_0)$ and $(P_1, V_1)$ is a Rayleigh line referring to the shock state $P_1$. When pressure is increased in a shock front, instead of following the $P - V/V_0$ path, it changes discontinuously for its initial value $P_0$ to $P_1$ [2]. A shock pulse of amplitude $P_1$ does not reach this point by following the Hugoniot line but is achieved via a thermodynamic path

given by Rankine-Hugoniot and the discontinuity of pressure and density in Hugoniot is related to the slope of the Rayleigh line [2].

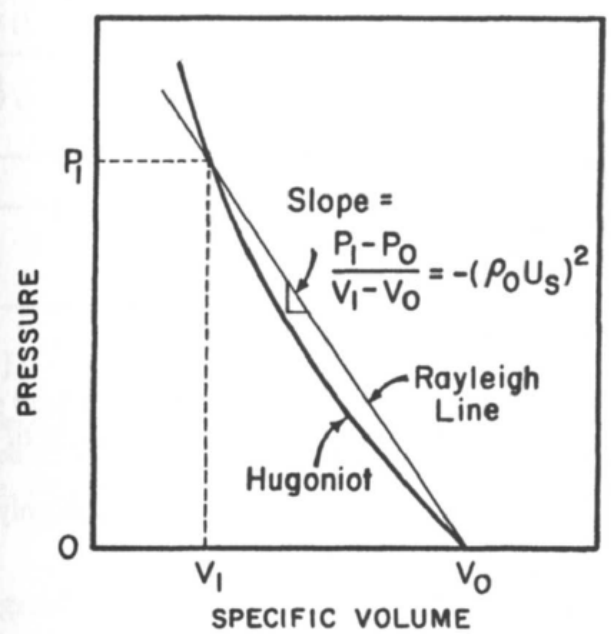


Figure 1.6. Characteristic Hugoniot (P-V) curve showing the Rayleigh line [2].

Many constitutive models have been developed for the shock loading, which is calibrated, and validated using the results produced from VISAR data. Some of the constitutive models that are widely used to predict dynamic strength in high strain rate applications are briefly discussed in the next section.

## 1.5. Material Strength Modeling for Shock Loading

Different loading conditions and varying temperature lead to changes in mechanical behavior of materials. To characterize this change in material mechanical behavior, several constitutive models exist; they consider the effects of strain rate, plastic strain, temperature and strength to capture the dynamic behavior of materials [33-42]. Strength models are subdivided into two main categories; the empirical based and the

physics (dislocation mechanics) based. Two of the most popular empirical based models are the Johnson-Cook (JC) [35] and the Steinberg-Cochran-Guinan (SCG) [37,38]. Both of them relate the flow stress of the material as a function of plastic strain and temperature in their constitutive equations. The major difference between JC and SCG is the strain rate dependence; JC is rate dependent whereas SCG is rate independent.

Johnson -Cook (JC) [35] considers the flow stress as a multiplicative function of strain rate, plastic strain and temperature (shown in equation (1.15) below) while the SCG considers the relationship between the shear modulus (G) and yield strength ($Y$) as a function of pressure and temperature (shown in equation (1.16 and 1.17) below), which also account for the variation in elastic constants at high strain rates [37,38].

The constitutive equation for the JC model is given as,

$$\sigma_f = (A + B\varepsilon^n)\left(1 + C\ln\left(\frac{\dot{\varepsilon}}{\dot{\varepsilon}_0}\right)\right)(1 - T^{*m}) \tag{1.15}$$

where, A, B and C are model constants; ε is the plastic strain and, T is the temperature.

The constitutive equation for the SCG model is given as [37,38],

$$G = G_0\left[1 + \left(\frac{G_p'}{G_0}\right)\frac{P}{\eta^{1/3}} + \left(\frac{G_T'}{G_0}\right)(T - 300)\right] \tag{1.16}$$

$$Y = Y_0\,(1 + \beta(\varepsilon + \varepsilon_i)^n\left[1 + \left(\frac{Y_p'}{Y_0}\right)\frac{P}{\eta^{1/3}} + \left(\frac{G_T'}{G_0}\right)(T - 300)\right] \tag{1.17}$$

where, β and η are model constants; Y is the yield strength; ε is the plastic strain; T is the temperature and, P is the pressure, subscript $'o'$ refers to the reference state ($T = 300K$, $P = 0, \varepsilon = 0$). Parameters with subscripts $P$ and $T$ refer to the derivatives of those parameters with respect to pressure or temperature at the reference state.

Several physics based models for material behavior exist. Some of the well accepted models are Zerilli-Armstrong (ZA) [39], Mechanical Threshold Stress [34]

(MTS), and the Preston-Tonks-Wallace (PTW) [41,42]. Zerilli-Armstrong [39] is dislocation-based, where the flow stress is assumed to have thermal and athermal components. The athermal component includes influence of solute and original dislocation density on yield stress with the microstructural effects depending on grain size [39].

The constitutive equation for the ZA for typical FCC metals is given by:

$$\sigma_f = \Delta\sigma_G' + kl^{-1/2} + C_2\varepsilon^{1/2}\exp(-C_3T + C_4T\ln\dot{\varepsilon}) \quad (1.18)$$

where, $C_1, C_2$ $C_3$ and $C_4$ are model constants; $k$ is the microstructural stress intensity known as the Hall-Petch constant; $l$ is the grain diameter; $\varepsilon$ is the plastic strain and, $T$ is the temperature.

The Mechanical Threshold Stress (MTS) [34] constitutive model includes the effect of dislocation dynamics with the microstructural evolution that has a complex dependent on strain rate and temperature. It accounts for clear thermal and athermal components. The flow stress for the MTS [34] is given by:

$$\sigma_f = \sigma_a + \sigma_T \quad (1.19)$$

$$\sigma_f = \sigma_a + (\hat{\sigma} - \sigma_a)\left\{1 - \left[\frac{KT\ln(\frac{\dot{\varepsilon}_0}{\dot{\varepsilon}})}{g_0\mu b^3}\right]^{\frac{1}{p}}\right\}^{\frac{1}{q}} \quad (1.20)$$

where, $\sigma_a$ is the athermal component characterizing the rate independent interactions of dislocations with long range barriers such as grain boundaries and $\sigma_T$ is the rate dependent interaction with short range obstacles. The parameter $\hat{\sigma}$ is the mechanical threshold stress that has a complex dependency on structure evolution and is a function of strain rate and temperature [34].

The Preston-Tonks-Wallace (PTW) is also a physics based model, where the flow stress is obtained by merging the flow properties of materials in the strong shock wave limit with the predominance of the non-linear dislocation drag over the thermal activation regime. The application this model ranges from the strain rate of $10^{-3} - 10^{12}\ s^{-1}$ [41,42].

Since PTW is suitable for explosive loadings and high velocity impacts, it has been calibrated and validated by many researches [42,43]. Parameters for the PTW model obtained from [41] are used as initial parameters in this research and as such will be reviewed in more detail than other models.

### 1.5.1 Overview of the PTW Model

This section briefly summarizes the PTW model, which consists of three different regions, (1) thermal activation, (2) overdriven shock, and (3) transition from thermal activation to overdriven shock regime. The strain rate dependence is of Arrhenius form, which is combined with a power law dependence to give work hardening saturation stress and yield stress [41]. Work hardening is captured by modifying the linear Voce law [44] to exponential form finally giving the expression for the thermal activation regime given by equation (1.22).

The overdriven shock regime is then formulated in the PTW model by the use of Wallace's theory of overdriven shock in metals [45,46]. The definition of overdriven shock is when the plastic wave is higher than the elastic precursor to produce a front steeper than that is attainable by adiabatic elastic compression, where the pressure at the peak of the plastic wave is large enough that its velocity is actually larger that that of the

elastic precursor, so only one wave exists. Wallace's theory [45,46] estimates the scaled average deviatoric stress from the average plastic strain rate.

The PTW model uses the saturation and the yield stress in the overdriven shock regime with the dependence of strain rate and the strain rate dimensionless variable and without the dependence of strain. Saturation and yield stress in the overdriven shock regime [41] is then combined with the saturation and yield stress provided by the thermal activation. In order to maintain the continuity of stress in the transition phase from thermal activation to the overdriven shock regime (phonon drag), the PTW model maximizes the saturation and yield stress in both regimes [41]. The abrupt increase of the strain rate sensitivity from thermal activation (low strain rate) to the overdriven shock regime (high strain rate) is allowed by minimizing yield stress [41]. The use of the inverse error function in saturation and yield stresses is to eliminate the exponentially suppressed reverse flow at finite stress in thermal activation regime. The mathematical representation of the PTW model is given by equations (1.21-1.27) [41,42].

Flow stress is given by:

$$\tau = 2\hat{\tau}G \tag{1.21}$$

where $G$ is the shear modulus $\hat{\tau}$ is the normalized flow stress given by:

$$\hat{\tau} = \hat{\tau}_s + \frac{1}{p}\left(s_0 - \hat{\tau}_y\right)\ln\left[1 - \left(1 - \exp\left(-p\,\frac{\hat{\tau}_s - \hat{\tau}_y}{s_0 - \hat{\tau}_y}\right)\right)\exp - \left\{\frac{p\theta\varepsilon}{\left(s_0 - \hat{\tau}_y\right)\left[\exp\left[p\left(\frac{\hat{\tau}_{\square} - \hat{\tau}_y}{s_0 - \hat{\tau}_y}\right)\right] - 1\right]}\right\}\right]$$

(1.22) Where $\hat{\tau}_s$ and $\hat{\tau}_y$ are normalized saturation stress and yield stress, respectively, which account for all three regimes: thermal, overdriven shock and transition regime. Maximizing the saturation stress for both thermal activation and overdriven shock regimes maintains stress continuity and also provides a smooth transition between them.

$$\hat{\tau}_s = \max\left\{s_0 - (s_0 - s_\infty)\,\mathrm{erf}\left[k\hat{T}\ln\left(\frac{\gamma\xi}{\dot{\varepsilon}}\right)\right],\ s_0\left(\frac{\dot{\varepsilon}}{\gamma\xi}\right)^{\beta}\right\} \tag{1.23}$$

Yield stress uses a similar approach as the saturation stress, including the effect of strain rate sensitivity at around $10^3 s^{-1}$ and below $10^{12}\ s^{-1}$.

$$\hat{\tau}_y = \max\left\{y_0 - (y_0 - y_\infty)\,\mathrm{erf}\left[k\hat{T}\ln\left(\frac{\gamma\xi}{\dot{\varepsilon}}\right)\right],\ \min\left[y_1\left(\frac{\dot{\varepsilon}}{\gamma\xi}\right)^{y_2}, s_0\left(\frac{\dot{\varepsilon}}{\gamma\xi}\right)^{\beta}\right]\right\} \tag{1.24}$$

$\xi$ is the strain rate variable which is defined as:

$$\xi = \frac{1}{2}\left(\frac{4\pi\rho}{3M}\right)^{1/3}\left(\frac{G_0}{\rho}\right)^{1/2} \tag{1.25}$$

where M is the atomic mass (kg per atom), $\rho$ is the density ($kgm^{-3}$).

The pressure and temperature dependent shear modulus is defined as:

$$G = G_0(p)\left(1 - \alpha_p\hat{T}\right) \tag{1.26}$$

$\hat{T}$ is the dimensionless temperature variable, which is defined as the ratio of current temperature T to the melting temperature $T_m$, $G_0(p)$ is the shear modulus at zero pressure.

$$\hat{T} = \frac{T}{T_m} \tag{1.27}$$

$s_0, s_\infty, y_0, y_\infty, y_1, y_2, p, \theta, k, \gamma, \xi, \beta, \alpha_p, G_0, \rho, T_m, M$ are the material parameters, where $s_0, s_\infty, y_0, y_\infty, y_1, y_2, p, \theta, k, \gamma$ are the PTW model parameters derived from experimental data.

The strength models described above are used to capture the dynamic behavior of material strength and plasticity. Many researchers [9-18] are using experimental techniques that exploit hydrodynamic instabilities to infer material strength and study dynamic plasticity in materials. This research focuses on studying plasticity through the hydrodynamic instability approach by creating perturbations on the geometry that can

provide more insights into how plasticity evolves at high pressures and strain rates and how the material strength interacts with the instability. The next section briefly describes the hydrodynamic instability techniques like Rayliegh-Taylor (RM) and Richtmyer-Meshkov (RM).

## 1.6. Hydrodynamic Instability for Material Strength Determination

The Rayleigh-Taylor (RT) and the Richtmyer-Meshkov (RM) instabilities are related to Inertial Confinement Fusion (ICF), which is one the programs supporting this research. Many researchers have used these techniques to study dynamic material strength due to their high dependency on this parameter and the existence of experimental capabilities for capturing dynamic and highly transient data during the evolution of these instabilities. Both RT and RM instabilities have been shown to be more effective tools to infer material strength in solids than the out-of-plane velocity measurements that are usually obtained in a typical shock experiments [9-18]. The fundamentals of both experimental techniques rely on a perturbed material interface and both are based primarily on linear hydrodynamic analysis of material behavior at the interface [6], where the two materials must have a difference in density for the instability to occur. The next section will briefly discuss these two instabilities.

### 1.6.1. Rayleigh-Taylor (RT)

In the Rayleigh-Taylor instability, a less dense material gradually pushes or supports a more dense material [8,48], with a variable velocity, typically produced by a constant acceleration, leading to loading that is approximately quasi-isentropic in nature

and, under the appropriate geometric constraints, results in high pressures [49, p.107], similar to shock loading pressures, but at lower temperature. As a result, high strain rates (~ $10^7$ $s^{-1}$) can be achieved experimentally [7, 11, 50, 51] and the evolution of the perturbation is measured dynamically using X-ray or proton radiography [8,11,51,52]. Dynamic and transient data acquired from experimental methods can be used for validation of material models [7].

According to hydrodynamic perturbation theory, the classical RTI growth rate in the linear regime is given by [6]

$$\sigma_{RT} = \sqrt{\frac{2\pi\, a\, A_t}{\lambda}} \tag{1.28}$$

with the perturbation amplitude of the unstable interface growing exponentially in time

$$\zeta = \zeta_0 \exp(\sigma_{RT} t) \tag{1.29}$$

where, $a$ is the acceleration in $m/s^2$, $\zeta$ is the current value of the amplitude of the perturbation of the unstable interface, $\zeta_0$ is the initial amplitude of the perturbation, $\lambda$ is the wavelength of the perturbation, $A_t$ is the Atwood number and is given by equation (1.30) and $k$ is the wave number of the perturbation and is given by equation (1.31)

$$A_t = \frac{\rho_2 - \rho_1}{\rho_2 + \rho_1} \tag{1.30}$$

$$k = \frac{2\pi}{\lambda} \tag{1.31}$$

From equations (1.24) and (1.27), the RT growth rate can be written as

$$\sigma_{RT} = \sqrt{A_t a\, k}$$

In solids with strength, the behavior is different. Piriz [9] studied the RT instability in elastic solids and provided an analytical description of the RT instability for a perturbed solid-gas interface where the solid is accelerated by the gas:

$$\ddot{\xi} = A_T k g \xi - \frac{2G}{\rho} k^2 (\xi - \xi_0) \;\; where \;\; g = {P_0}/{\rho h} \tag{1.32}$$

where $\xi$ is the perturbation amplitude, $\xi_0$ is the initial amplitude, ($A_T \approx 1$ for a solid-gas interface), $P_0$ is a constantly applied pressure of a gas accelerating a plate of density and thickness $\rho$ and $h$, respectively, and $G$ is the shear modulus of the solid. Equation (1.32) is derived from the conservation of momentum at the perturbed surface with the consideration of solid elasticity alone [9]. Analysis of equation (1.32) shows that the perturbation of the interface depends on the wave number, $k$. The perturbation interface is marginally stable if $k$ is greater than the cutoff wave number $k_c = \rho g / 2G$.

In addition, Piriz [9] also discussed that if a solid-gas interface is considered, the steady state solution is damped out but the solid-gas solution is retained. However, if there is strain rate dependency present in equation (1.32), it would provide a different transient response but the same steady-state amplitude. Similarly, Piriz [10] also studied the RT instability in elastic-plastic solids where he noted that the plastic response is necessary but not sufficient for instability, that is a material could yield in the transient response but be marginally stable at steady state, which is purely elastic.

Park et al. [11] studied the effect of material strength on the stabilization of the RT instability for polycrystalline vanadium samples that were compressed and accelerated quasi-isentropically at ~ 1 Mbar pressure while maintaining the samples in the solid state. They [11] conducted several experiments to measure the RT growth by using face-on radiography. From the experiments and simulations performed for vanadium, the samples were predicted to have higher strength with the higher peak pressure and hence showing the higher degree of strength stabilization of RT instability

[11]. Figure 1.7 depicts the effect of strength in stabilization of RT instability performed by Park et al. using a 2D radiation-hydrodynamics simulation [11]. He shows density plots of RT growth at different times using simulations with and without material strength [11]. It can be clearly seen from figure 1.7 that using PTW material strength model slows down the RT instability significantly as compared to the no strength model. If the strength of the material is not considered, it gives very large perturbations as can be seen in figure 1.7: density plot at 75 ns time scale compared to the density plot obtained using a PTW model at the same time for a vanadium sample [11].

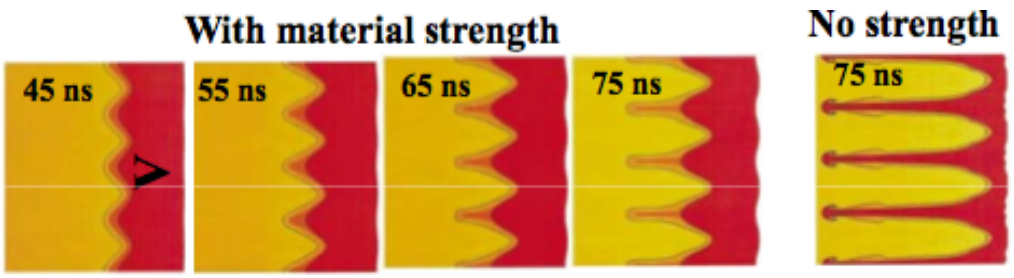


Figure 1.7. Density plots of RT growth from a 2D radiation-hydrodynamics simulation at 45, 55, 65, and 75 ns, using the PTW strength model and with no strength model at the far right [11].

Loomis et al. [28] studied the seeding of instabilities in beryllium-based ICF targets that are susceptible to different hydrodynamic instabilities at different stages of implosion. Due to the perturbations present at the ablation surface, he noted that perturbed surface grow from the Richtmyer-Meshkov (RM) instability at an early time seeding the RT instability once the target begins to accelerate [28]. In addition, Aglitskiy et al. [16] studied the perturbation evolution of a rippled sample triggered by laser-driven shock wave breakout at the free rippled rear surface by gradually increasing the shock pressure. He explained that the evolution of a rippled shock wave after the shock breakout follows RM instability growth at low and medium pressures. As the shock

pressure is increased, the RT instability is triggered when the leading edge of the rippled expansion wave breaks out at the ablation front opposite from the location of the valleys causing the target to accelerate [16].

Although it can be seen that the RT instability is a dominant instability in inertial confinement fusion, the RM instability can seed the RT instability [16, 28]. Therefore, it becomes important to understand the evolution of the RM instability and the effects of material strength on it. Also, from the experimental point of view, the RM instability has a slower linear growth rate compared to RT, which allows the use of sensitive measurement techniques like Transient Imaging Displacement Interferometry (TIDI) to catch the instability in its linear regime making it easier to model and compare to asymptotic solutions as the one proposed by Piriz [13-14]. The next section will briefly discuss the RM instability.

### 1.6.2. Richtmyer-Meshkov (RM)

The Rithcmyer-Meshlov instability is similar to the RT instability, which also requires a perturbed material interface with different densities. However, the RT instability occurs only when a less dense material pushes or supports a more dense material whereas the RM instability occurs for any value of the Atwood number, i.e., for a shock propagating from a light material to a dense material and vice versa [12]. Also, the perturbation growth in the RM instability is a result of a shock wave that passes through the material interface resulting in a impulse like response, which is easier to obtain and characterize at high pressures and, hence, can be used for the validation of material models [53]. Although RM and RT require similar diagnostic tools [15-17], RM

has an advantage over RT that allows some sensitive experimental measurement techniques like TIDI to capture the instability in the linear regime due to its slower linear growth rate [13,18,28,54-56]. Also, RM can be used for low to moderate pressures (~<100 GPa) [13].

The classical RM instability growth rate is given by Richtmyer 1960 [6],

$$\sigma_{RM} = A_t \, k \, \Delta u \tag{1.33}$$

where $\Delta u$ is velocity increment caused by the transit of the shock at time $t = 0$, and both $k$ and $A_t$ are defined above (equations (1.30-1.31)).

According to hydrodynamic linear theory, a perturbation on an unstable interface under the RM instability grows linearly in time as follows [6],

$$\zeta = \zeta_0 \, (1 + \sigma_{RM} \, t) \tag{1.34}$$

where, $\zeta$ and $\zeta_0$ are the amplitudes of unstable surface interface and initial surface respectively and $t$ is the time.

Piriz et. al. [14] investigated RM instability behavior analytically in solids under high-energy density conditions, where they showed that strength determines the maximum perturbation amplitude. They provided a simple scaling law for the relationship between strength and perturbation amplitude. This analysis done by Piriz et. al. [14] does not account for the early transient response of the shock at time $t = t_0$ when the shock is still in the solid-vacuum boundary and is based on the assumption that at time $t$ that is greater than $t_0$, the shock has traversed several perturbation wavelengths into the material. Also, a constant pressure is maintained at the solid-vacuum boundary driving a shock, which moves with constant velocity into the material [14]. At time $t > t_0$, the perturbation amplitude $\xi(t)$ grows to $\xi_0$, which is greater than the initial

perturbation amplitude $\xi_i$ as described by the elastic evolution. Later, when the perturbation amplitude is greater than the plastic perturbation amplitude $\xi_p$, i.e, $\xi > \xi_p$, it grows to a maximum value $\xi_m$ at time $t_m > t_0$ and after some time, the perturbation will remain oscillating in a purely elastic regime determined by the shear modulus [14]. Piriz et al. [14] provided a relationship among effective yield strength of a material $S_y$, post shock density of a material $\rho$, wave number $k$, a numerical factor that expresses the ignorance about the exact velocity field $\alpha$, and amplitude of perturbation $\xi$ and is given by

$$\rho \frac{\alpha}{k} \ddot{\xi} = -S_y \tag{1.35}$$

Piriz et al. [13] used the RM instability as a tool to infer and evaluate material yield strength of solids by a single steady shock wave below melting shock pressure, which can be obtained from the scaling law given by

$$\bar{\xi} - \xi_i \approx \frac{\alpha \rho \dot{\xi}_0^2}{kY} \tag{1.36}$$

where, $\bar{\xi} \approx \xi_m$, $\xi_0 \sim \xi_i$ and $Y$ is the yield strength that can be experimentally evaluated from a single measurement of amplitude taken at a relatively long time ($t \geq t_m$).

Experiments using the RM instability do not guarantee stability: large shocks, large initial perturbations, and low yield stress can all lead to the formation of material spikes that detach from the parent material [15,17,53]. Figure 1.8 shows spikes and bubble formation from a sinusoidally perturbed sample after a shock wave has passed through the perturbations, leading to release, where the perturbations invert and the spikes are formed. These spikes grow beyond the free surface of the material and the

bubble grows into the free surface feeding all the mass into the spikes and sometimes these spikes detach from the parent material resulting in unstable RM [17].

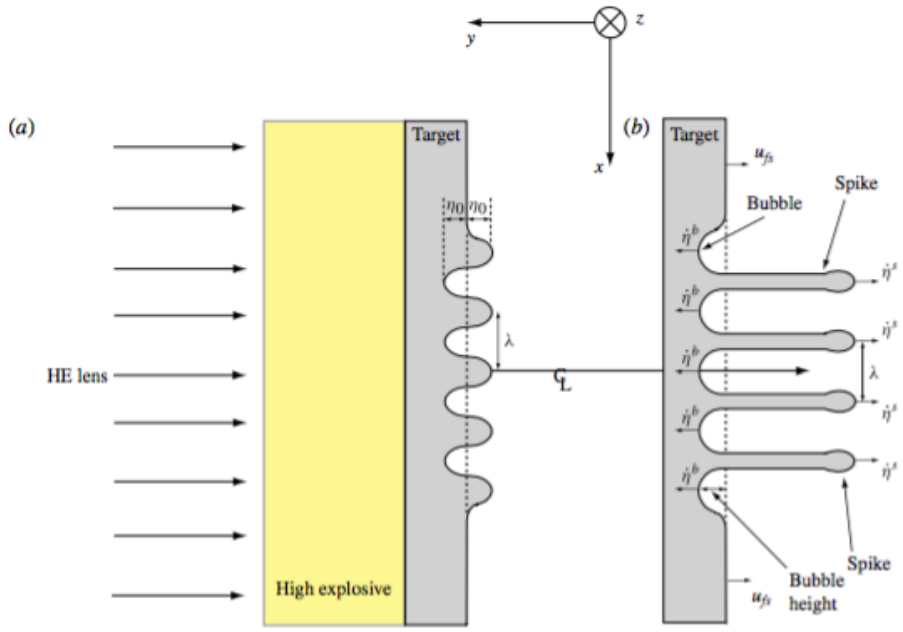


Figure 1.8. Pre-shocked (a) and post-shocked (b) geometries for unstable RM experiments [17].

During the shockwave loading, leading to release, the perturbations invert and the spikes form and grow beyond the free surface, and bubbles grow into the free surface and feed mass into the spikes [17]. Dimonte et al [15] studied the evolution of these spikes and bubbles and observed an ejecta transition where saturated bubbles and spikes determined the amount and velocity of ejecta, respectively. They [15] used RM instability at a copper-gas interface to infer material's yield stress from the velocity and scaled saturated amplitude of spikes given by

$$Y_{RMI} \sim \frac{\rho |V_{sp}^{0}|^{2}}{K h_{sp}^{max}} \tag{1.37}$$

where $Y_{RMI}$ is RMI inferred yield stress, $\rho$ is the density, $V_{sp}^{0}$ is the velocity of spike, $kh_{sp}^{max}$ is the scaled saturated amplitude of spike. The RMI inferred yield stress was then compared with the yield stress with direct yield measurements under the same condition where they found that yield strength can be inferred from the spikes and bubbles velocity and saturated amplitudes [15].

Peralta et. al. [18] used the RMI with a square surface perturbation on a copper sample to study anisotropic plasticity effects by correlating measured changes in perturbation amplitude at free surfaces to local plastic behavior and grain orientation. In order to produce larger changes in perturbation amplitudes at low shock pressures, they [18] pressed a plexiglass window against the peaks of perturbations leaving the valleys as free surfaces. They reported that the final perturbation amplitude was largest in the grains oriented close to $< 001 >$ parallel to shock and lowest for grain with shock directions close to $< 101 >$ [18]. They also used the yield strength to obtain the maximum value of resolved shear stress (RSS) for two grain orientations with maximum and minimum final amplitude, where they observed that RSS value for the grain orientation of maximum final amplitude was lower than the RSS value for the grain orientation of minimum final amplitude [18].

Experiments using the RM instability as those described above are used in this research as the experimental technique to get the transient and dynamic data, which is in turn used to validate the material model. This research also focuses on the effect of the material strength on RM instability and its growth.

In ductile fracture, the spallation process is controlled by localized plastic deformation. Spall damage is a plasticity-controlled phenomenon, and the dynamic plasticity of a material is affected by anisotropy and local plastic response. Many studies have been conducted to show that damage is driven by strain localization [5,57]. Strain localization seen at and around the boundaries correlates quite well with nucleated damage sites, which implies that shock wave propagation in metals lead to strain localization next the boundaries due to property mismatch at these locations sue to plastic and elastic [5,57]. The next section briefly describes the mechanism of spall damage during shock loading condition.

## 1.7. Spall Damage

Spall damage is a complex phenomenon resulting from the shock loading of a material. When very large tensile stresses are imposed in a very short time, spallation can occur as a result of nucleation, growth and coalescence of voids. Most of the spallation data has been is obtained from flyer-plate impact studies [59] or from experiments using direct application of explosives [60].

Spall damage in ductile materials, especially metals, is defined as a planar separation of material parallel to the wave front due to a dynamic tensile stress component perpendicular to this plane [2]. Tension is induced in the sample by crossing of two release waves: one coming from the front surface when the pressure loading on it falls off and the other due to the reflection of the incident shock wave from the rear (free) surface [2]. If the magnitude and duration of the tensile stress are sufficient, internal

ruptures occur and spallation can be observed [2]. The formation of the spall plane due to interaction of the shock waves is shown in the figure 1.9.

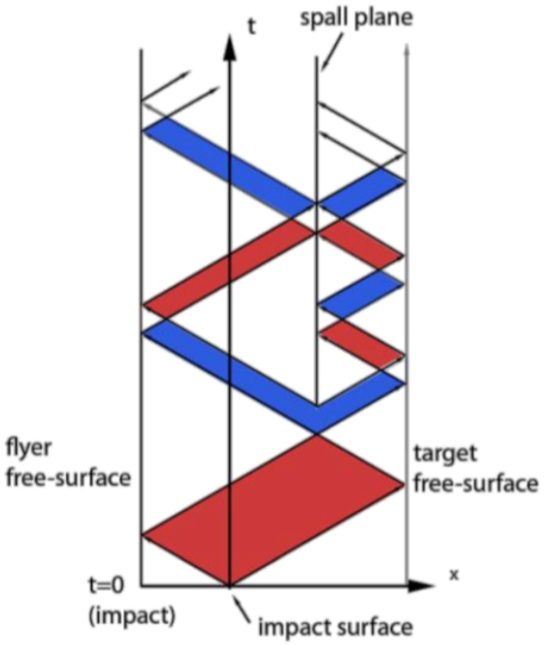


Figure 1.9. Distance-time (x-t) plot showing the spall plane due to the waves generated from free and impact surfaces (red), and waves reflected from the spall plane (blue) [5]

As mentioned earlier, spallation process is controlled by localized plastic strain. Recently, Krishnan et al. [5,57] used a modified crystal plasticity framework with an added Gurson-Tvergard-Needleman (GTN) damage model to perform 3-D finite element simulations of spall damage in bicrystals and multicrystals of copper showing strain localization at and around grain boundaries that show damage. Void nucleation damage from the simulation strongly correlates to the damage sites observed experimentally for shock loaded multicrystalline copper. Figure 1.10 shows simulation results from Krishnan [5] for the equivalent plastic strain and the void volume fraction in selected sites with high damage localization found experimentally in multicrystalline copper.

These simulation results were then compared to the corresponding experimental data. Figure 1.10 shows that strain localization appears next to and around grain boundaries; this drives damage nucleation, which promotes plastically driven damage [5].

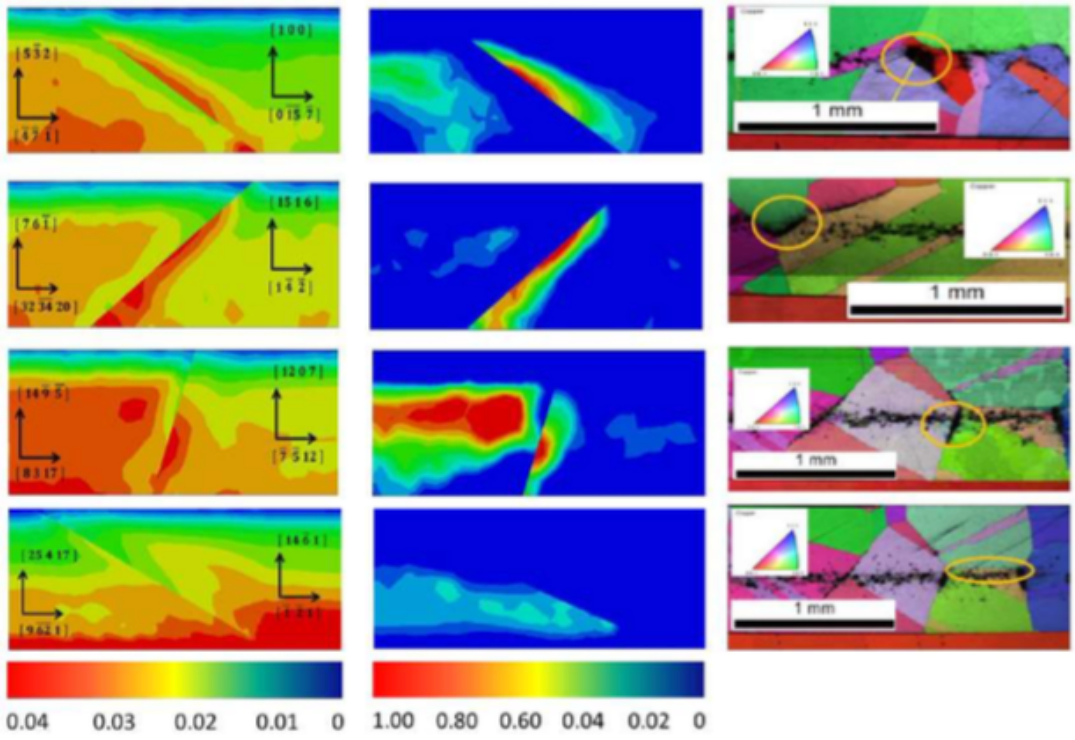


Figure 1.10. Contour plots for equivalent plastic strain (left), void volume fraction (center), and corresponding EBSD scan images of the damage sites (right) in multicrystalline copper [5].

Spall damage can be classified in 3 regimes: incipient spall, intermediate spall and full spall leading to fracture. Incipient spall relates to the nucleation of the voids, intermediate spall combines mechanisms of growth of nucleated voids and initial coalescence of these growing voids and full spall fracture represents the final coalescence producing the rupture in a material. Figures 1.11 (a), (b) and (c) provide typical examples of these 3 regimes of spall damage.

Evolution of damage is affected by heterogeneity of the material, as induced by composition or anisotropy. Many researchers have investigated effects of microstructure on spall damage. The next section briefly describes some of these effects.

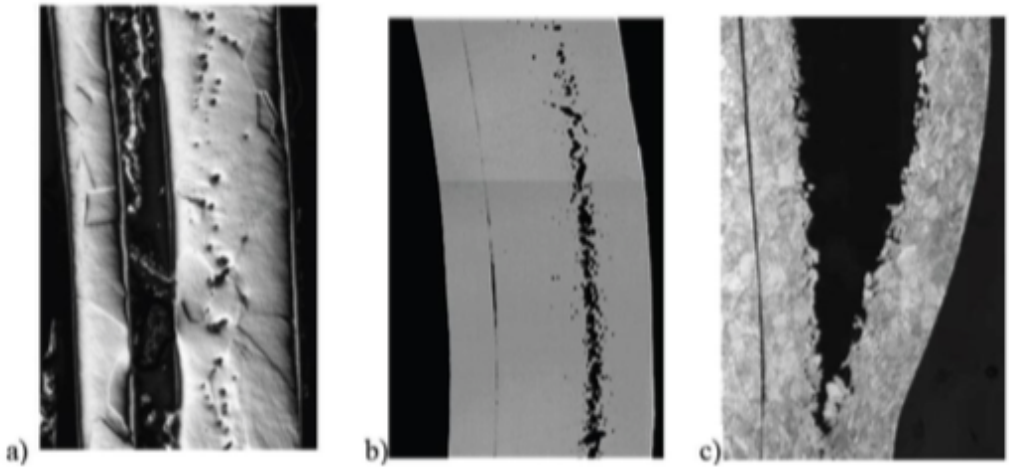


Figure 1.11. Spall damage examples showing the 3 regimes of spallation. a) Incipient spall b) Intermediate spall and c) Full spall fracture [3,20,23]

## 1.8. Microstructural Effects on Spall Damage

Grain boundaries, triple joints are intrinsic defects and precipitates, inclusions, and preexisting porosity are some examples of extrinsic defects, whereas grain size, grain orientation, and misorientation between adjacent grains are some of the parameters that are present in the microstructure. These defects and their associated parameters have a significant effect on spall damage. In order to fully understand where and how the damage nucleates and grows within the material, it becomes very important to understand microstructural effects on spall behavior. There have been many studies and research conducted to understand and find the effect of these defects and associated parameters on spallation process [2,23,61-68]. Experiments conducted by Chen et.al. [65] for Aluminum alloy 6061 and Minich et. al. [67] for 99.99% of copper showed that single

crystals have higher spall strength than polycrystalline materials. They also showed the significant difference in spall strength with different crystallographic orientations of grains, e.g., Minich et. al. [67] reported that $< 100 >$ single crystals exhibited increasing spall resistance with increasing pressure and showed higher spall strength than other crystal orientations. They also showed that crystal orientations $< 110 >$ and $< 111 >$ exhibit relatively similar behavior to one another [67].

After conducting an experiment for aluminum alloy 7010-T6 and studying the response of a shock wave as a function of orientation to the loading axis to the rolling direction, Vignjevic et. al. [68] reported that the longitudinal direction gives higher spall strength and Hugoniot Elastic limit than the transverse direction. Peralta et. al. [4] conducted experiments in shock loaded copper multicrystals to understand the correlation between microstructure and incipient spall damage and showed that the damage sites localize at and around the grain boundaries, especially triple points. Henrie et. al. [69] provided a statistical representation of voids to quantify the spallation for impacted tantalum samples. Hashemian [3] studied the distribution of misorientation angle along the grain boundaries and reported that most frequent damage localization in multicrytalline copper was due to the high angle misorientation from $40^{\circ} - 60^{\circ}$, as shown in figure 1.12 (a). She also showed that damage localized preferentially at triple points, quadruple points, and their associated grain boundaries. Figure 1.12 (b) shows the distribution of damage localization sites in copper multicrystals [3].

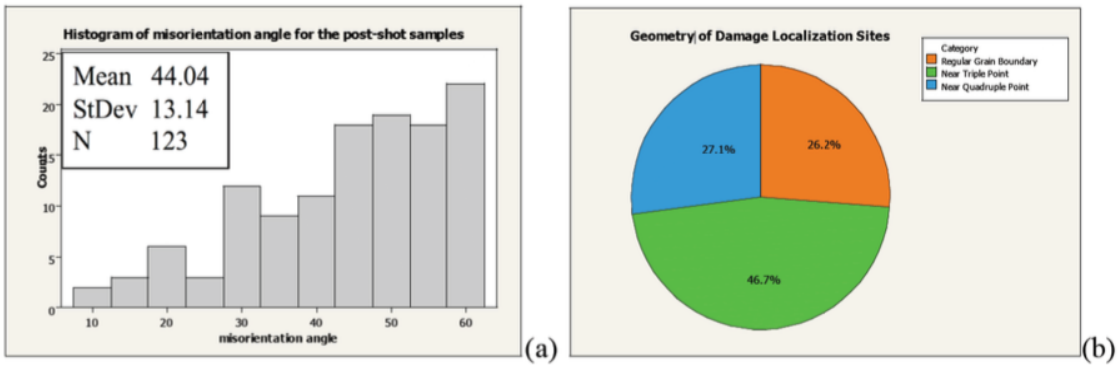


Figure1.12. (a) Histogram of misorientation angles for boundaries in copper multicrystals. (b) Fraction of damage sites according to grain connectivity [3].

Wayne et. al. [61] studied the intergranular damage in polycrystalline copper and reported that boundaries with misorientation angles from $35^{\circ} - 40^{\circ}$ had the highest probability to localize spall damage with some tendencies of damage to occur at tips of terminated twins with $60^{\circ}$ misorientation. Krishnan et. al. [57] studied the intergranular and transgranular damage sites to find the characteristics of weak grain boundaries and showed that large Taylor factor mismatch, either along the shock direction or the crystallographic grain boundary normal coupled with misorientation angle, is a primary driving force for void nucleation. They also reported that the favorable sites for void nucleation and damage are the triple junctions and grain boundaries [57]. The next section will briefly discuss the effect of misorientation angles on damage.

## 1.9. Effect of Misorientation Angles on Damage

It is important to gather statistics on the parameters that define microstructural locations with a clear tendency to localize the spall damage. Research has been carried out [3,4,20,22,66,84] to study the relationship between spall damage and local microstructure using polycrystalline copper samples. The work in [3,4,20,22] focused on

preferred sites for void nucleation, while the work in [66,84] focused on boundaries that were less preferred for damage nucleation. It was observed that boundaries with misorientation angles ranging from $25° - 50°$ and $55° - 60°$ show higher probability of being damage sites [3,4,20,22]. Figure 1.13 provides the frequency of misorientation angles in boundaries with damage sites while figure 1.14 shows misorientation angles for all grain boundaries present in the copper polycrystalline sample analyzed in [22,61].

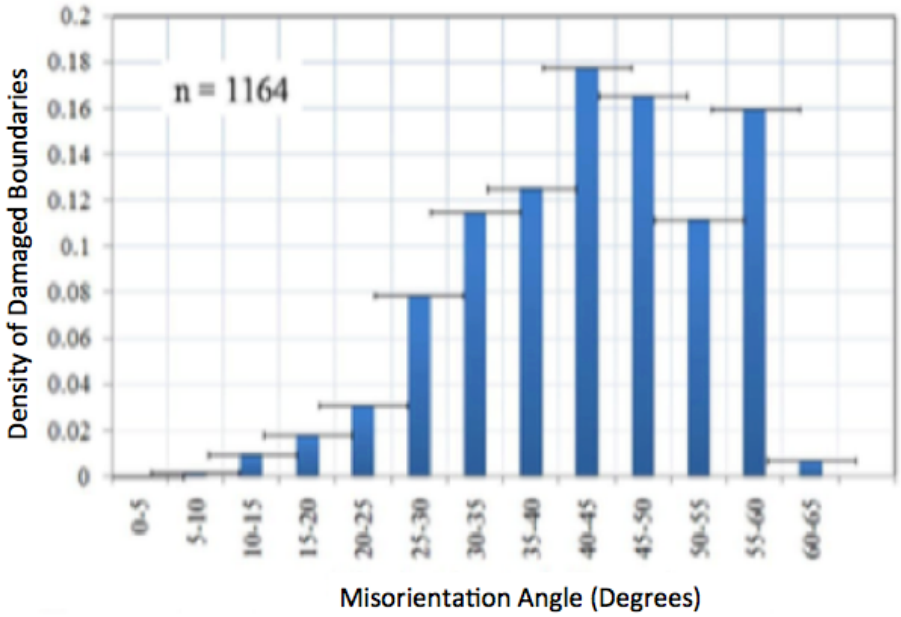


Figure 1.13. Statistical analysis of damaged boundaries in 3 polycrystalline copper samples measured using 2-D cross-sections, where n indicates the total number of measurements [22,61].

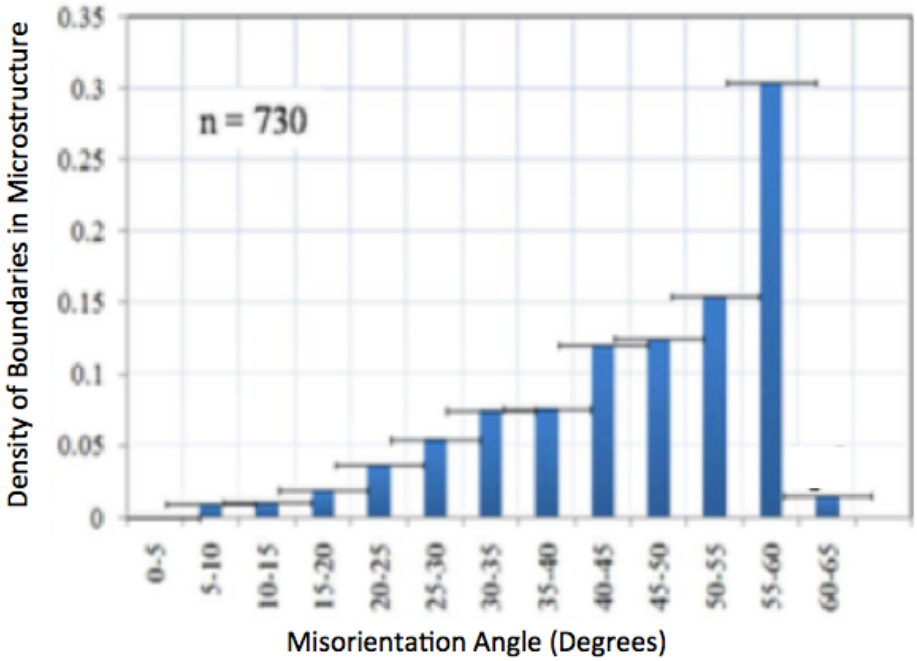


Figure 1.14. Statistical analysis of all boundaries in an untested polycrystalline copper sample with the same thermomechanical history as the ones used to obtain the results shown in figure 1.13, where n indicates total number of measurements [22,61].

The probability of a misorientation angle being present in the microstructure sampled during characterization is determined by using misorientation data collected from both damaged and undamaged grain boundaries. The total probability theorem [85] provides a mathematical description of the probability of finding a misorientation angle $\theta$,

$$P(\theta) = P(\theta|X = 0)\,P(X = 0) + P(\theta|X = 1)P(X = 1) \tag{1.38}$$

where $P(\,)$ is the probability, $(X = 1)$ is the presence and $(X = 0)$ is the absence of damage. Also, the probability of finding damage $(X = 1)$ at a boundary given its misorientation angle $\theta$ is defined by Bayes' theorem as [85]

$$P(X = 1|\theta) = \frac{P(\theta|X=1)\,P(X=1)}{P(\theta)} \tag{1.39}$$

Figure 1.15 represents the measured misorientation angles of grain boundaries with and without damage and the probability distribution predicted from the total probability theorem. Figure 1.15 shows that the probability of measured misorientation angles of grain boundaries in the sample is in good agreement with the probability distribution predicted from the total probability theorem. Figure 1.16 represents the probability of finding damage in a boundary given its misorientation angle $\theta$ as predicted from Bayes' theorem [5].

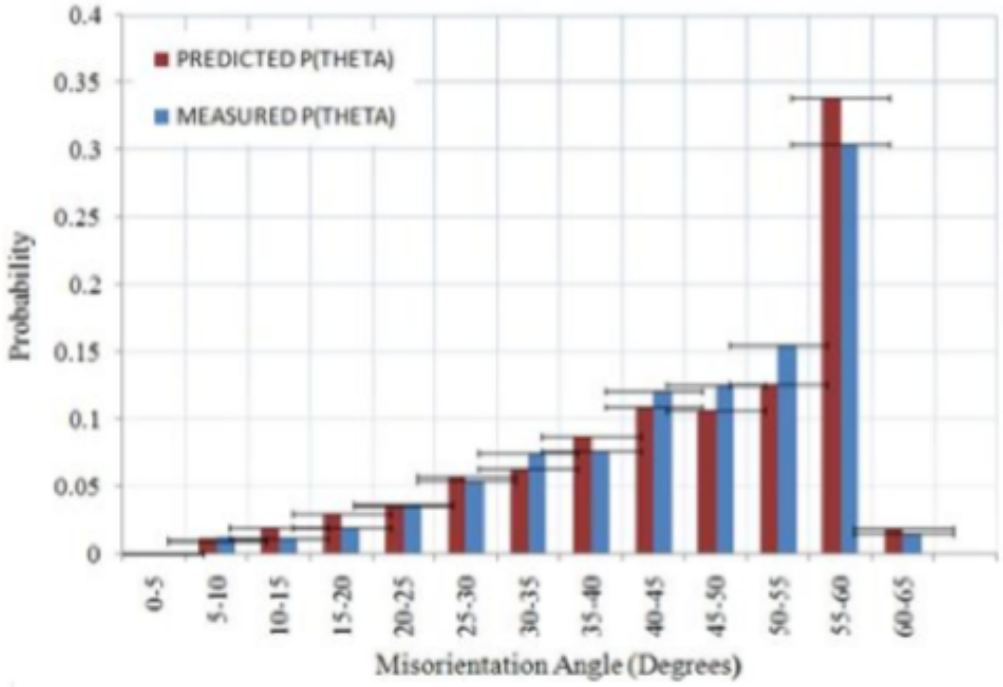


Figure 1.15. Predicted and measured probabilities for finding a given misorientation angle in the samples examined in [22,61].

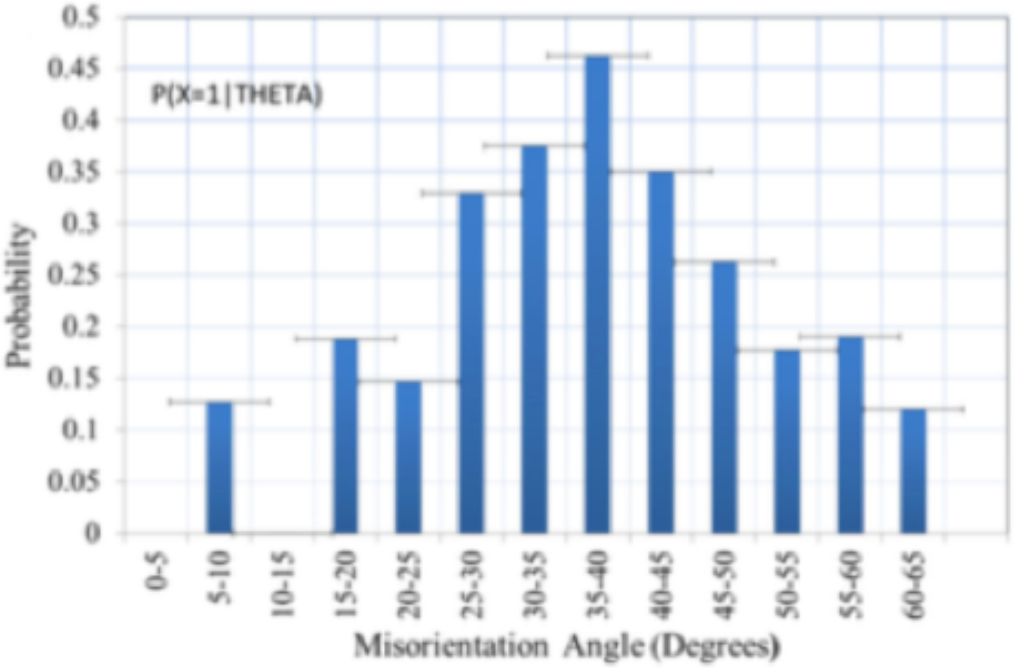

Figure 1.16. Probability of finding damage in a boundary given its misorientation angle $\boldsymbol{\theta}$ [22,61].

From figures 1.13 through 1.16, one can see that damage tends to be present more often for misorientation angles ranging from $25° - 50°$ and $55° - 60°$. The misorientation angle boundaries ranging from $25° - 50°$ are considered micro-structurally weaker than others. In polycrystalline copper, localization of damage in boundaries with misorientation angles around $55° - 60°$ is often observed and is caused due to twin boundaries. However, in the original microstructure, probability of localization of damage at misorientation angles $55° - 60°$ is lower than expected from 'random' sampling, which suggests that these boundaries are strong due to their low energy [86,87]. Escobedo et. al. [66] also observed that voids do not nucleate at special $\sum 1$ and $\sum 3$ boundaries, which is in agreement with trends reported by Wayne et. al. [22], except for the tip of annealing twins (terminated twins). These terminated twins are

incoherent $\sum 3$ boundaries, which can have higher energy and lower strength than coherent twins [88].

Krishnan [5] set up a finite element model to simulate the traditional flyer-plate impact experiment of a copper multicrystal to understand the effect of microstructure in spall damage. He reconstructed the 3-dimensional microstructure of a multicrystalline sample to create this model from 20 different serial sectioned images spaced 50 μm between slices using AVIZO$^{TM}$ software [5]. The complete microstructural reconstruction is shown in figure 1.17 [5], where the thickness of the multicrystalline copper target and flyer were 1.0 mm and 0.5 mm respectively. He then performed a finite element analysis on this 3-D reconstructed multicrystal using crystal plasticity with a modified GTN based damage model that he developed for the ABAQUS$^{TM}$/Explicit solver. From the simulation, he observed that large damage sites that can be correlated to the microstructural features [5]. To understand the influence of microstructural features on incipient spall damage, he compared the damage profile reconstructed from the 2D serial sectioned images shown in figures 1.18 and 1.19. He then observed that the simulation result was in good agreement with the large damage sites observed experimentally [5]. Analysis of the simulation results obtained by Krishnan [5] on a copper multicrystal with emphasis on misorientation effects is the focus of the research. The outcomes of this analysis are discussed in chapter 7.

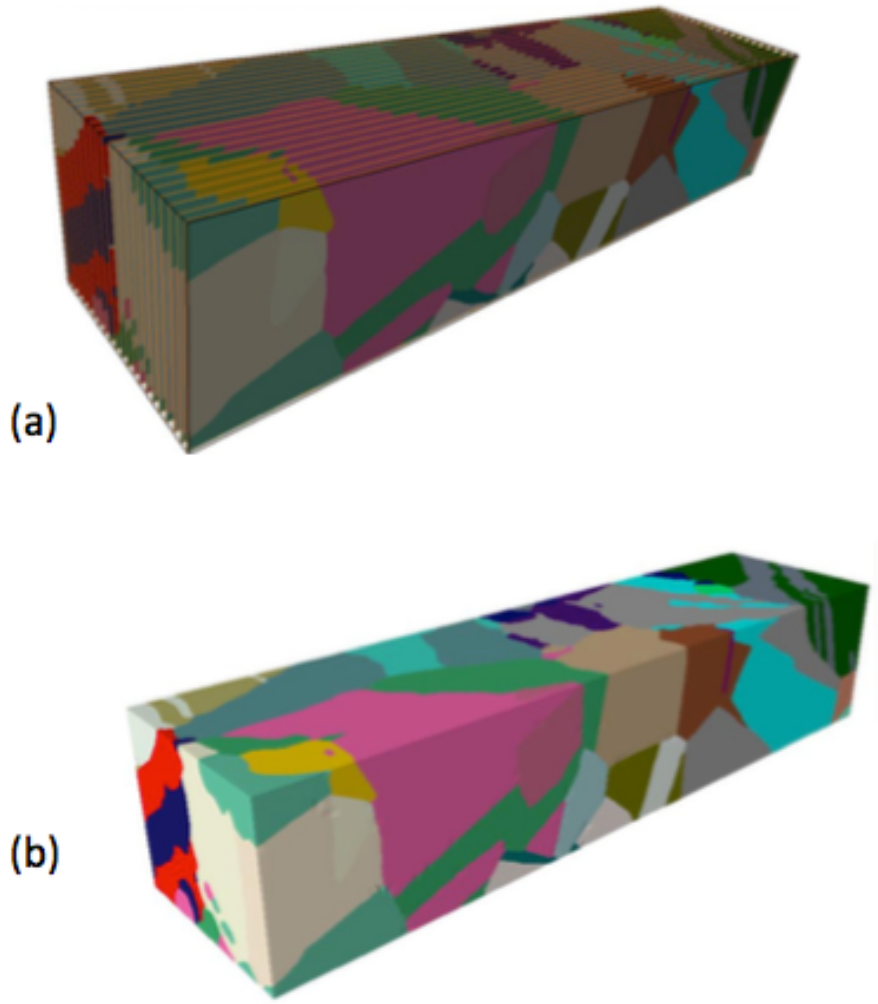


Figure 1.17. (a) Serial-sectioned images (20 slices) used for the 3-D reconstruction. (b) 3-D reconstructed multicrystal model [5].

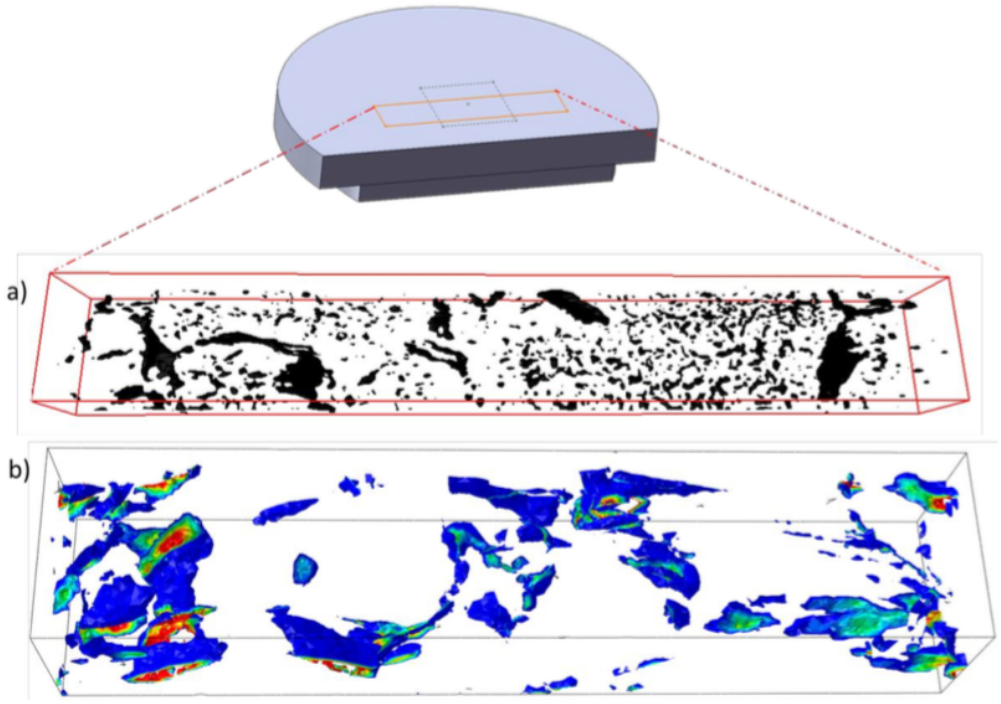


Figure 1.18. Spall damage in the multicrystal sample (a) cross-sectional image of the damage zone observed experimentally (b) iso-surface plot of total void fraction obtained from simulation [5].

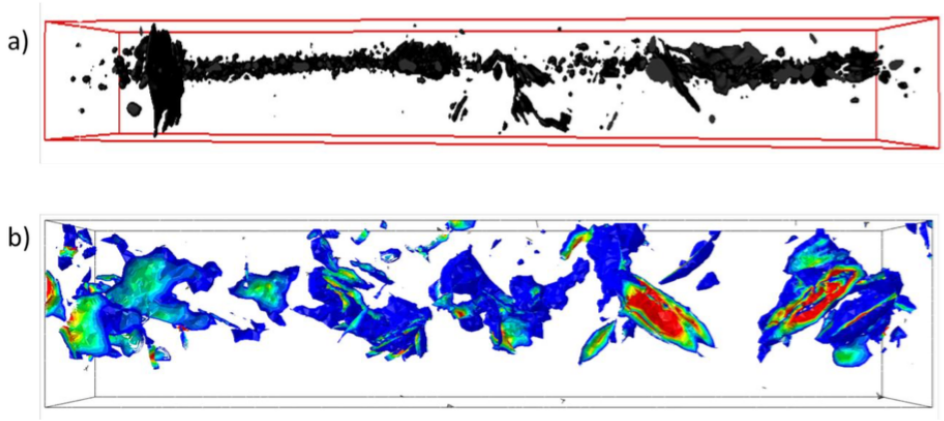


Figure 1.19. Spall damage in the multicrystal sample-front view (a) cross-sectional image of the damage zone observed experimentally (b) iso-surface plot of total void fraction obtained from simulation [5].

A brief introduction to shock, hydrodynamic instability experimental techniques to produce plasticity, and spall damage has been provided in the chapter above. Also, many constitutive (strength) models have been discussed to model plasticity in high strain

rate applications. Past and present studies on these topics provide fundamental understanding of shock loading, the development of a constitutive strength model, and spall damage initiation. All the experiments for hydrodynamic instabilities show that they have been conducted with ramps or shocks directed to ripples on the opposite surface of the sample, but no experiments seem to have the configuration using Piriz' models [13], a shock on ripples.

This research is an attempt to use Piriz' configuration [13] by directing a shock on ripples using laser energy. Because of the complexity of these experiments, most of the experimental data are limited to perturbation amplitude growth, which are used to validate a constitutive model, which is imperative to overcome the limitations in understanding the effects of geometry, loading conditions and strength on material behavior during shock loading. K. Krishnan [5] evaluated the incipient stages of nucleation for shock loaded copper bicrystals and multicrystals using a crystal plasticity framework with added Gurson-Tvergaard-Needleman (GTN) damage model. His models predicted that damage nucleated at or around microstructural weak links such as grain boundaries and triple junctions [5]. However, void nucleation observed at the triple junctions were not analyzed. This research work is also a continuation of Krishnan's [5] work, which scrutinizes void nucleation sites observed in triple junctions. The main objective of this research is to understand the effect of strength in perturbation amplitude and to collect the statistical data of triple junctions found on the damaged sites. The other important objectives of the research work are provided in the next chapter.

# 2. OBJECTIVES

This research will calibrate and validate an accurate isotropic material model that will be used to study the dynamics of shock loading and the effects of strength on material response under conditions leading to hydrodynamic stabilities and investigate microstructural conditions leading to nucleation of spall damage with emphasis on local crystallography. The objectives of this research work are as follows:

1. Study dynamic plasticity during shock loading through analysis of results from hydrodynamic instability experiments.

An explicit isotropic constitutive model will be used to study plasticity during shock loading by using the PTW model for the material's deviatoric response and the Mie-Grüneisen EOS for its volumetric response. The constitutive model will be implemented as a user subroutine (VUMAT) that can be used with the finite element code ABAQUS$^{TM}$/EXPLICIT.

2. Calibrate and validate the developed constitutive model.

Calibration of the material constants will be done using the best-fit technique. Best-fit technique will involve fitting the velocity history of flat samples to velocity histories obtained from experimental Velocity Interferometer System for Any Reflector (VISAR) results. A laser pulse was used during the experiment to create shock waves in the sample, whereas a pressure boundary condition will be used for the finite element simulation to replicate the laser pulse. The relationship between pressure boundary condition and laser energy will be obtained by calibrating the simulation velocity profile to the velocity profile measured experimentally through VISAR. Calibration of material

constants and derivation of the relationship between pressure boundary condition and laser energy will be performed simultaneously.

Validation of the model will be done by comparing experimental Transient Imaging Displacement Interferometry (TIDI) results with the simulated free surface perturbation evolution of rippled (perturbed) samples. As an experimental technique, TIDI can capture full-field out-of-plane surface displacement map in a single-slot with 180 ps time resolution, as given by the width of the illumination pulses. A framing high-resolution camera allows capturing up to 8-displacement maps for a single loading event by tracking the evolution of a surface motion. A spatially resolved VISAR (line-VISAR) is used as a complementary diagnostic that provided a continuous record of velocity history and also provided time stamps for the TIDI displacement map.

3. Use the developed constitutive model to study the effects of strength on hydrodynamic instability growth.

Evolution of free surface amplitude will be evaluated by performing 2-D finite element simulations of rippled (perturbed) samples at different strengths. The effects of different strengths on simulation results and hydrodynamic instability growth will be elucidated.

4. Further analyze the damage sites found in copper multi-crystal simulation performed by K. Krishnan [5].

Void nucleation at an incipient stage around triple junctions as predicted by crystal plasticity simulations will be assessed and compared to experimental results. Statistical analysis of damage at triple junctions will be performed and compared with statistical data from L. Wayne [22] and A. Brown [58].

# 3.EXPERIMENTAL AND MODELING PROCEDURES

## 3.1. Experimental Technique

### 3.1.1. Novel RM Instability Experiment Set-up

Experimental data obtained from new RM instability experiment is used for simulation model calibration and validation. All shock-loading experiments for this research work were carried out at The Trident Laser Facility at Los Alamos National Laboratory (LANL) by Eric Loomis and his colleagues. The physics of the instability experiments is dominated by hydrodynamics, where the surface perturbations at the incident shocked surface of a sample produced a perturbed shock front that is 'fed-thru' the sample to a flat free surface. The flat free surface subsequently developed a perturbed surface as the perturbed shock front broke out and then grew via the RM instability.

Therefore, LANL used the RM Instability to measure strength effects in polycrystalline copper with a novel approach whereby the shock was applied directly on a perturbed surface using laser ablation and producing a perturbed shock that propagated through the specimen thickness. This experiment is novel because all the experiments conducted in the past had a configuration where the perturbation in the sample was at the rear surface, directing the shock from the flat surface to the perturbed surface whereas a 'feed-thru' technique was used in this experiment. Figure 3.1 shows schematic of a typical experimental set-up at the Trident Laser Facility and the dynamic diagnostics used during testing.

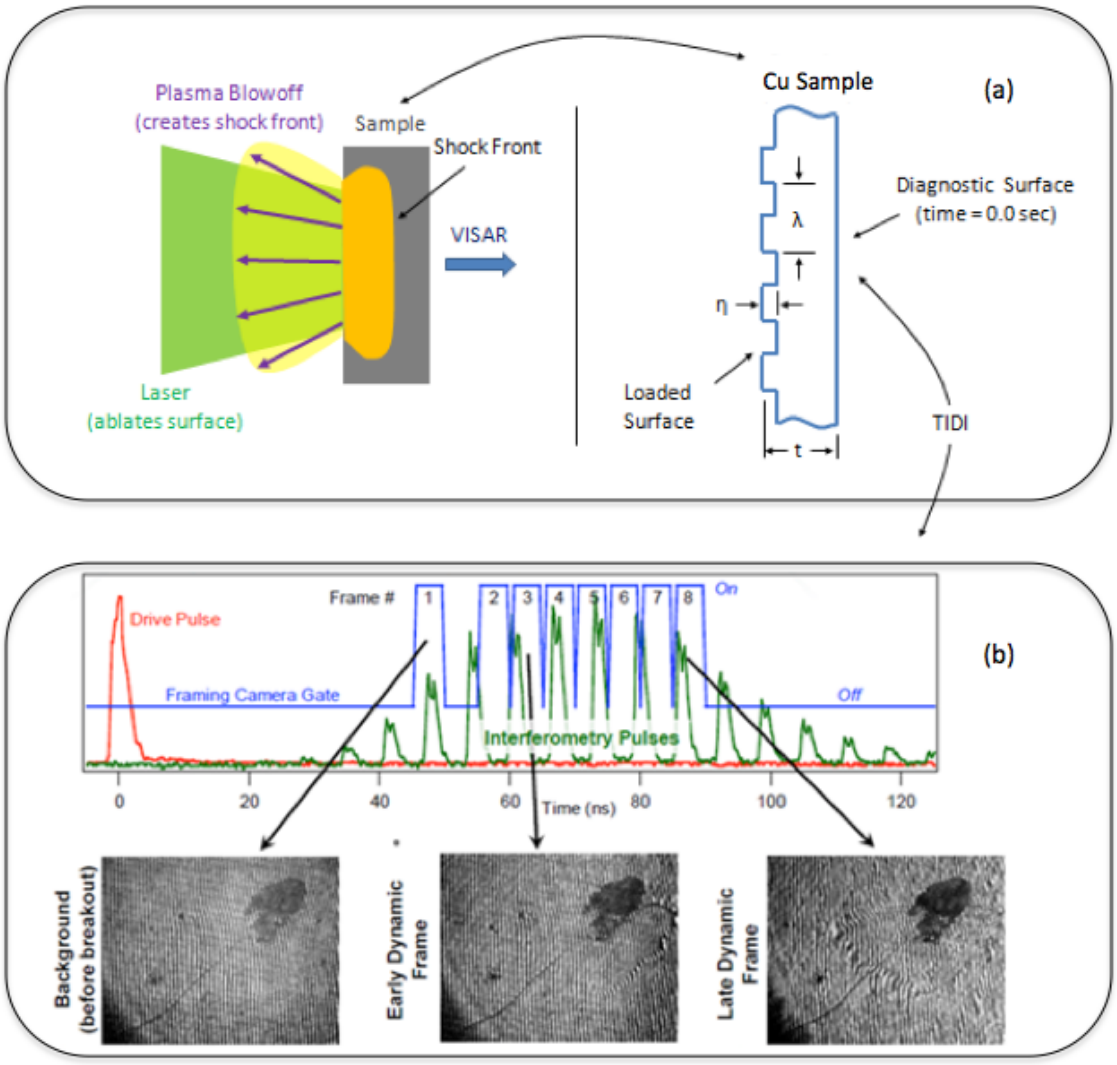


Figure 3.1. Schematic showing experimental setup and diagnostics. (a) Laser ablation and sample configuration. (b) Pulse train of laser illumination to capture TIDI data with framing cameras and example images.

In the RM instability experiment shown in figure 3.1, a laser beam was used to ablate a thin layer on the surface of the sample that created plasma and gas, the expansion of which against the surface of the sample produced an equal reaction shock wave in it. Given that the ablated surface of the sample was perturbed (square rippled-explained in next section), a perturbed shock front was created that propagated through the sample. This perturbed shock front oscillated in time and space [28] eventually reaching the free

surface (rear surface) of the sample also as a perturbed shock, but likely with a different amplitude than that determined by the initial perturbation. The perturbed shock imprinted a perturbation once it reached the free surface that then grew via the RM instability. The evolution of the velocity and displacement of the originally flat free surface was monitored directly using diagnostics such as line VISAR [32] and TIDI [54-56] respectively. In these experiments, TIDI is specifically advantageous for measuring small disturbances that evolve at the flat surface [54-56] and it is well suited to capture the evolution of instability at early times, while they are still in the linear or weakly non-linear regime. Radiography diagnostics are commonly used for hydrodynamic instability experiments to calibrate and validate strength models; however, one of the advantages of using TIDI in this experiment is that it has better sensitivity than radiography [54-56].

The experimental technique applied for this research is different from the typical RM technique in the sense that the laser pulse used for the wave formation is very short (~ 7 ns) and as a result, the analysis outlined in the previous section is only applicable during a short period of the experiment. Also, as mentioned earlier the feed-thru technique used in this experiment is novel. Figure 3.1 (a) shows in detail the laser ablation set-up and geometrical configuration of the sample. As can be seen from figure 3.1(a), the perturbed surface was ablated and the free surface was probed by the TIDI and VISAR diagnostics. Figure 3.1 (b) is a generic representation of the pulse train of laser illumination used to capture TIDI data with framing cameras and example of typical images. Frame number 1 is the static image of a free surface before the shock breakout whereas the other frames show the images captured at different times after the shock breakout. The TIDI diagnostic at Trident used laser pulses separated by 6.5 ns. So to

capture the dynamic data within and after the 7 ns drive pulse, two consecutive illumination pulses were used.

Laser energy was used to control the shock pressure induced in the sample during dynamic loading. The short laser pulse of ~ 7 ns produced pressures in the range of 9-18 GPa in copper, with laser energies in the range of 13-36 J. The laser beam was focused to a spot size of about 1 mm and made square in shape by the use of a phase plate. Two sample geometries were used for this investigation. Flat samples with a thickness of ~100 μm were tested first. The results from testing these samples were used to correlate a known laser intensity pulse and the resulting free surface velocity history to a pressure boundary condition profile via numerical simulation. Several laser energies were used for this calibration. Velocity profile measurements were made using Line VISAR system.

The second geometry considered for this analysis is a perturbed sample (shown in figure 3.1(a)). The preparation technique for the perturbation will be described in the next section. The ablated perturbations produced a perturbed shock front that imprinted the initially flat free surface with a perturbation of its own at breakout which, in turn, resulted in an RM instability. Velocity and displacement measurements on the diagnostic surface, again, the one opposite to the rippled ablated one, were made using Line VISAR and TIDI, respectively.

### 3.1.2. Sample Preparation

All samples for this work were fabricated from a rolled plate of high-purity Hitachi copper (99.995%). The specimens were shaped like disks. Dedicated experimentalists at ASU performed the photolithography process at ASU's Center for

Solid State Electronics Research (CSSER) to produce the surface perturbations [18]. Square waves with a wavelength of 150 $\mu m$ were created on one of the surfaces of the sample via columnar photomask pattern. These samples were then polished within $\pm 10$ % of the desired thickness and were finished with 0.05$\mu m$ colloidal silica suspension. The back and front surfaces of all samples were kept flat and parallel with a tolerance of about 0.1 °.

### 3.1.3. Experimental Results

Figure 3.2 shows experimental results obtained from line VISAR and TIDI diagnostics.

Figures 3.2 (a) and (b) are the Line VISAR interferograms obtained for flat and rippled samples, respectively. The horizontal axis is space ($x$ in $\mu m$) and vertical axis is time ($t$ in $ns$) increasing downwards. The VISAR data was collected during a window of about 50 ns and the line was about 1 mm long. Both interferograms have time fiducials that are 6.5 ns apart, which were obtained from pulses used for TIDI illumination. The shift of vertical fringes in Figure 3.2(a) indicates the time at which the shock front reached the free surface. Figure 3.2(b), on the other hand, shows two different fringe shifts in time, which indicates that the shock front does not arrive at the same time to the free surface everywhere. This is to be expected, since ablation of the perturbed surface produces a rippled shock front, and the time difference in the VISAR record should correspond to the difference in arrival time between the peak and valley of this perturbed shock front. This time difference can be measured directly from the Line VISAR plot interferogram of a perturbed sample.

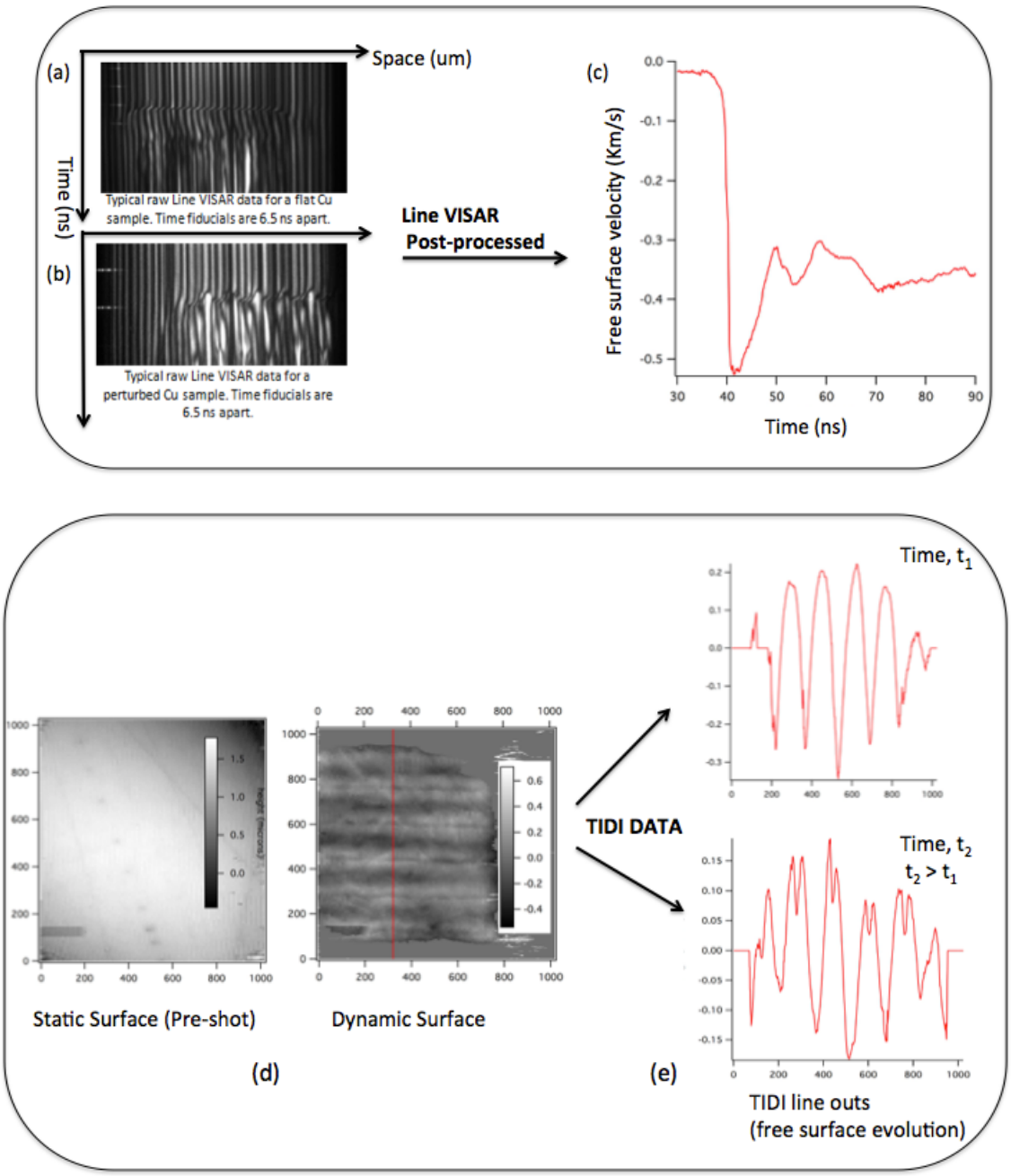


Figure 3.2. Schematic showing raw experimental data and their post processing. (a) Line VISAR from a flat sample, (b) Line VISAR from a rippled samples, (c) Post-processed velocity history from VISAR, (d) Pre-shot (static) and post-shot (dynamic) TIDI images, and (e) TIDI post-processed out-of-plane displacement at the free surface at two different times.

Figure 3.2(c) is a typical velocity history obtained from the raw VISAR data for a flat sample. Velocity records for rippled samples were much harder to analyze, since the free surface evolves from an initially flat surface to a perturbed surface with a wavelength equal to the original perturbations, whereas for flat samples the whole surface accelerates with the shock front arrival and decelerates with the release wave. The velocity histories obtained from flat samples were, therefore, used for the calibration of pressure boundary conditions as a function of laser energy and also for calibration of the material model. However, in the perturbed sample data from TIDI pre and post-shot images (shown in figure 3.2(d)) were used to characterize the evolution of the perturbation imprinted on the free surface by the rippled shock front. Figure 3.2(e) represents two line profiles showing out-of-plane displacements at two different times obtained from the TIDI images shown in Figure 3.2(d).

In figure 3.2(e), at time $t = t_1$, the perturbation showed only one harmonic, at the same frequency as the initial perturbation made on the sample, whereas at time $t = t_2$, with $t_2 > t_1$, one can see a second harmonic along with the first, which indicates that perturbations evolve higher harmonics with time. This is believed to be a result of the interaction of the perturbed surface with the perturbed release wave after the shock front reaches the free surface, which is explained in detail in the results and discussion section.

## 3.2. Finite Element Modeling

The finite element model used comprises a 2-D simulation of polycrystalline copper samples by implementing a PTW strength model in an isotropic hypoelastic constitutive framework with a Mie-Grüneisen EOS via a fortran subroutine within

ABAQUS™ built-in co-rotational framework [71-72]. Two-dimensional, 4-node bilinear quadrilateral plane strain elements were used for all the simulations. All 2-D simulations were performed in ABAQUS™ using a Lagrangian dynamic explicit analysis. The details of the constitutive model development are discussed in subsequent chapters. Given that a laser pulse was used during the experiment to create shock wave in the sample and that it generated a pressure wave that propagated from the absorption region, a pressure boundary condition is therefore used for the finite element simulation to replicate this laser pulse. Figures 3.3 and 3.4 show the 2-D geometry of a sample and the boundary conditions applied.

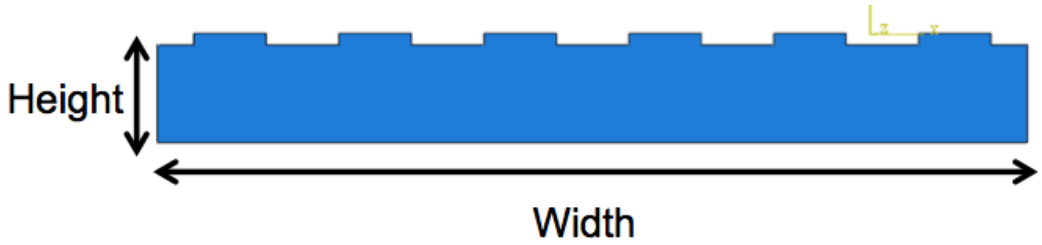


Figure 3.3. Schematic showing the geometry of a perturbed (rippled) sample in ABAQUS™.

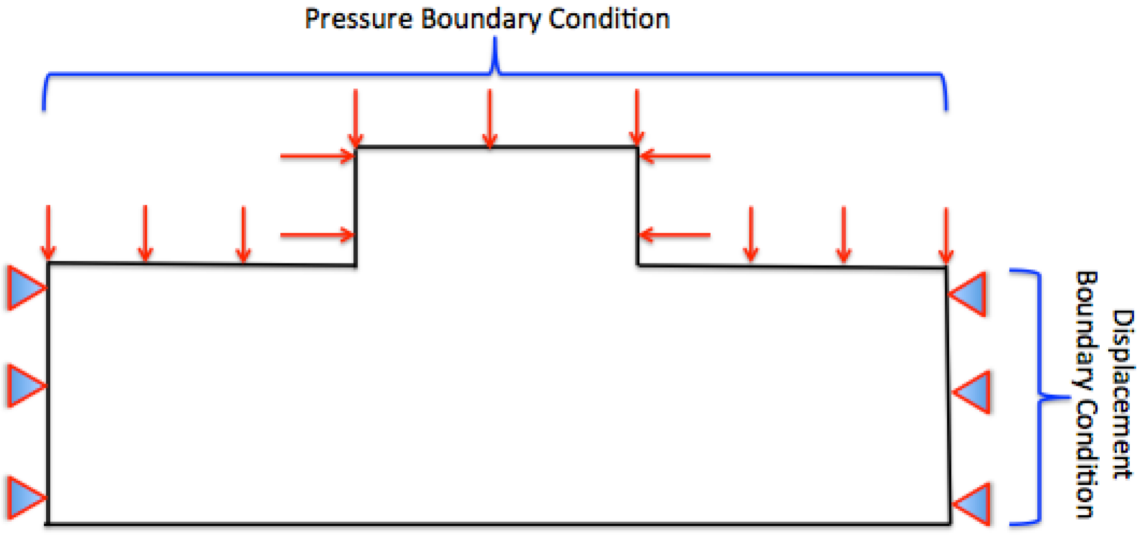


Figure 3.4. Applied boundary conditions.

A mesh-convergence study was first performed to obtain the optimal element size for the finite element analysis. The geometry considered for this investigation was truncated where a single wavelength was considered (shown in figure 3.4). The total simulation time for this study was set to $50\ ns$. An element size sweep was carried out for the mesh-convergence study. Stress is more sensitive to the solution than displacement as it is a second order derivative of displacement and is more accurate; therefore, maximum von Mises stress is used to study the convergence of the solution with the different mesh sizes. The element sizes ranged from $1.0\ to\ 0.01\ \mu m$. Figure 3.5 shows the stress convergence for various element sizes.

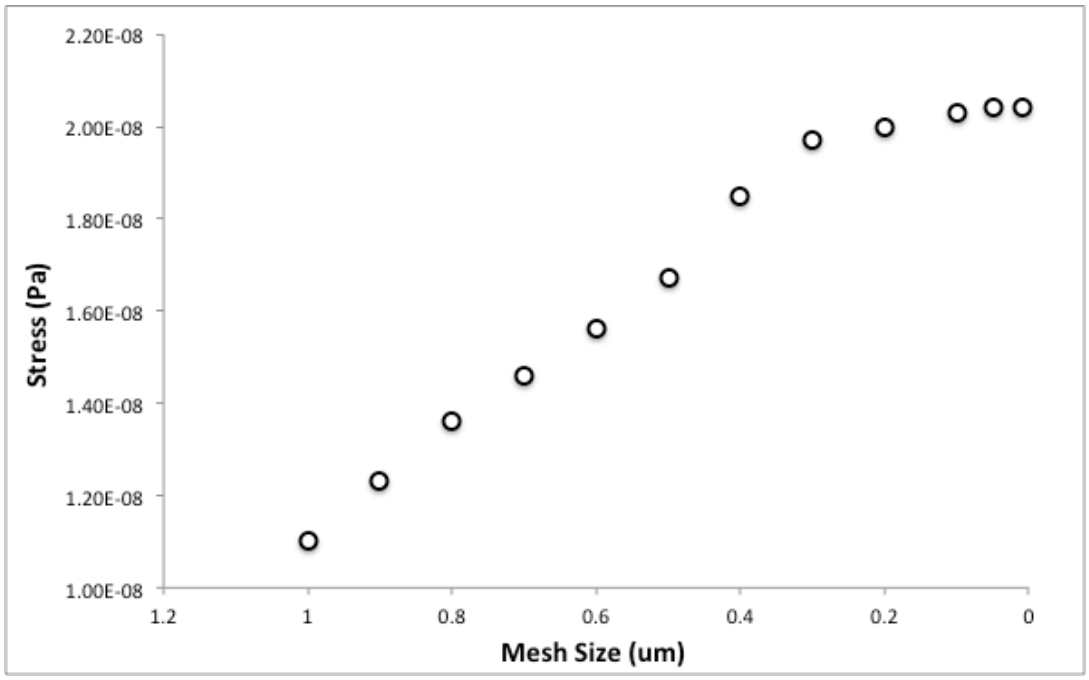


Figure 3.5. Stress convergence for different base element sizes.

From figure 3.5, it can be seen that the stress values start converging for a base element size of $0.3\ \mu m$. A base element size of $0.1\ \mu m$ was considered as the optimal element size. The mesh for the sample with $0.1\ \mu m$ elements is shown in figure 3.6 (b).

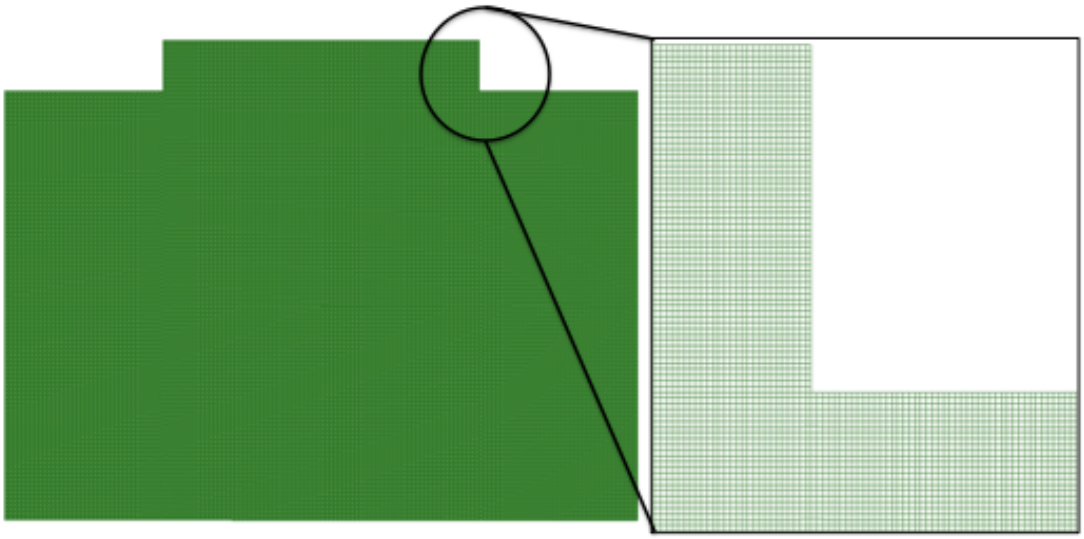

Figure 3.6. (a) Geometry considered for the mesh convergence study; (b) Zoomed in picture of the chosen optimal mesh size ($\mathbf{0.1\ \mu m}$).

The time step for each solution was automatically calculated through the ABAQUS$^{TM}$ explicit solver [71-72]. The stable time increment size is defined as the smallest transit time of a dilatational wave across any of the elements in the mesh given by [71-72]

$$\Delta t \approx \frac{L_{min}}{c_d} \tag{3.1}$$

where $L_{min}$ is the smallest element size in the mesh and $c_d$ is the dilatational wave speed. The current dilatational wave speed $c_d$ is determined in ABAQUS$^{TM}$/Explicit by calculating the effective hypoelastic material moduli from the material's constitutive response [71-72]. The actual stable time increment chosen by ABAQUS$^{TM}$/Explicit will be less than equation (3.1) by a factor between $1/\sqrt{2}$ and 1 in a two-dimensional model and it also accounts for stiffness behavior in a model associated with penalty contact [71-72].

Shock waves are mathematically treated as discontinuities; however, this causes problems for numerical solutions. Physically, a shock wave is a very narrow transition

zone the thickness of which is on the order of a few molecular mean-free paths. Application of conservation of mass, momentum, and energy condition across a shock wave requires a transformation of kinetic energy into heat energy, which is represented as viscous dissipation. An artificial increase in this value of viscosity to thicken the shock transition zones stabilizes the numerical solution. Finite element simulations performed in this research work used the PTW strength model, which already induces significant viscous dissipation. Therefore, a very small value of 0.02 for linear and 0.2 for quadratic bulk viscosity was used for numerical stability in ABAQUS$^{TM}$ [71-72].

# 4. CONSTITUTIVE FRAMEWORK

## 4.1. Overview

Plasticity produced by shock loading is a complex physical process that is strongly dependent on the load application and the material [4,65,67,69,73-77]. Figure 4.1 shows the different aspects of material behavior that can affect a velocity history profile [2]. This research only focuses on the process of plasticity that eventually leads to spall failure, but does not include the spallation itself in order to better understand the material plastic behavior during compression, which conditions the material for spall. Some phenomena such as phase transitions are neglected due to low to medium applied pressures that do not induce phase transformations in copper.

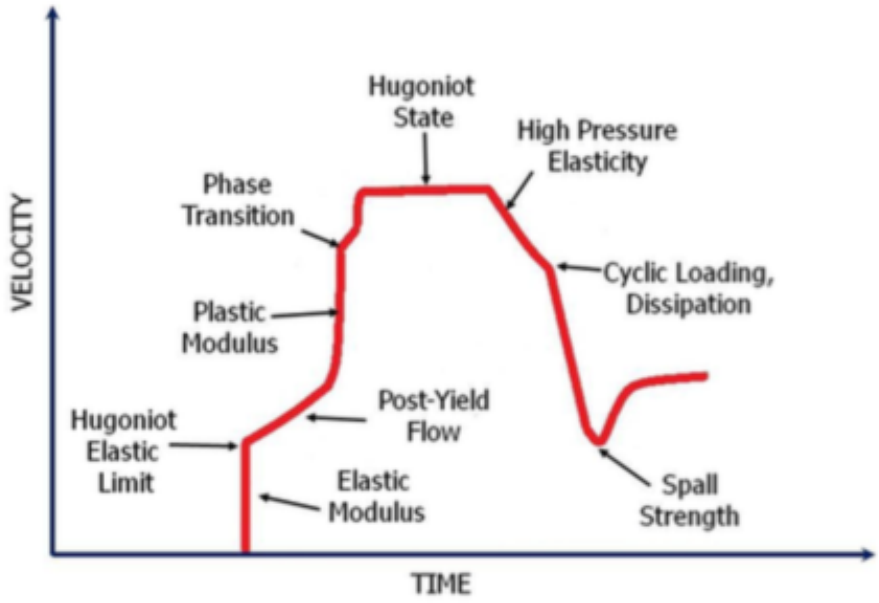


Figure 4.1. Generic velocity history profile for shock loading showing the different aspects of material behavior that affect the dynamic response [2].

A constitutive model needs to be developed that can accurately predict metal plasticity during shock loading for the purpose of this work. The process involves various

different physical phenomena such as strain rate dependence of properties, elastic and plastic processes, loading history, anisotropy, intrinsic, and extrinsic effects, such as the presence of inclusions or precipitates. This research only focuses on macroscopic plasticity, which can and will be assumed to be isotropic in nature in this case and hence the effects of microstructure and anisotropy will be neglected.

The main objective of the constitutive model is to calculate a stress response for a given deformation history. In this research, the constitutive framework includes the combination of an isotropic strength model with an equation of state. An Equation of State (EOS) is used to incorporate the pressure-volume-energy relations for the shock loading calculations. One of the most commonly used EOS for metals is the Mie-Grüneisen EOS. The following subsections outline the approach used for the implementation of the constitutive framework.

### 4.1.1. Isotropic Strength Model

The inelastic response of the material studied in this research, copper, is modeled by using a hypoelastic based model. In contrast to hyperelasticity models [78], which are valid at large elastic strains, hypoelastic-based models do not rely on the assumption of the existence of a free-energy potential to model the reversible behavior. Many researchers have investigated and documented the limitations of hypoelastic material models for the large elastic shear (deviatoric) strains that can produce significant integration errors for a large number of stress cycles [79-82]. However, most metals have small elastic shear strains, therefore, it is safe to use hypoelastic-based theory for the material model. Also, large hydrostatic stresses and volumetric strains are accounted by

the EOS and are independent of deviatoric stress, which allows hypoelastic-based theory in this research for the constitutive framework.

This material model is implemented via a fortran subroutine with ABAQUS$^{TM}$ built-in co-rotational framework, specifically the Green-Naghdi stress rate [71-72].

With the assumption of isotropic elasticity and small elastic shear strains, the stress-strain constitutive relation can be expressed in the form of an objective stress rate, which is given by

$$\sigma^{\nabla} = C^*: D_e \tag{4.1}$$

where $\sigma^{\nabla}$, is an objective stress rate that can be selected from a variety of choices [79-81], $C^*$ is a pressure and temperature dependent material elastic stiffness tensor, and $D_e$ is the spatial (Eulerian) elastic deformation rate.

An objective stress rate consistent with the one needed for this work can be derived from the assumption of an elastic stress-strain relationship on a Lagrangian framework between the Second Piola-Kirchoff Stress (PK2) tensor *S* and the Green strain $E_e$ such that $S = C^*(P,T): E_e$. The rate of the PK2 stress is given by

$$\dot{S} = \dot{C}^*(P,T): E_e + C^*(P,T): \dot{E}_e \tag{4.2}$$

where $\dot{S}$ is the PK2 stress rate

With an elastic push forward of equation (4.2) using the elastic deformation gradient, $F_e$, the assumption of small elastic shear strains, which means that $F_e$ is approximately orthogonal, and isotropic behavior, equation (4.2) can be reduced to equation (4.1), which leads to the general hypoelastic relation for an isotropic material used in this work. The push forward of the PK2 stress rate leads to the Truesdell rate given by

$$\sigma^{\nabla} = \dot{\sigma} - L\dot{\sigma} - \sigma L^{T} + (trL)\sigma \tag{4.3}$$

where $L$ is the velocity gradient, $\sigma$ is the Cauchy stress.

From equation (4.1) and (4.3), we have the evolution of stress tensor that is governed by a constitutive law of the form

$$\sigma^{\nabla} = \dot{\sigma} - L\dot{\sigma} - \sigma L^{T} + (trL)\sigma = C^{*}: D_{e} \tag{4.4}$$

In ABAQUS™, the constitutive equation is formulated in a co-rotational framework based on Green-Naghdi stress rate, which is given by [71-72]

$$\sigma^{\nabla} = W\sigma - \sigma W + C^{*}(P,T): D_{e} \tag{4.5}$$

where $W$ is the spin tensor or the skew symmetric part of the velocity gradient *L*.

Stress is separated into deviatoric and hydrostatic (volumetric) parts. Deviatoric stresses are incremented proportionally to the increment of strain deviators. A trial stress increment is chosen to update the stresses where the new trial stress is given by

$$\sigma'^{trial}_{new} = \sigma_{old} + 2G\Delta\varepsilon' \tag{4.6}$$

where $\Delta\varepsilon'$ is deviatoric strain increment obtained from ABAQUS, G is the shear modulus.

If the deviatoric stress calculated from equation (4.6) is greater than the flow stress obtained from PTW strength model, then plasticity is present. The next step is to solve for plastic strain rate ($\dot{\varepsilon}^{p}$). Calculation of strain rate and effective strain rate follow equations (4.7-4.22) [83].

Hooke's law of isotropic material in terms of stress and strain tensor is given by

$$\sigma = 2G\varepsilon^{e} + \lambda\, tr(\varepsilon^{e})I \tag{4.7}$$

where $G$ and $\lambda$ are the Lame's constants.

The elastic strain at the end of time step is given by

$$\varepsilon^e = \varepsilon_t^e + \Delta\varepsilon^e = \varepsilon_t^e + \Delta\varepsilon - \Delta\varepsilon^p \tag{4.8}$$

So that the stress is given by

$$\sigma = 2G(\varepsilon_t^e + \Delta\varepsilon - \Delta\varepsilon^p) + \lambda\, tr(\varepsilon_t^e + \Delta\varepsilon - \Delta\varepsilon^p)I \tag{4.9}$$

$$\sigma = 2G(\varepsilon_t^e + \Delta\varepsilon) + \lambda\, tr(\varepsilon_t^e + \Delta\varepsilon)I - 2G\Delta\varepsilon^p \tag{4.10}$$

Elastic predictor of the trial stress is denoted by

$$\sigma^{tr} = 2G(\varepsilon_t^e + \Delta\varepsilon) + \lambda\, tr(\varepsilon_t^e + \Delta\varepsilon)I \tag{4.11}$$

and therefore equation (4.11) can be written as

$$\sigma = \sigma^{tr} - 2G\Delta\varepsilon^p \tag{4.12}$$

which can be re-written as

$$\sigma = \sigma^{tr} - 2G\Delta\gamma\frac{3\sigma'}{2\sigma_e} \tag{4.13}$$

where $\Delta\gamma$ is the incremental effective plastic strain and $\sigma_e$ is the effective von-mises stress and is given by

$$\sigma_e = \sqrt{\frac{2}{3}\sigma' : \sigma'} \tag{4.14}$$

The stress is expressed in terms of deviatoric and hydrostatic (volumetric) stresses as

$$\sigma = \sigma' + \frac{1}{3}(\sigma : I)\, I \tag{4.15}$$

so that we obtain

$$\sigma' + \frac{1}{3}(\sigma : I)\, I = \sigma^{tr} - 2G\Delta\gamma\frac{3\sigma'}{2\sigma_e} \tag{4.16}$$

which gives

$$\left(I + 3G\frac{\Delta\gamma}{\sigma_e}\right)\sigma' = \sigma^{tr} - \frac{1}{3}(\sigma : I)\, I \tag{4.17}$$

Using equation (4.16), we can say that $\sigma' - \frac{1}{3}(\sigma : I)\, I$ is just a deviatoric trial stress and then equation (4.17) is reduced to

$$\left(I + 3G\frac{\Delta\gamma}{\sigma_e}\right)\sigma' = \sigma^{tr\prime} \tag{4.18}$$

If we take the contracted tensor product of each side with itself, we get

$$\sigma^{tr\prime}:\sigma^{tr\prime} = \left(I + 3G\frac{\Delta\gamma}{\sigma_e}\right)^2 \sigma':\sigma'$$

$$\left(I + 3G\frac{\Delta\gamma}{\sigma_e}\right)\sigma_e = \left(\frac{3}{2}\,\sigma^{tr\prime}:\sigma^{tr\prime}\right)^2$$

$$\left(I + 3G\frac{\Delta\gamma}{\sigma_e}\right)\sigma_e = \sigma_e^{tr} \tag{4.19}$$

Equation (4.19) finally gives

$$\sigma_e^{tr} - 3G\Delta\gamma = \sigma_e \tag{4.20}$$

Effective strain rate ($\dot{\gamma}$) is needs to be calculated in order to compute equation (4.20). A function $F$ is defined such that

$$F = \sigma_{flow\ stress} - \sigma_e \tag{4.21}$$

where $\sigma_{flow\ stress}$ is the stress obtained from the PTW strength model. Equation (4.21) can be re-written as

$$F = \sigma_{flow\ stress} - (\sigma_e^{tr} - 3G\Delta\gamma) \tag{4.22}$$

Finally the effective plastic strain rate ($\dot{\gamma}$) was obtained by minimizing the absolute value of function ($F$). The minimization of $F$ was done using Newton Raphson method. The volumetric part of the stress is calculated from the equation of state.

### 4.1.2. Mie-Grüneisen Equation of State

One of the most commonly used Equations of State (EOS) in shock loading applications is the Mie-Grüneisen (M-G) EOS, which relates a state of pressure, volume,

and energy to a Hugoniot state of pressure ($P_H$) and energy ($E_H$) at the same specific volume $v$. The Mie-Grüneisen EOS for low to medium shock loading is given as [2]

$$P(v,E) = P_H(v) + \frac{\Gamma}{v}\left(E - E_H(v)\right) \tag{4.23}$$

If we take the partial derivative of equation (4.23) with respect to temperature, we get

$$\left(\frac{\partial P}{\partial T}\right)_v = \frac{\Gamma}{v}\left(\frac{\partial E}{\partial T}\right)_v \Rightarrow \Gamma = v\left(\frac{\partial P}{\partial T}\right)_v \left(\frac{\partial T}{\partial E}\right)_v \Rightarrow \Gamma = \frac{v}{C_v}\left(\frac{\partial P}{\partial T}\right)_v \Rightarrow \Gamma = -\frac{v}{C_v}\left(\frac{\partial P}{\partial v}\right)_T \left(\frac{\partial v}{\partial T}\right)_P$$

……. (4.24)

where $\frac{1}{v}\left(\frac{\partial v}{\partial T}\right)_P = 3\alpha$ is the volumetric thermal expansion and $-\frac{1}{v}\left(\frac{\partial v}{\partial P}\right)_T = K$ is isothermal compressibility. Equation (4.24) can be re-written as

$$\frac{\Gamma}{\nu} = \frac{3\alpha}{C_\nu K} \tag{4.25}$$

Γ is the Gruneisen material parameter and is often assumed that it can be approximated by

$$\Gamma = \Gamma_0 \frac{\rho}{\rho_0} \Rightarrow \frac{\Gamma}{v} = \frac{\Gamma_0}{v_0} \tag{4.26}$$

$\Gamma_0$, $v_0, \rho_0$ are the Grüneisen parameter, specific volume, and density at zero pressure, respectively

The Hugoniot state of energy $E_H$ and pressure $P_H$ are calculated at the constant $v$ found in equation (4.23). The experimentally obtained linear relationship representing shock velocity ($U_s$) as a function of particle velocity ($U_p$) given by [2]

$$U_s = C_0 + sU_p \tag{4.27}$$

where $s$ is empirical parameter that describes the slope of the $U_s - U_p$ line and $C_0$ is an isentropic bulk sound speed at zero pressure.

Equation (4.27) when combined with the conservation equations describing the jump conditions across the shock front provide expressions for pressure and energy along the Hugoniot path [16].

$$E_H(v) = \frac{P_H \eta}{2\rho_0} \text{ and } \eta = 1 - \frac{\rho}{\rho_0} = 1 - \frac{v}{v_0} \tag{4.28}$$

and the Hugoniot pressure is defined as [2]

$$P_H(v) = \frac{\rho_0 C_0^2 \eta}{(1-s\eta)^2} \tag{4.29}$$

Equations (4.28-4.29) are a fit to a materials *P*-*v* (or equally *E*-*v*) Hugoniot, an intrinsic property of the material for a given reference point. In equations (4.28-4.29) the reference point is at zero pressure. The MG-EOS, Equation (4.23), then allows one to calculate a pressure for a material state, i.e. a (*E,v*) pair, that is off the known Hugoniot described by equations (4.28-4.29). The MG-EOS typically assumes material parameters (e.g. $C_v$, $\frac{\Gamma}{v}$, $K$) to be constant or temperature independent. When temperature changes are large this can obviously introduce issues. Finally the MG-EOS has a bounded (*E,v*) range for which it is valid, i.e., see [49, p. 136] for further details.

# 5. CALIBRATION AND VALIDATION

A constitutive model can only be used to study and predict behavior once it is calibrated and validated with reliable experimental data. Validation is a primary method to gain confidence in accurately predicting the physics of constitutive model by comparing the numerical solution with experimental data. Calibration is done to fine-tune the material parameters in the model to fit the experimental data and usually precedes the validation. Once all the material parameters are fine-tuned to fit the experimental data, the same parameters are used to validate and compare the numerical solution with many other experimental data that are not used in the calibration process. This process is explained in detail in the next section.

## 5.1. Calibration of Material Constants

Calibration of PTW strength model parameters to obtain a good agreement between the simulation and experimental velocity profiles involved two simultaneous operations- 1) Obtaining the relationship between applied laser energy and pressure boundary condition on the ablation surface and 2) Calibration of the PTW material constants. A basic trapezoidal pressure pulse with 5 ns duration was used as a reference pressure boundary condition for the simulation to replicate the experimental laser pulse (approximately 5 ns) condition. Figure 5.1 shows the reference trapezoidal boundary condition considered for the simulation.

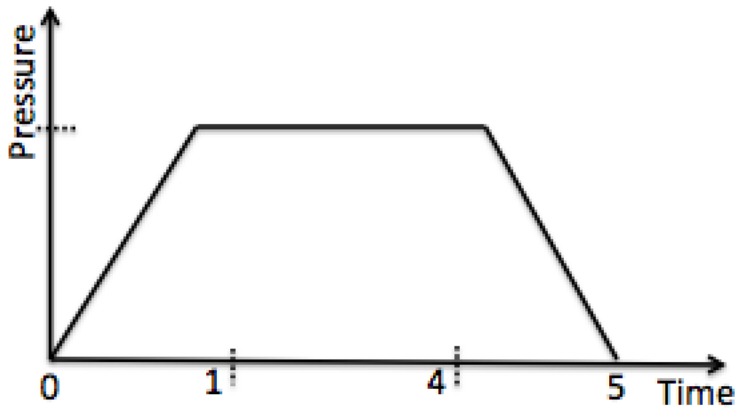


Figure 5.1. Reference pressure boundary condition profile used for the simulation.

To better understand the effect of each parameter on the PTW material model, which incorporates large pressure and high strain rates, a point integrator code developed in MATLAB was used to obtain a yield stress versus strain rate plot. This code uses isotropic properties and the Mie-Grüneisen Equation of State. Each set of PTW material parameters was changed to see its impact in a yield stress versus strain rate plot. Figure 5.2 provides a schematic of how different material parameters influence the PTW model, where material constants $S_0$and $S_\infty$ are the values that $(\hat{\tau}_s)$ work hardening saturation stress takes at zero and very high temperatures, respectively. $Y_0$ and $Y_\infty$ are the material constants values that are taken by $(\hat{\tau}_y)$ yield stress at zero and very high temperatures, respectively. As shown in figure 5.2, the PTW response plot shows thermal activation, transition and drag regimes. As shown from the dashed and solid lines, increasing plastic strain increases thermal activation regime for the same strain rate; however, the phonon drag curve in the athermal region merges for all plastic strains. Hence, the dashed line represents thermal activation with lower work hardening while the solid line above it is thermal activation with higher work hardening (saturation). The slope for the thermal

activation curve is set by kappa $(k)$, the transition from thermal to drag region is given by the material constants $Y_1, Y_2$ and the strain rate $(\dot{\varepsilon})$. Material parameters $Y_1$ and $Y_2$ allow the maximum work hardening yield stress in the small strain rate sensitivity region. The athermal region in the PTW response is set by strain rate $(\dot{\varepsilon})$ and exponent $(\beta)$.

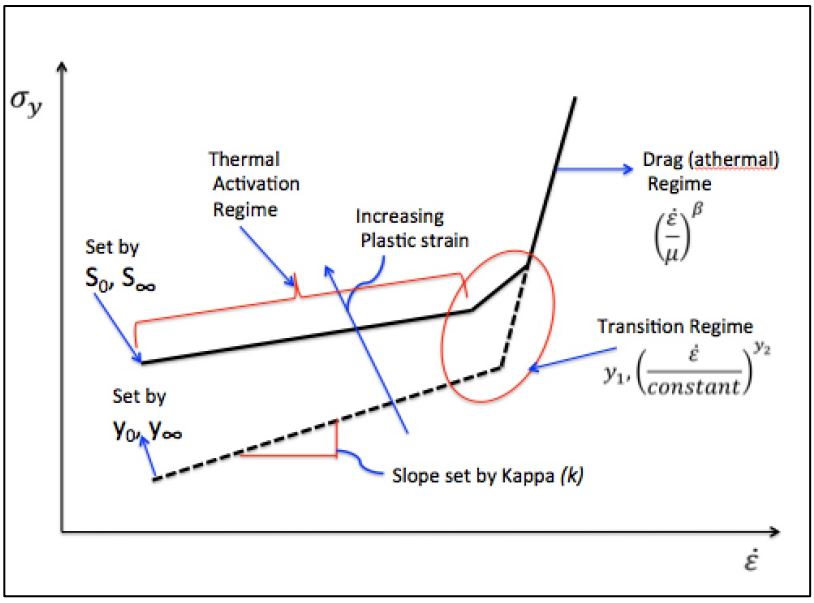


Figure 5.2. Schematic of how material parameters influence PTW response.

Figure 5.3 is a typical PTW response plot showing yield stress versus strain rate for different plastic strains, which was obtained from the code developed in MATLAB.

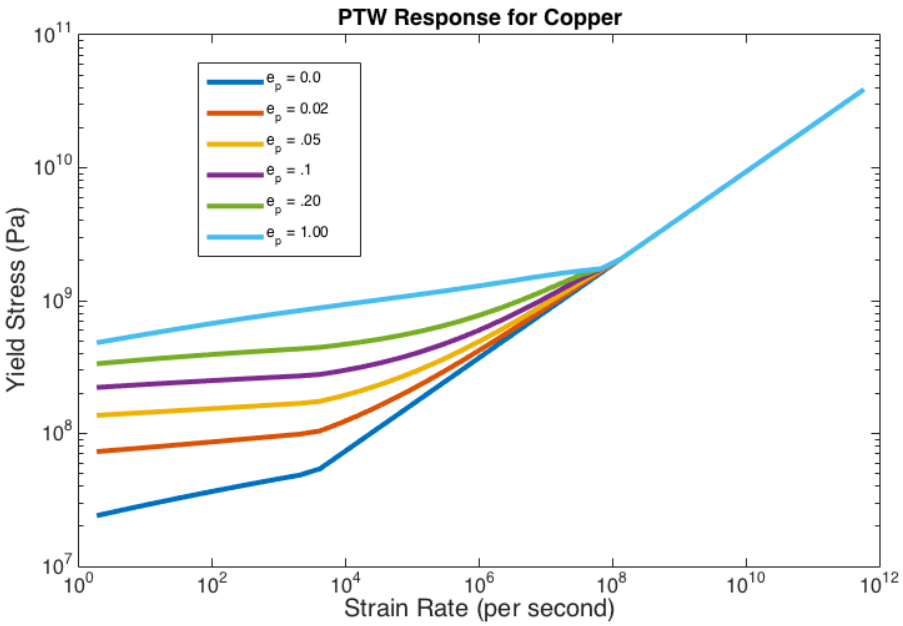


Figure 5.3. Typical PTW response plot at a temperature of 300 K.

Reference PTW parameters were obtained from [41] and were used for preliminary finite element simulations. Since the reference PTW parameters did not match the slope of a shock front correctly, calibration of these parameters was performed by carefully changing those parameters responsible for the change in the slope of the shock front and initial release. Calibration of these parameters was done for flat copper samples using the best-fit technique. The best-fit technique involved the comparison of $R^2$ values of experimental velocity profile obtained from VISAR and simulated velocity profiles using reference and calibrated PTW parameters. The parameter $R^2$ is a statistical representation of the closeness of two data sets. If the differences between the observed values and the predicted values are small and unbiased, the model fits the data well and results in $R^2 \approx 1$.

Appropriate PTW material parameters were calibrated by comparing the simulated velocity history results with experimentally obtained velocity measurements

from VISAR for flat samples, and, simultaneously, the relationship between applied laser energy and pressure pulse was established. The relationship between the pressure and laser energy was found to be represented well by a quadratic polynomial. Theoretically, the energy can be translated into pressure using Lindl's equation [95]

$$P = K \left(\frac{I}{\lambda}\right)^{2/3} \tag{5.1}$$

where $P$ is the pressure in Pa, $I$ is the laser intensity in $w/m^2$, $K$ is constant, and $\lambda = 523\ nm$ is the wavelength in $m$. Laser intensity $(I)$ is defined as

$$I = \frac{\text{Laser Energy}}{\Delta t\ A} \tag{5.2}$$

where $\Delta t = 5\ ns$ is the laser pulse, and $A = 0.01\ cm^2$ is the area. Using equations (5.1) and (5.2), pressure was derived and compared with calibrated pressure. Calibrated pressure is in good agreement with theoretically determined pressure using Lindl's equation. Figure 5.4 (a) shows the quadratic relationship of calibrated pressure with laser energy and figure 5.4 (b) shows the comparison of calibrated pressure to pressure obtained from Lindl's equation.

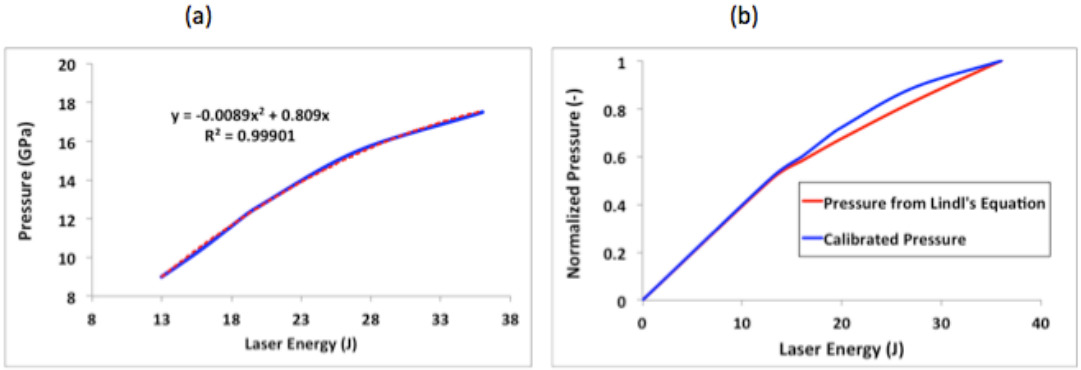


Figure 5.4. Pressure-laser energy relationship (a) calibrated (b) comparison of pressure obtained from Lindl's equation and calibration.

Once the PTW parameters were calibrated to fit the experimental velocity history profile of a flat sample, the applied pressure pulse from the same simulation was used to develop the pressure-energy relationship. These calibrated parameters with a pressure pulse derived from the pressure-energy relation were then used for the simulation of rippled (perturbed) samples, without further adjustments. Table 5.1 provides the details of geometry and shock conditions of all the samples simulated (in this research) along with the measured pressure-energy relation.

Table 5.1: Geometry and shock conditions of copper samples.

| **Cu Shock Conditions** | | | | | | |
|---|---|---|---|---|---|---|
| **Shot #** | **Geometry** | | | **Thickness** | **Laser Energy** | **Pressure** |
| | | **Wavelength** | **Amplitude** | | | |
| | | *(um)* | *(um)* | *(um)* | *(J)* | *(GPa)* |
| 25259 | Flat | - | - | 92.5 | 13 | 9.00 |
| 25481 | Flat | - | - | 82.5 | 16 | 10.5 |
| 25269 | Flat | - | - | 94.5 | 36 | 17.90 |
| 25287 | Ripple | 150 | 6 | 96.5 | 27 | 15.47 |
| 25288 | Ripple | 150 | 6 | 113.5 | 19 | 12.18 |
| 25289 | Ripple | 150 | 6 | 113.0 | 20 | 12.65 |
| 25290 | Ripple | 150 | 6 | 108.0 | 19 | 12.18 |

Figures 5.5, 5.6, and 5.7show the comparison between velocity histories using reference PTW [41], calibrated parameters and experimentally obtained velocity history from VISAR for flat samples. The $R^2$ values for the reference PTW parameters [41] and calibrated PTW parameters are shown as well.

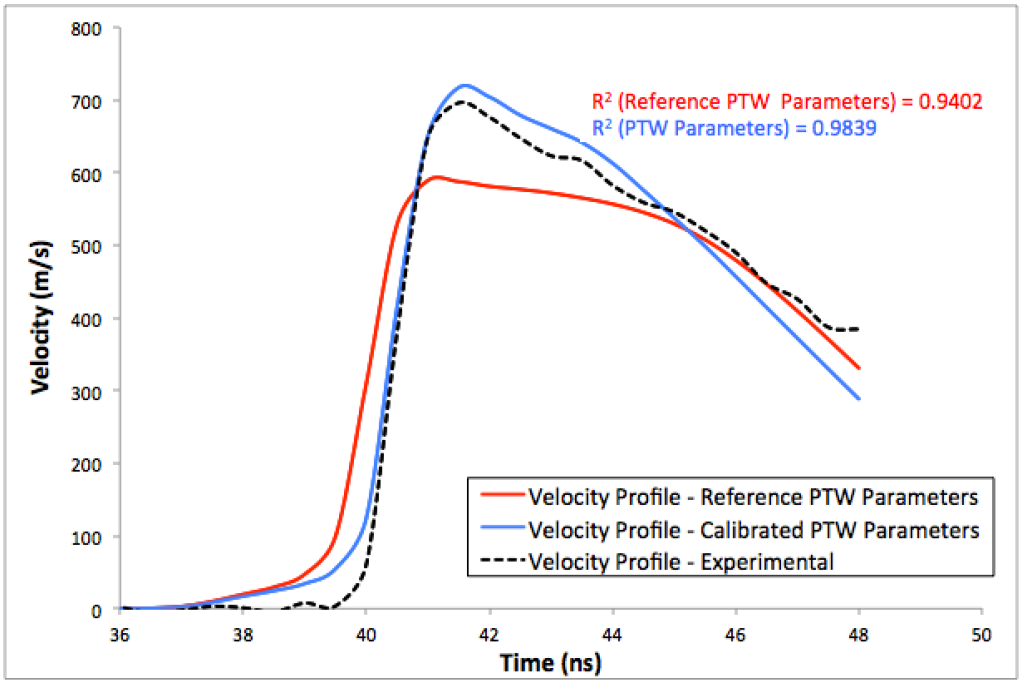


Figure 5.5. Velocity profile using reference PTW parameters and calibrated PTW parameters. Comparison of simulation results with experimental data for shot # 25269.

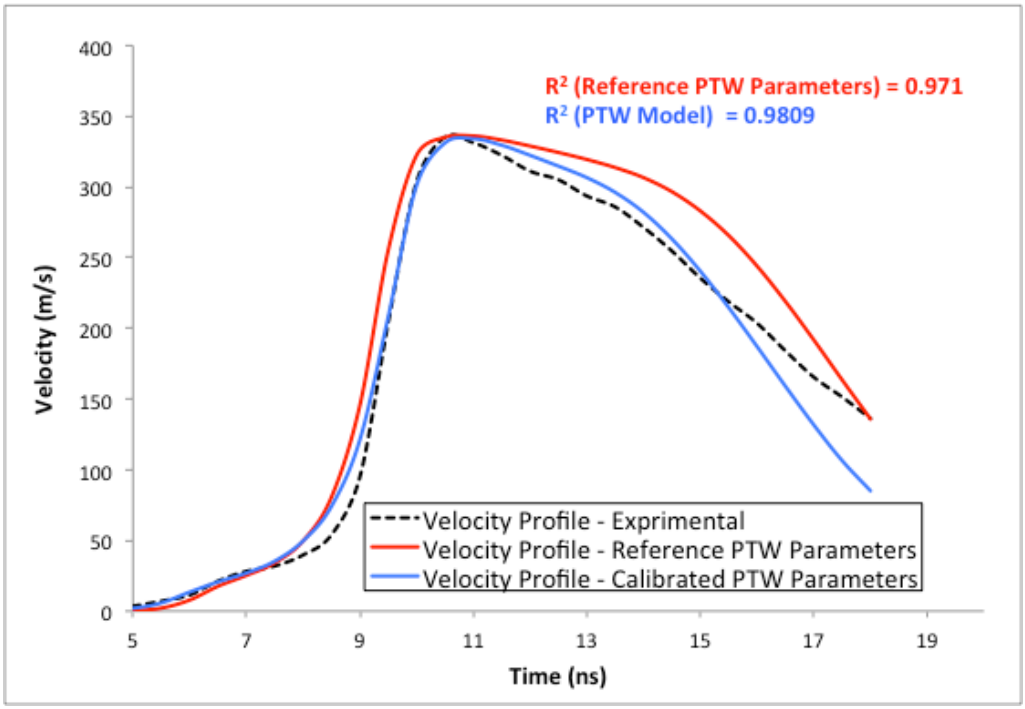


Figure 5.6. Velocity profile using reference PTW parameters and calibrated PTW parameters. Comparison of simulation results with experimental data for shot # 25259.

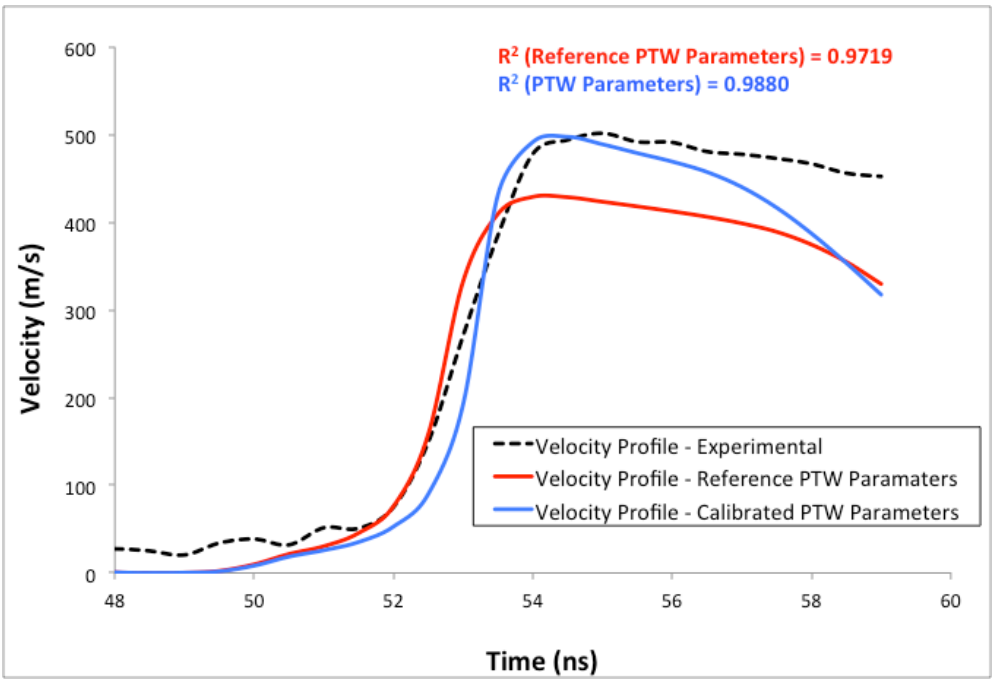


Figure 5.7. Velocity profile using reference PTW parameters and calibrated PTW parameters. Comparison of simulation results with experimental data for shot # 25481.

From figures 5.5, 5.6, and 5.7, it can be seen that the calibrated PTW parameters have a better $R^2$ value, which translates to a better fit with experimental data. The set of PTW parameters that corresponds to $R^2$ values of 0.9839 and 0.9809 (shown in square brackets) along with the reference PTW [41] parameters are shown in table 5.2 below. In table 5.2, the pressure derivative of $G_0$, $(g_p)$ is changed. This changes is not for the calibration. It is an assumption to ease the complexity of the algorithm and computation time. Zuo [96] uses a hypoelastic model without pressure dependent shear modulus and for the pressures ranging from 9-18 GPa, it is a reasonable approximation and it eases the complexity of algorithm. Also, additional simulations done without the approximation of pressure dependent shear modulus did not show significant change in the result.

Table 5.2: Initial PTW model parameters obtained from the literature used for copper [41] and parameters that were modified to give a more accurate match to experimental data are reproduced in square brackets.

| PTW Parameters | |
|---|---|
| **Parameter Description** | **Values** |
| Temperature Constant, $\kappa$ (-) | 1.1e-1 |
| Strain Rate Parameter, $\gamma$ (-) | 1.0e-5 |
| Strain Hardening Parameter, $\theta$ (-) | 2.5e-2 |
| Strain Hardening Parameter, p (-) | 2.0 [1.0e-3] |
| Saturation Stress Factor, $s_0$ (-) | 8.50e-3 |
| Saturation Stress Factor, $s_{inf}$ (-) | 5.50e-4 |
| Yield Stress Factor, $y_0$ (-) | 1.0e-4 [1.0e-3] |
| Yield Stress Factor, $y_{inf}$ (-) | 1.0e-4 [1.0e-5] |
| Medium Strain Rate Constant, $y_1$ (-) | 9.4e-2 |
| Medium Strain Rate Exponent, $y_2$ (-) | 5.75e-1 [2.50e-1] |
| Exponent in Drag, $\beta$ (-) | 2.5e-1 |
| Melt Temperature, $T_m$ (K) | 1.36e3 |
| Reference Shear Modulus, $G_0$ (Pa) | 5.18e10 |
| Pressure Derivative of $G_0$, gp (-) | 8.0 [8.0e-1] |
| $G_0$ Temperature Parameter, $\alpha$ (-) | 2.3e-1 |
| Poisson's Ratio, $\nu$ (-) | 2.9e-1 |

Table 5.3: Equation of state parameters used for the simulation of constitutive model [2].

| EOS Parameters | |
|---|---|
| **Parameter Description** | **Values** |
| Reference Temp., $T_0$ (K) | 3.0e2 |
| Reference Density, $\rho_0$ (kg/m3) | 8.960e3 |
| Specific Heat, $C_p$ (J/kg-K) | 3.86e2 |
| Mie Gruneisen Constant, $\gamma$ (-) | 1.82 |
| Reference Bulk Modulus, $K_0$ (Pa) | 1.4e11 |
| Press. Derivative of Bulk Modulus, $N_0$ (-) | 4.0 |
| Reference Energy, $E_0$ (J/kg) | 0.0 |
| Reference Entropy, $S_0$ (J/kg-K) | 0.0 |

Material parameters from Tables 5.2 (PTW parameters) and 5.3 (Equation of State parameters) were used for the finite element simulations; the simulated velocity

histories of flat samples were compared with the experimental data. Figure 5.8 was obtained by using the material parameters from tables 5.2 and 5.3 in the MATLAB code developed. One can clearly see that the calibrated model has higher strength than the literature parameters [41]. This increase in strength is mostly in thermal and transition regime.

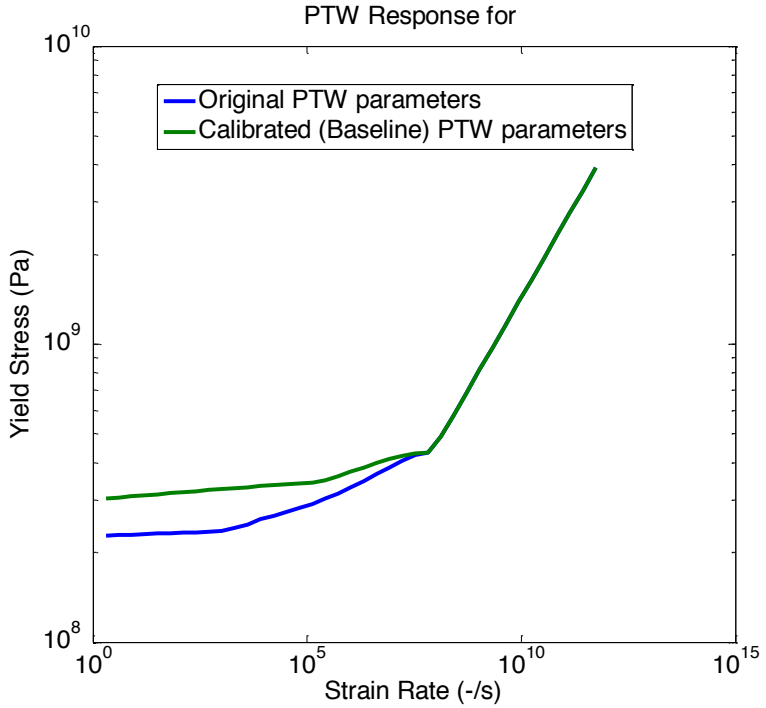


Figure 5.8. Comparison of original (literature [41]) PTW parameters with calibrated PTW parameters.

Figure 5.9 depicts the comparison of experimental velocity profiles obtained from VISAR with numerical simulated velocity history of flat samples using the PTW modified parameters, EOS parameters and pressure pulse. Figure 5.9 (a) shows the deviation of simulation result from experimental at around 15 ns and figure 5.9 (b) shows the same deviation at around 47 ns. The deviation is due to the presence of reflected tensile wave once the shock front reaches the free surface resulting in the development of

tensile stresses that lead to void nucleation and damage [5,57]. The constitutive framework used here does not incorporate these phenomena and, therefore, agreement between the experimental VISAR data and simulation results was sought only within the period of time for which the shock was supported. The $R^2$ calculation was performed only for this time period. Figure 5.9 (c) shows a similar trend as figures 5.9 (a) and (b) except the experimental velocity history has a slow release, and a deviation from simulation larger than for the other cases. The slow release is likely to be a result of an anomaly in the laser pulse, which occurred occasionally during the experiments.

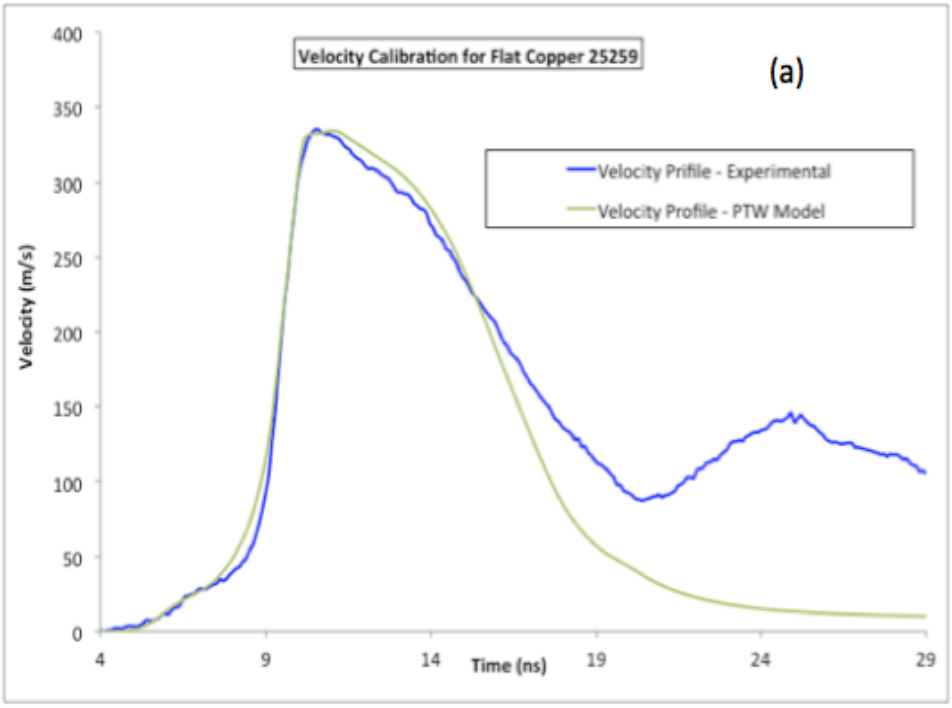

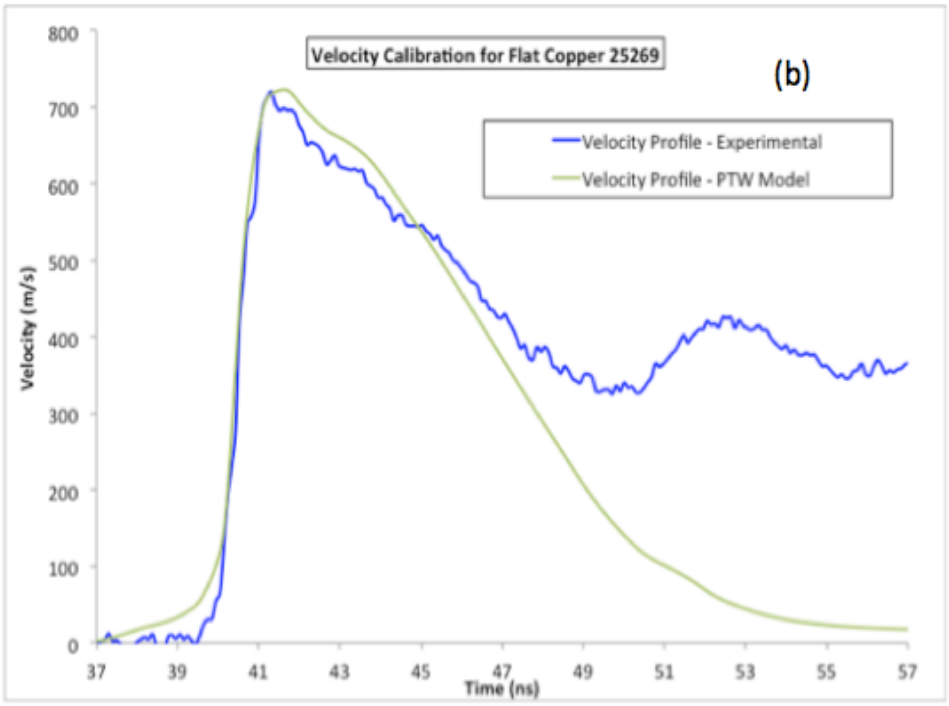


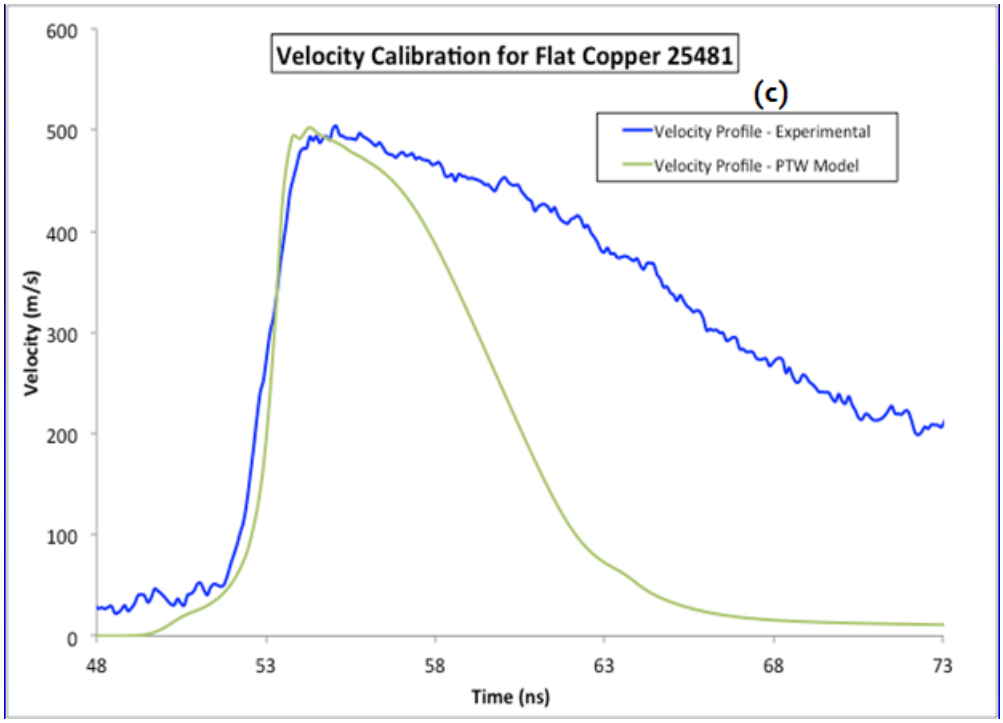


Figure 5.9. Comparison of experimentally obtained VISAR profiles and simulated velocity history profiles of flat copper samples for (a) shot # 25259, (b) shot # 25269 and (c) shot # 25481.

## 5.2. Validation of the Calibrated PTW Model

The calibrated set of PTW material constants was used to validate the constitutive model by performing finite element simulations of rippled (perturbed) copper samples and then doing quantitative comparisons between experimental data obtained from the TIDI analysis and the surface displacement obtained from the simulation. Furthermore, the difference in time of arrival obtained from VISAR data for the forward and backward regions of the perturbed shock front as it reached the free surface was compared to simulation results. Table 5.4 provides the experimental and simulated time differences and they are in good agreement with a maximum difference of 8%.

Table 5.4: Experimental and simulated time difference for the forward and backward regions of the shock front to reach free surface.

| **Experimental and Simulated Δt** | | |
|---|---|---|
| **Shot #** | **Experimental Δt** | **Simulation Δt** |
| | **(ns)** | **(ns)** |
| **25287** | 2.1+/-0.05 | 2.3 |
| **25288** | 3.3+/-0.06 | 3.2 |
| **25289** | 2.8+/-0.045 | 2.7 |

Free surface evolution measured from TIDI data was also compared with the free surface evolution obtained from the simulation. Figures 5.10 and 5.11 show the simulation results for free surface evolution. From figures 5.10 and 5.11, we can see the presence of second harmonic in the free surface displacement plot. The presence of second harmonics will be discussed in the next chapter.

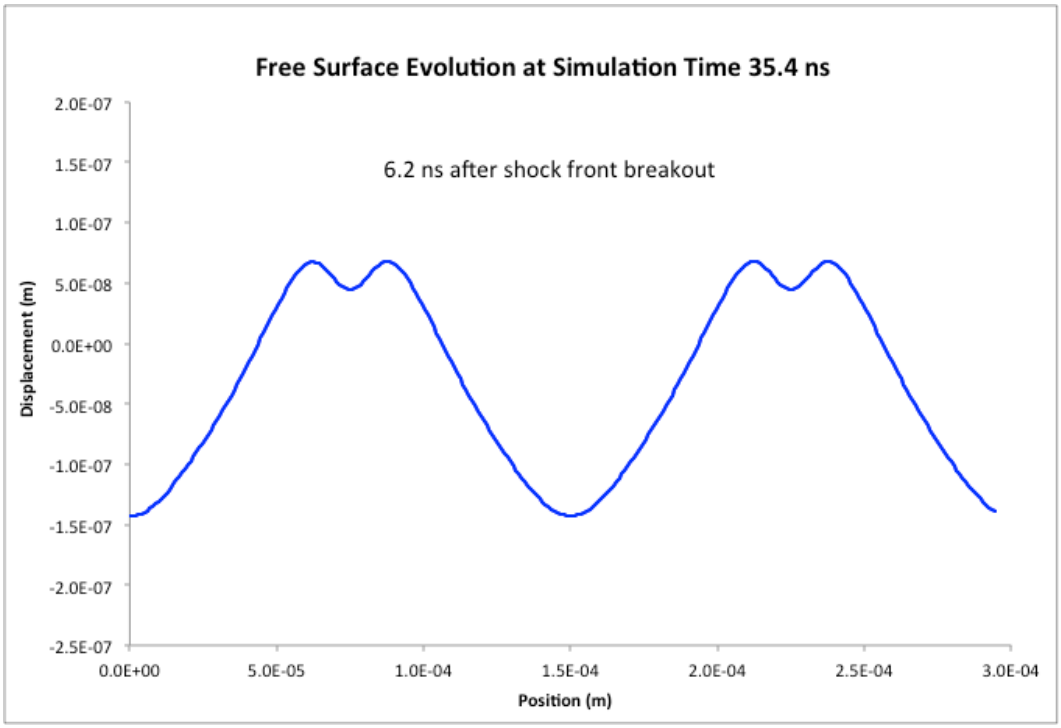


Figure 5.10. Copper (s25288, 19J) free surface profile at simulation time 35.4 ns.

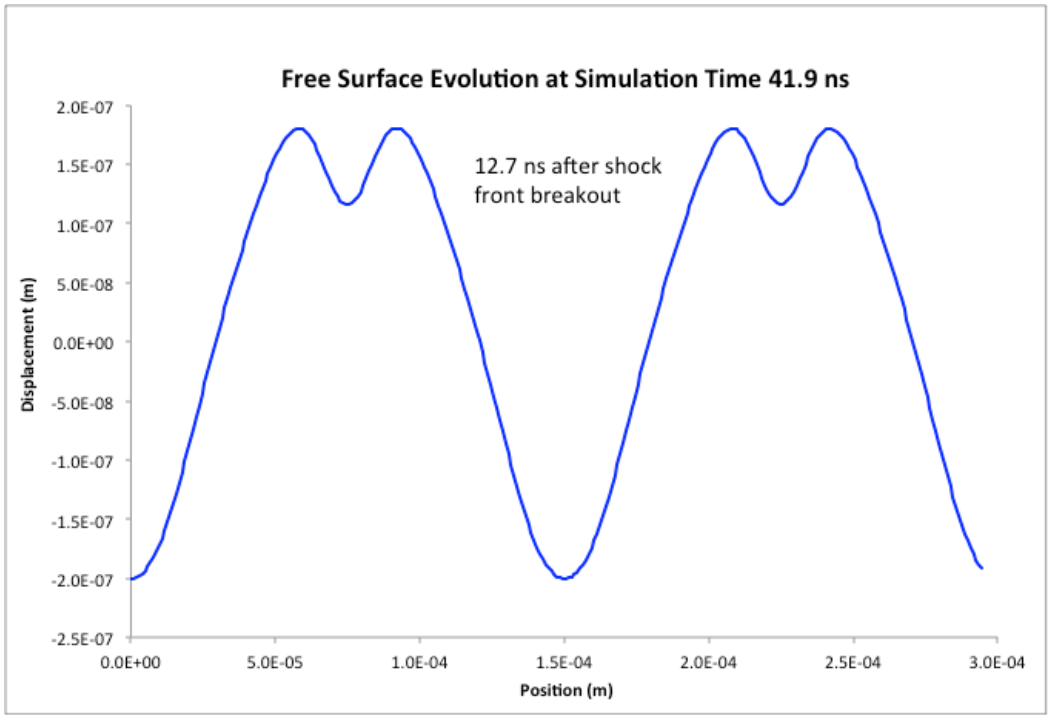


Figure 5.11. Copper (s25288, 19J) free surface profile at simulation time 41.9 ns.

Table 5.5 was created using data from figures 5.10 and 5.11 as well as the TIDI data and it shows the comparison between the experimental and simulated amplitudes (peak and base distance of a free surface profile plot) of the resulting perturbation. Simulation results matched well with the experimental data. At simulation time 35.4 ns, which correspond to 6.2 ns after the shock front breakout, free surface displacements from experiment and simulation agree within the error margin. However, there is a 20% difference between the simulated and experimental peak to base distance (amplitude) of the free surface displacement plot for simulation time 41.9 ns (12.7 ns after shock breakout). The tension (release) wave resulting in spallation possibly contributes to this difference in results, as the model used does not account for damage.

Table 5.5: Copper (s25288, 19J) experimental and simulation results. First column is experimental time measured from shock breakout at the free surface. Amplitude refers to peak to base distance of the free surface displacement plot.

| **Cu Experiment and Simulation Results** | | | |
|---|---|---|---|
| **Time** | **Simulation Time** | **Experimental Amplitude** | **Simulation Amplitude** |
| (ns) | (ns) | (microns) | (microns) |
| 0 | 29.2 | 0 | 0 |
| 6.2 | 35.4 | 0.20+/-0.05 | 0.18 |
| 12.7 | 41.9 | 0.50+/-0.05 | 0.39 |

Once the validation is completed, all ripple samples are used to understand the effect of strength, which is discussed in the next chapter.

# 6. RESULTS AND DISCUSSION

Given that one of the primary goals of this work is to understand the effect of material strength on the evolution of hydrodynamic instabilities through simulations of free surface evolution after a perturbation has been "fed-through" there, simulation results for different strength responses, changed via modifications in appropriate PTW parameters, were compared. To obtain different material strengths, PTW material parameters were adjusted based on figure 5.2, which was discussed in chapter 5. Flow stress was evaluated from a point integrator code developed in MATLAB. Table 6.1 provides the parameters changed for high and low strength values and figure 6.1 shows flow stress versus strain rate resulting from using parameters in table 6.1.

Table 6.1: PTW model parameters changed for increased and decreased strength.

| **PTW Parameters** | | | |
|---|---|---|---|
| **Parameter Description** | **Baseline Strength** | **Increased (High) Strength** | **Decreased (Low) Strength** |
| Temperature Constant, $\kappa$ (-) | 1.10E-01 | 2.20E-01 | 5.50E-02 |
| Saturation Stress Factor, $s_0$ (-) | 8.50E-03 | 1.70E-02 | 4.25E-03 |
| Saturation Stress Factor, $s_{inf}$ (-) | 5.50E-04 | 1.10E-03 | 2.75E-04 |
| Medium Strain Rate Constant, $y_1$ (-) | 9.40E-02 | 1.00E-01 | 8.00E-02 |
| Medium Strain Rate Exponent, $y_2$ (-) | 2.50E-01 | 3.50E-01 | 1.50E-01 |
| Exponent in Drag, $\beta$ (-) | 2.50E-01 | 3.50E-01 | 1.50E-01 |

The resulting sets of parameters were used for finite element simulations of rippled copper samples, keeping driving force, geometry and other material properties, e.g., EOS, constant. Simulation results obtained from new PTW parameters for high and low strength were then compared with results using the baseline strength (calibrated PTW model parameters).

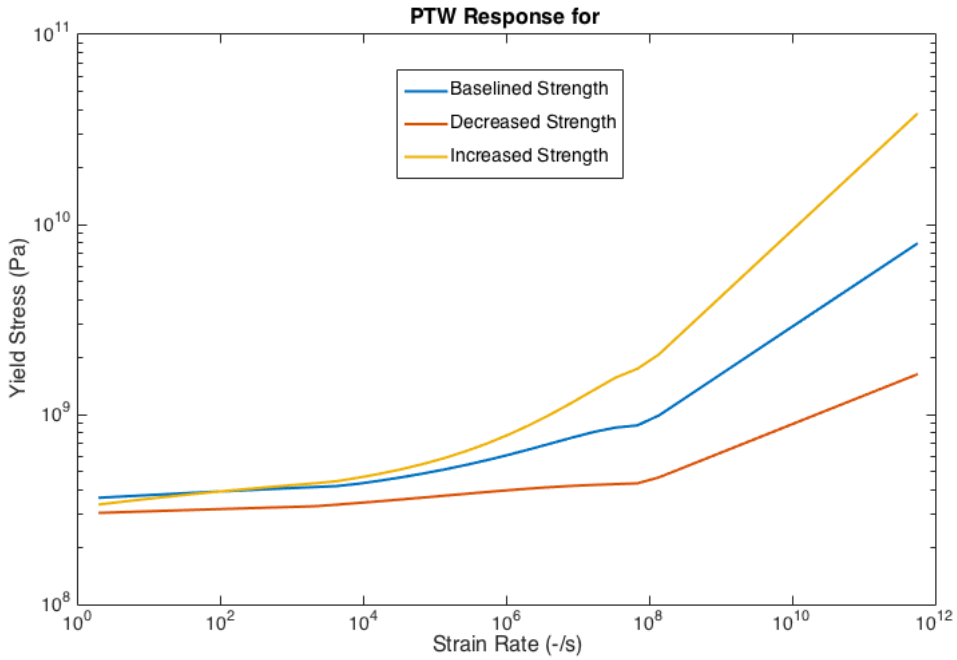


Figure 6.1. Effect of changing PTW parameters on flow stress predicted as a function of strain rate. The baseline curve obtained after calibration process is shown for comparison.

The effect of different strengths can be seen in the von Mises and pressure plots provided in figure 6.2. As shown in figure 6.2 (a), the von Mises stress is maximum for the increased strength, as it should be, since it is a measure of the deviatoric (shear stress) that material can sustain. Hence, it also decreases with decreasing strength as can be seen in figure 6.2 (b) and (c) respectively. Conversely, pressure displays the opposite behavior, as shown in figure 6.2 (d), (e) and (f). This is also expected, since for a given driving force, an increase in strength should lead to a decrease in pressure under the uniaxial strain conditions that are typical of shock waves. Since the ablated surface of the sample is perturbed, the shock front that passes from the base of the sample is ahead of the shock front that passes from the peak resulting in a perturbed shock front as can be seen in figure 6.2.

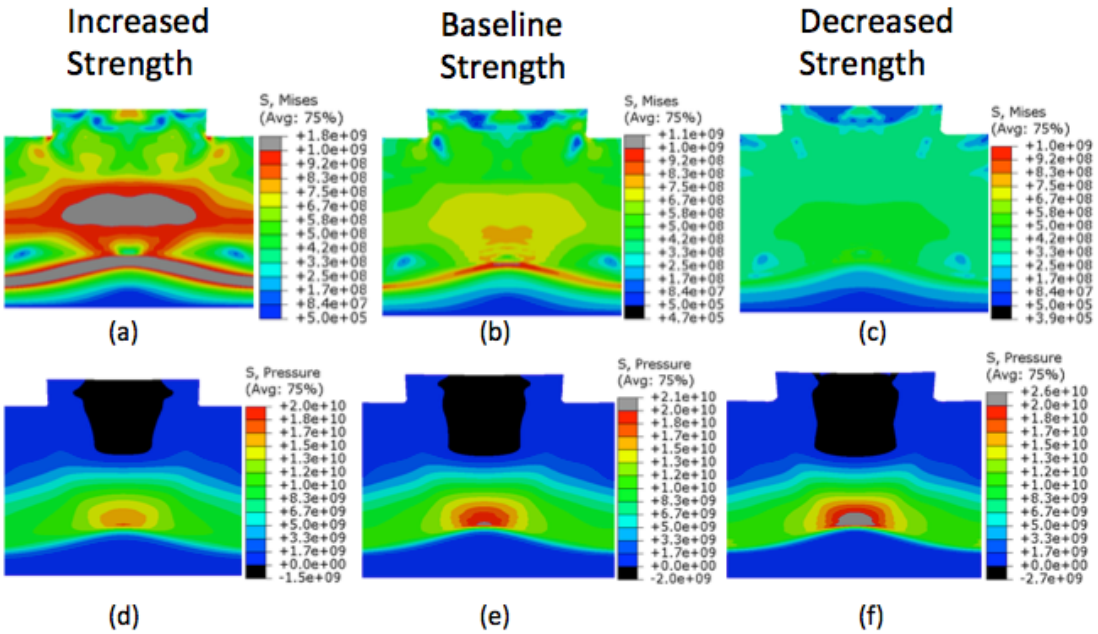


Figure 6.2. Von Mises and pressure contour plots for copper (s25287, 15.47 GPa) at different strengths just before the shock front reaches the free surface. Figures (a), (b) and (c) are the von-Mises stress plots for increased strength, baseline strength and decreased strength, respectively. Figures (d), (e) and (f) are pressure plots for increased strength, baseline strength and decreased strength, respectively. The scales used for each variable are the same for all three strength levels. Shocks propagate from top to bottom.

In most plasticity models, plastic strain rate is directly proportional to the deviatoric stress and von Mises stress is a measure of deviatoric stress; therefore, the plastic strain rate is maximum where von Mises stress is maximum. This is further explored in figure 6.3 where von Mises stress, pressure, and equivalent plastic strain rate are plotted along the thickness of the specimen (from top (center of the peak) to bottom). The maximum pressure is found right behind the shock front, as expected, as the maximum values of von Mises stress and plastic strain rate are also found at that location, where the conditions are the most extreme. The contour plots shown in figure 6.3 indicate clearly that the shock front gets perturbed and as it passes through the thickness of the

sample, and that different conditions are present under the peak and the valley of the initial perturbation. These differences are examined in figure 6.4.

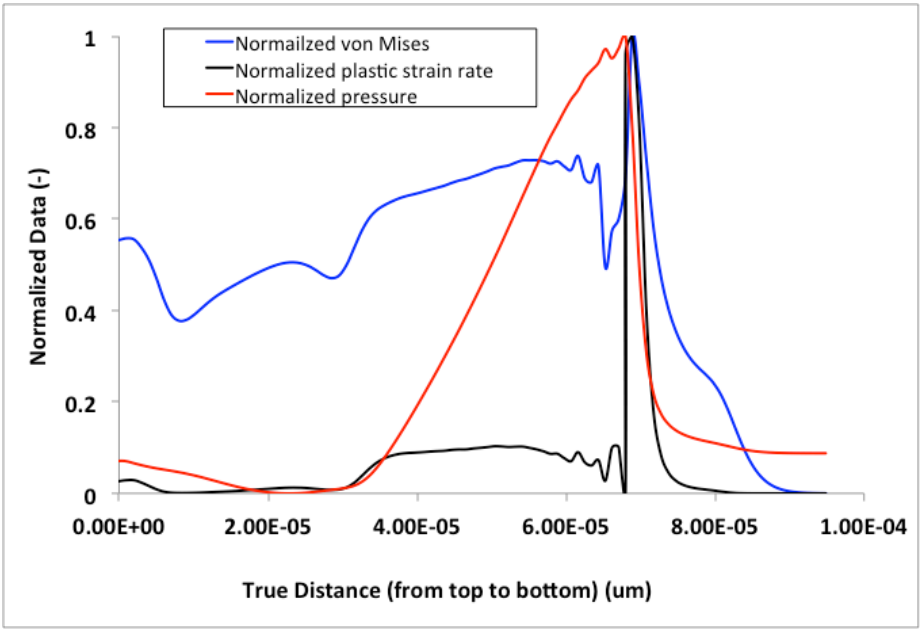


Figure 6.3. Normalized plastic strain rate, von Mises, and pressure versus distance from top to bottom at the center of the model for sample s25287, 15.47 GPa.

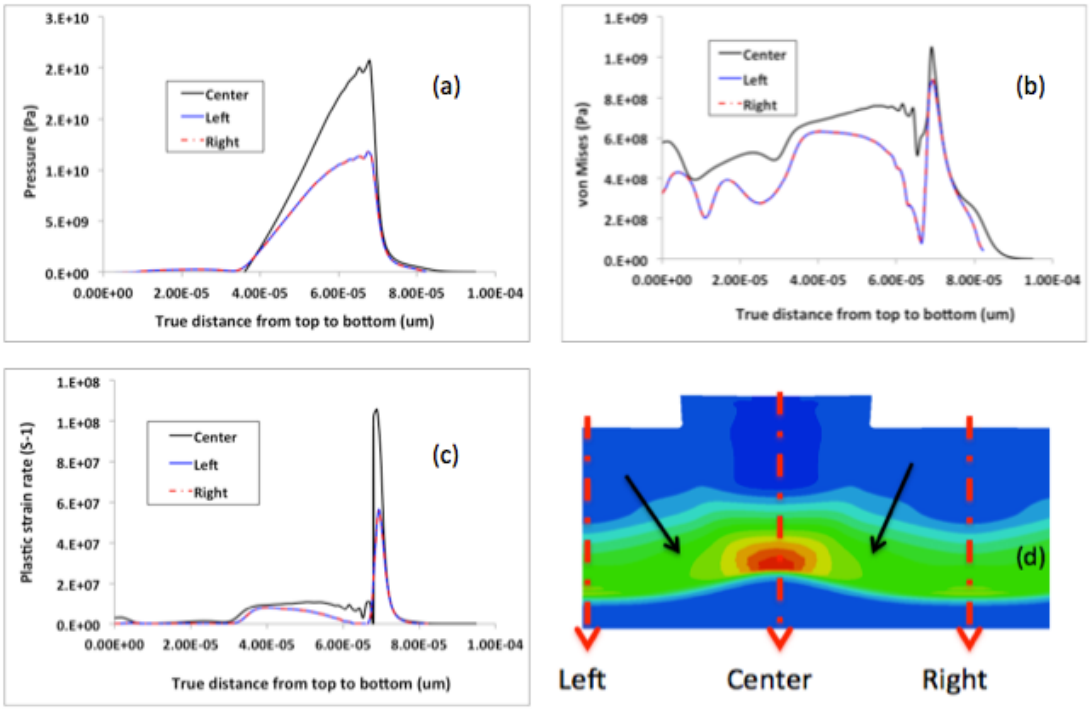


Figure 6.4. Distribution of von-Mises, pressure, and equivalent plastic strain-rate for different paths versus distance from top to bottom at different locations of the model for copper s25287, 15.47 GPa (a) pressure, (b) von Mises stress, (c) plastic strain rate, and (d) model showing three different paths created to extract the results. Black arrows represent obliquity of the shock waves.

In figure 6.4 (d), the black arrows indicate the obliquity of the shock waves present at the left (shock front under the initial surface perturbation valley) and right (shock front under the initial surface perturbation valley). This results in the concentration of stress (pressure) at the center (shock front under the initial surface perturbation peak). This is also evident in figures 6.4 (a), (b) and (c) where pressure, von Mises stress and equivalent plastic strain rate are higher for the center path than for the right and left paths. Increase in pressure (stress) at the center (under the peak of the surface perturbation) leads to an increase in shock wave speed at the center as compared to the shock front located under the valleys of the original perturbation, which is the implies that a flat shock front is stable against perturbations like the ones induced here,

since the faster shock front that lags behind will eventually catch up to the one ahead, and will eventually become flat again. This is evident from the evolution of pressure profiles and is discussed in more detail later.

The effect of strength can also be seen very clearly in the evolution of the free surface profile, where increasing the strength decreases the perturbation amplitude due to a slow down of the growth rate of the hydrodynamic instability, as expected given results presented in [9-18,28]. Given that the laser pulse was very short, it is unlikely that the surface profiles measured experimentally had reached steady state and the presence of damage must have also altered it. Therefore, to capture the final surface profile from the simulation without damage, a simulation was performed to study the "steady state" of the perturbation by running a model for a long time. At time $t = 216.8$ ns after shock breakout, the surface profile was captured as the surface profile did not change significantly after this time. Figure 6.5 shows the steady state free surface profile for copper sample s25287 at a simulation time $t = 240$ ns.

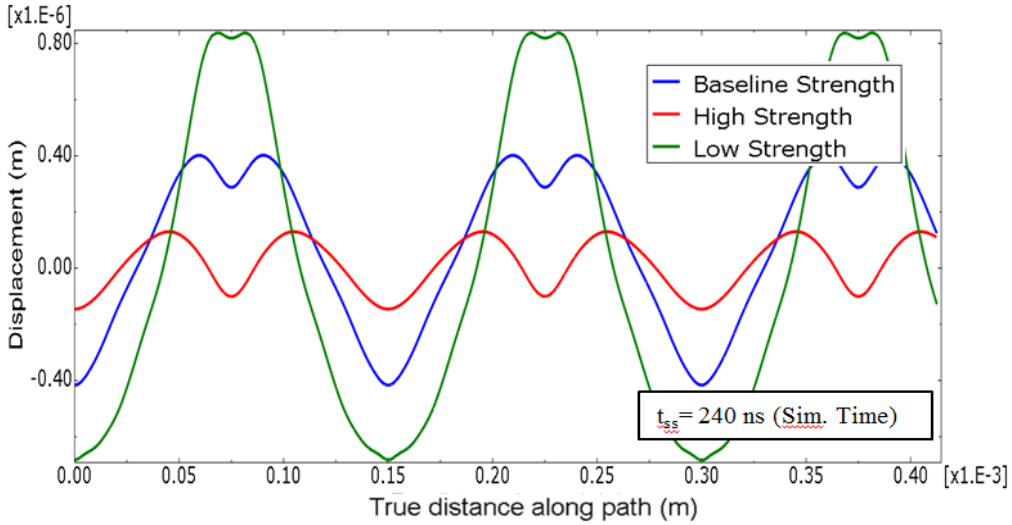


Steady State Free Surface

Figure 6.5. Free surface profile at “Steady State” for copper (s25287, 15.47 GPa) using different strength levels.

Increased (high) strength has the smallest perturbation amplitude and decreased (low) strength has the largest perturbation amplitude, which shows the effect of strength in hydrodynamic instability as expected from the research work done by Piriz and coworkers [9,10,13,14]. They used the RM instability as a tool to evaluate material strength of solids by providing a simple scaling law between the strength and perturbation amplitude where the maximum amplitude measured at a relatively long time was inversely proportional to the yield strength of a material. Similar results are seen in figure 6.5, where one can say that strength has a reverse effect on perturbation amplitude [13,14]. Results for the baseline strength lie between results for increased and decreased strengths, as expected. The presence of second harmonics can be noted in figure 6.5. As seen from the surface profiles of three different strengths, second harmonics were amplified by high strength and were decreased by low strength, which strongly suggests that strength has an effect on evolution of second harmonics. The presence of second harmonics will be explored in more details in another section.

Figures 6.6 and 6.7 also provide information on the dynamics of the evolution of free surface profile for copper samples, at times 35.4 ns and 41.9 ns with different strengths respectively. The simulation time of 35.4 ns corresponds to 6.2 ns and a time of 41.9 ns corresponds to 12.7 ns time after shock breakout at the free surface, respectively. The trends seen in figures 6.6 and 6.7 are the same as those seen in figure 6.5.

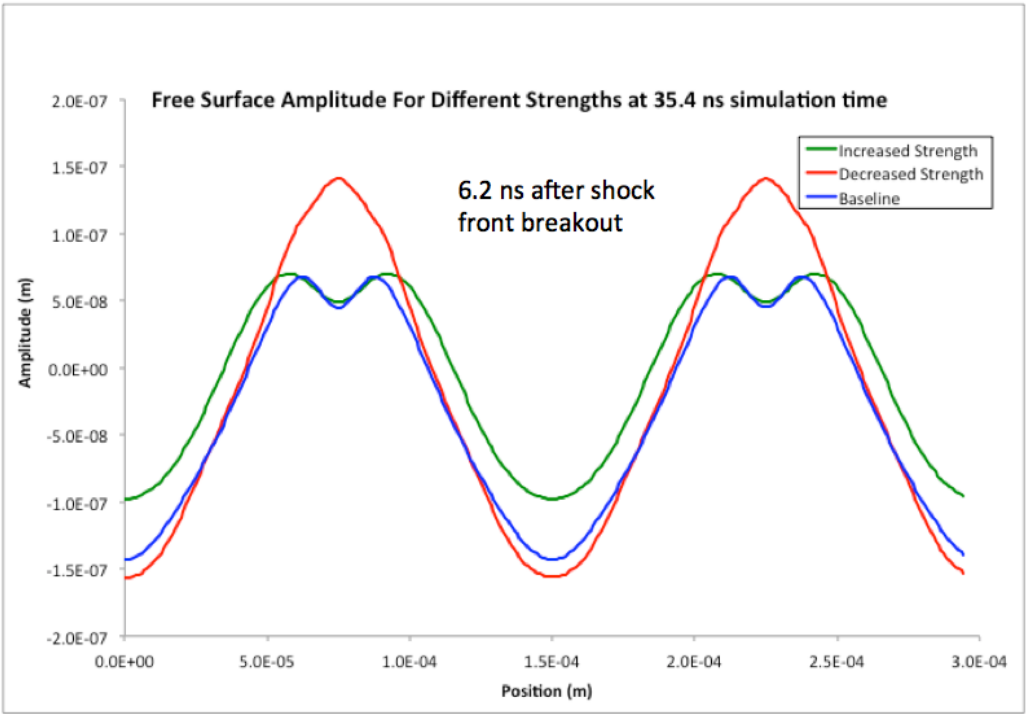


Figure 6.6. Free surface profile of copper (s25288, 12.18 GPa) at 6.2 ns after shock breakout for different strengths.

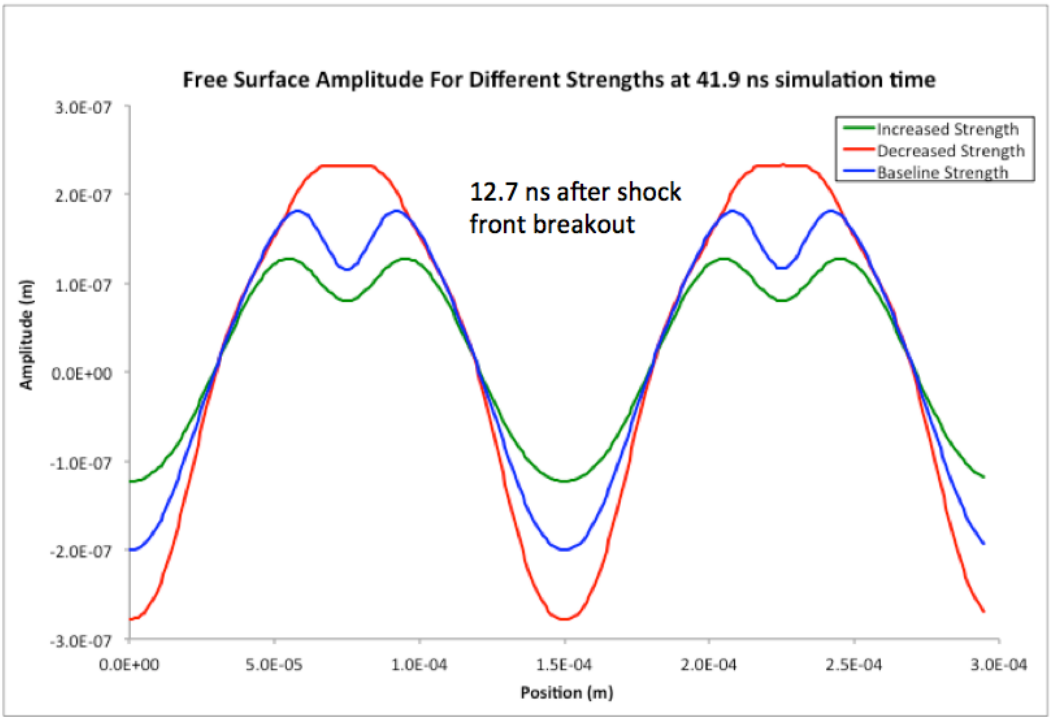


Figure 6.7. Free surface profile of copper (s25288, 12.18 GPa) at 12.7 ns after shock breakout for different strengths.

Table 6.2 shows the numerical values of the amplitude of the free surface profile for simulation results, which directly correspond to figures 6.6 and 6.7, and a direct comparison to the experimental data collected with TIDI. Table 6.2 shows that at time $t = 6.2$ ns after shock breakout, the simulation result falls within the experimental error margin. However, at time $t = 12.7$ ns after the shock breakout, the simulation result shows a 20% difference with the experimental result. Note that at 12.7 ns after shock breakout there has been about enough time for two tensile waves to meet, spall damage to develop and a pullback to appear (see figure 5.8(a)). The compressive release wave due to spall would reload the surface leading to the larger amplitude observed experimentally. Given that the constitutive framework used does not incorporate damage/spall, the simulation result cannot be directly compared with the experimental results at this time and an underestimation of the actual amplitude should be expected..

Table 6.2: Experimental and simulation results for the amplitude of the free surface profile for copper (s25288, 12.18 GPa). Simulation results incorporate 3 different strength levels. First column is experimental time since shock breakout at the free surface.

| **Cu Experimental and Simulation Results** | | | | | |
|---|---|---|---|---|---|
| **Time** | **Simulation Time** | **Experimental Amplitude** | **Simulation Amplitude** | | |
| | | | **Baseline Strength** | **Increased Strength** | **Decreased Strength** |
| (ns) | (ns) | (microns) | (microns) | (microns) | (microns) |
| 0 | 29.2 | 0 | 0 | | 0 |
| 6.2 | 35.4 | 0.20+/-0.05 | 0.21 | 0.16 | 0.29 |
| 12.7 | 41.9 | 0.50+/-0.05 | 0.39 | 0.25 | 0.54 |

Figures 6.6 and 6.7 also show clearly that no second harmonic develops for the decreased strength whereas it is amplified by the increased strength. From figures 6.5,

6.6, and 6.7, we can see that the amplitude of the second harmonic is also affected by strength, with the ratio of the amplitudes of the second to first harmonics increasing with increasing strength.

To understand more of the dynamic evolution of the free surface profile, it is important to evaluate the surface perturbation as a function of time. As we have seen in both experimental and simulation results, the perturbed shock front oscillates in time and space [28] and RM instability will occur following the shock breakout and depending on the time of the shock breakout, the shock front will induce different surface perturbation amplitudes. Figure 6.8 shows the oscillation of free surface in time and space for various simulation times: $t = 15, 20, 25, \text{and } 30$ ns and the simulation was performed with baseline strength. The lack of perturbation amplitude for simulation at time $t = 15\ ns$ indicates that the shock front has not reached the free surface as the shock front reaches the free surface at 17.6 ns; this is evident in figure 6.8. The simulation result for time $t = 20\ ns$ (2.4 ns after shock breakout) shows clear evidence of the shock front reaching the free surface and no presence of second harmonic. However, from time $t = 25$ ns (7.4 ns after shock breakout), the presence of second harmonic can be seen and the free surface perturbation reverses at this time. As explained in figure 6.4, parts of the shock front that arrives later have more pressure than those arrive first. Due to the increase of pressure, these waves travel faster when they arrive at the free surface and end up catching up and overtaking leading to inversion. This is also enhanced when the material remains incompressible in the shocked state, and if its rear surface is initially indented, then the shocked indentation inverts itself, which is consistently observed in explosively- and laser-driven experiments as well as simulations [16,17]. At time $t = 25$ ns (7.4 ns

after shock breakout), shock waves that arrive later overtake shock waves that arrive first after reaching the free surface creating an inversion. At time $t = 30$ ns (12.4 ns after shock breakout) surface perturbation grows higher and shows significant second harmonic as well.

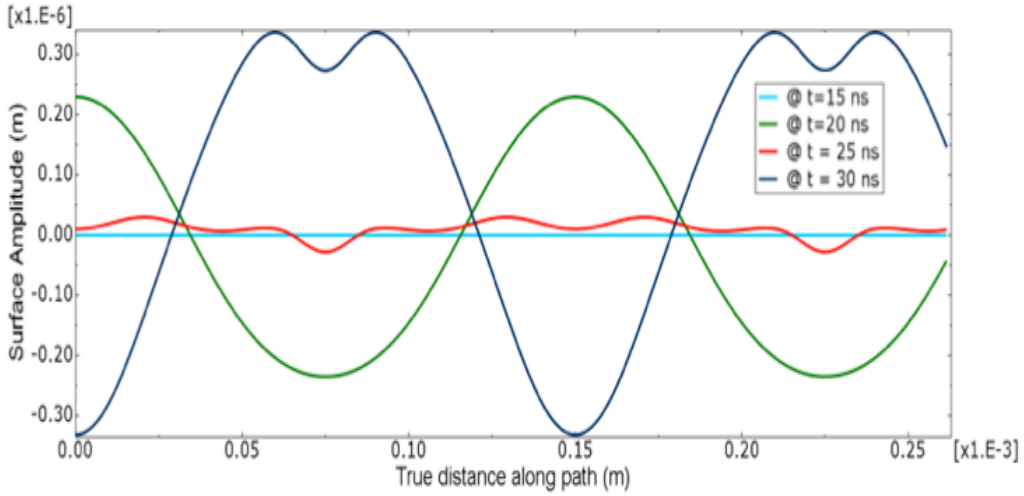


Figure 6.8. Evolution of the free surface perturbation at different times for copper (s25287, 15.47 GPa).

As seen in figures 6.5-6.8 and other experimental results described in chapter 3, the evolution of the free surface perturbation displays behavior in a higher harmonic, i.e., at a spatial frequency that is higher than that of the ripples made in the samples, after a certain time and for certain strength. In order to understand the presence of second harmonics, finite element simulations were performed using a sine wave perturbed sample to analyze if the presence of second harmonics was due to the square wave. A sinusoidal wave has a single Fourier mode, whereas a square wave with sharp boundaries has higher harmonics, i.e., the Fourier transform of a square wave exhibits an "infinite" series of higher harmonics, and a Fourier series encodes the sharp square-wave type features as an infinite sum of smooth sinusoids with different frequencies, all of them integer multiples of the fundamental frequency or first harmonic. All the dimensions such

as wavelength and amplitude for the perturbation, and thickness and width for the sample were kept constant and were referenced to s25290, 12.18 GPa (19 J) for both sine and square wave. To evaluate the difference in surface profile between the square and sine wave for the perturbed sample, boundary conditions and loading conditions were also held constant as baseline strength was used for all cases.

Figures 6.9, 6.10, and 6.11 show the surface profile results from simulations on the perturbed samples. Figures 6.9 and 6.10 are plots of the free surface profile for sine and square wave perturbations at 20 ns (1 ns before shock breakout) and 25 ns (4 ns after shock breakout) simulation time, respectively, these simulation results do not show the presence of $2^{nd}$ harmonics. Figure 6.11, however, being the latter free surface profile of sine and square wave at 30 ns (9 ns after shock breakout) shows the presence of $2^{nd}$ harmonics. This suggests that the presence of higher harmonics with time in the free surface profile can be a result of the interaction of shock front waves with the release waves, after the shock front has reached the free surface. Figure 6.9 is at 20 ns, which is just before shock breakout and therefore the result is in 100 of picometers. Despite the numerical accuracy issues that are likely present, it can be useful to see the free surface profile evolving from here on. Figure 6.10 is a free surface profile at 25 ns (4 ns after shock breakout) and when compared with figure 6.8 at 25 ns (7.4 ns after shock breakout), we can see figure 6.8 shows an inversion while figure 6.9 is continuously growing. However, inversion takes place in figure 6.11 at time 30 ns (9 ns after shock breakout). Figure 6.8 used higher pressure of 15.47 GPa whereas figures 6.9, 6.10, and 6.11 are representatives of s25290 perturbed sample and use 12.18 GPa. Also, figure 6.8 representative of s25287 and s25287 and s25290 compose different thickness

(96.5 and 108 $\mu m$ respectively). s25287, due to higher applied pressure and shorter sample thickness results in earlier time for shock breakout and the inversion.

From the comparison between figures 6.8 and 6.11, we can say that free surface profiles indicate inversion at certain time after shock front breakout and the higher harmonics can be seen during an inversion. Additionally the difference in amplitudes in figure 6.8 and figures 6.9, 6.10, and 6.11 also indicate that the higher pressures result in higher amplitudes. The comparison between surface profiles of different pressures and thickness of the sample will be discussed later.

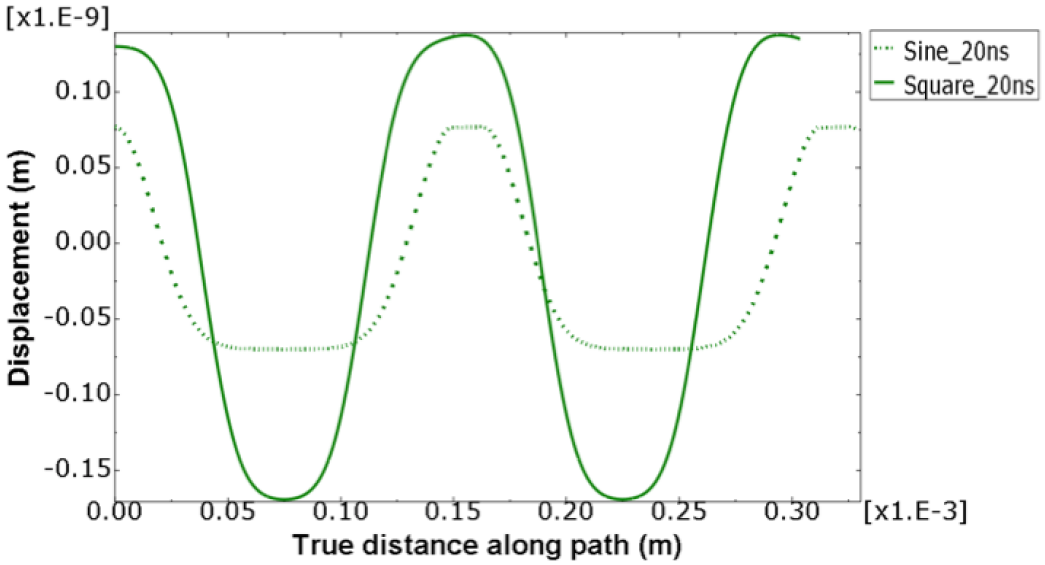


Figure 6.9. Free surface profile for sine and square wave perturbations at 20 ns (just before shock breakout) simulation time.

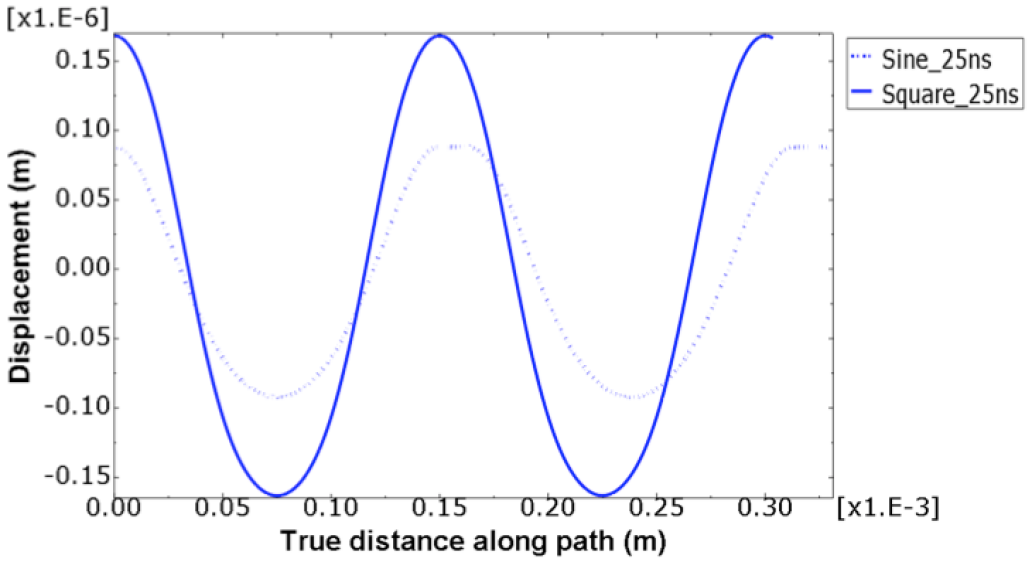


Figure 6.10. Free surface profile for sine and square wave perturbations at 25 ns (4 ns after shock breakout) simulation time.

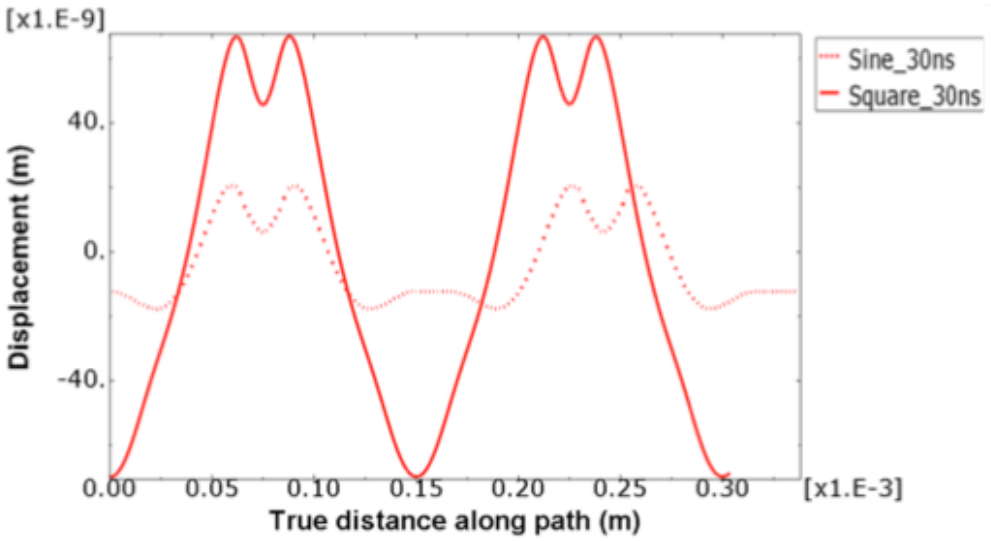


Figure 6.11. Free surface profile for sine and square wave perturbations at 30 ns (9 ns after shock breakout) simulation time.

The study performed using sine and square wave leads us to believe that the presence of second harmonics is not due to the shape of the wave, since both sine and square wave show second harmonics at 30 ns (9 ns after shock breakout) simulation time, but rather that it occurs at a certain time after the shock breakout. This is further studied

from the evolution of the pressure contour plots provided in figure 6.13 and from velocity history for peak (shock front under the peak of the initial perturbation) and base (shock front was under the valley of the initial perturbation) shock front shown in figure 6.12.

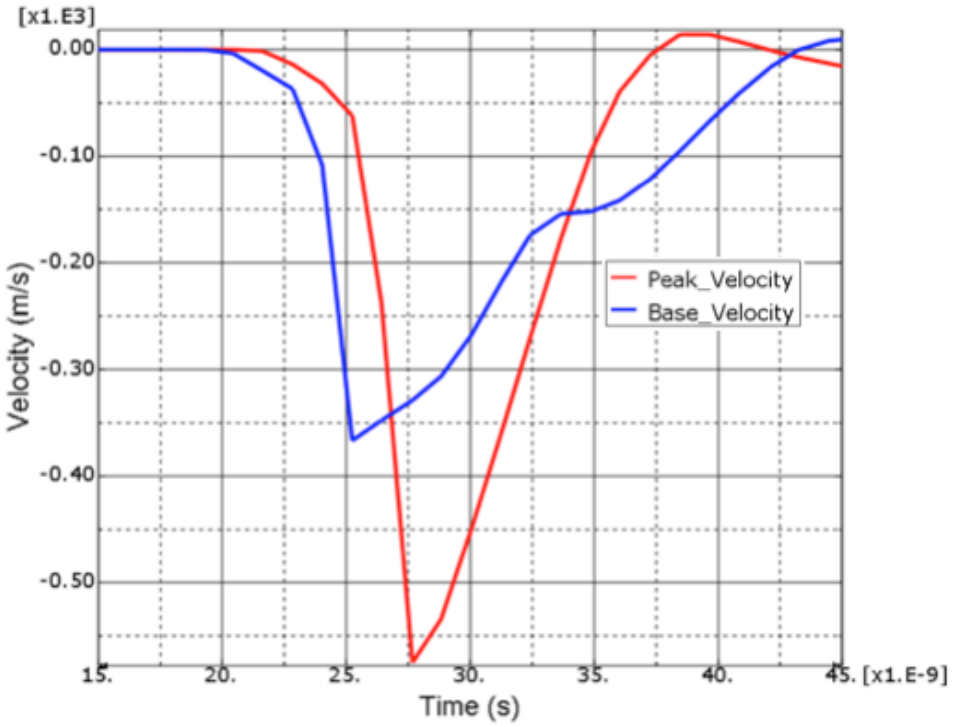


Figure 6.12. Velocity history of a peak and base shock front for copper (s25289, 12.18GPa).

Note as seen in figure 6.12, base shock front (shock front was under the valley of the initial perturbation) breaks out earlier than the peak shock front (shock front under the peak of the initial perturbation) and this shock breakout time was taken for all the simulations as shock front breakout time. Figure 6.12 clearly depicts that the shock wave that arrives later travels faster than the shock wave that arrives earlier when it arrives at the free surface and end up catching up and overtaking. This overtaking of the base velocity (shock front was under the valley of the initial perturbation) by peak velocity

(shock front was under the valley of the initial perturbation) leads to an inversion. Figure 6.12 indicates the interaction of peak shock front and release wave coming from the base shock front after reaching free surface are at simulation time ≈ 27 ns (6 ns after shock breakout). Around the same time, as seen in figure 6.13 (d), (e), and (f), there is an initial development of second harmonics. These harmonics are more prominent in figure 6.13 (g) and (h), which represent the pressure profiles at time 9.05 and 11.9 ns after shock breakout. This suggests that the presence of second harmonics is due to the interaction of shock front and release waves. Note that figures 6.13 (a), (b), (c), and (d) show the development of the shock front, where the peak shock speed is higher than that of the base due to the concentration of stress at the center and reaches the base shock front seen in 6.13 (d).

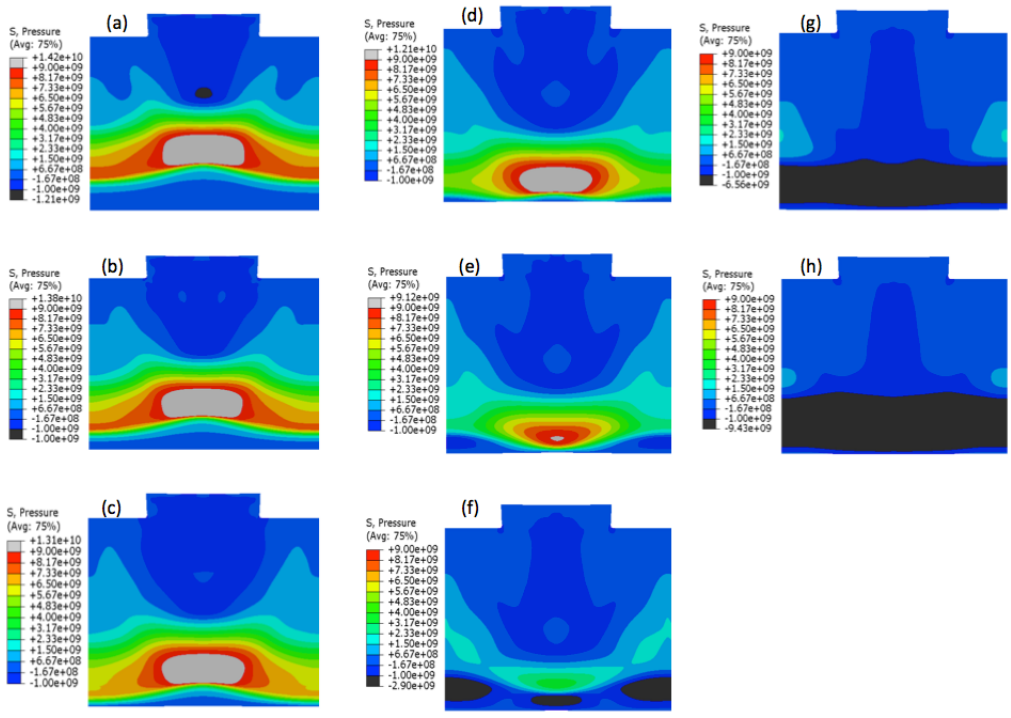


Figure 6.13. Evolution of pressure profiles for copper (s25289, 12.18 GPa) at different times. (a) 0.19 ns before shock breakout, (b) 1.43 ns, (c) 3.03 ns, (d) 4.61 ns, (e) 6.22 ns, (f) 7.82 ns, (g) 9.05 ns, and (h) 11.9 ns after shock breakout respectively.

Note from figures 6.9, 6.10 and 6.11 that the amplitudes resulting from the sine wave perturbation are smaller compared to the square wave, at all times. As explained earlier, Fourier transform of a square wave exhibits an "infinite" series of harmonics and a Fourier series encodes a square wave as the sum of smooth sinusoid. Note also from figures 6.9, 6.10, and 6.11 that the square wave has higher perturbation amplitudes as compared to the sine wave. This is also observed by Loomis et. al. [28], where he performed 2D Fourier transform and radial average in the Fourier domain to extract TIDI images of targets with different levels of roughness and grain sizes. They observed significant increase in the power spectrum density of each mode where the each mode will grow according to its own scaling law for large grains, where perturbations cannot be smoothed easily, and appreciably less increase for samples with smaller grains.

From figures 6.8 - 6.11, we saw that the applied pressure (laser energy) has an effect on the perturbation growth. Since all the ripples simulated have same initial wavelength and amplitude and comparable thickness, a comparison of applied pressure and its effect on the perturbation growth on the free surface of the sample can be achieved. All the simulations performed to understand the effect of applied pressure were done using baseline strength and were captured at 10 and 14 ns after the shock breakout.

Figure 6.14 indicates the effect of applied pressure for two-rippled samples s25288 and s25289 and surface profiles were captured at 10 ns after shock breakout. Samples s25288 and s25289 are rippled samples with the thickness $113.5\ and\ 113.0\ \mu m$ and applied pressured of 12.18 and 12.65 GPa respectively. As s25288 and s25289 have comparable thickness, we can see that surface perturbation for s25289 is higher than s25288 indicating perturbation growth is amplified by the applied pressure (laser energy).

This trend is also seen in figure 6.15 where s25287 has a thickness of 96.5 $\mu m$, applied pressure of 15.47 GPa and surface profile was captured at 10 ns after shock breakout. Figure 6.16, however indicates the effect of thickness for two rippled samples s25288 and s25290 and surface profiles were captured at 14 ns after shock breakout. Specimens s25288 and s25290 both have same applied pressure of 12.18 GPa but different thickness of 113.5 and 108.0 $\mu m$ respectively and the result in figure 6.16 indicates the dependence of sample thickness in the growth of perturbation amplitude showing s25290 with smaller thickness has higher perturbation amplitude than s25288.

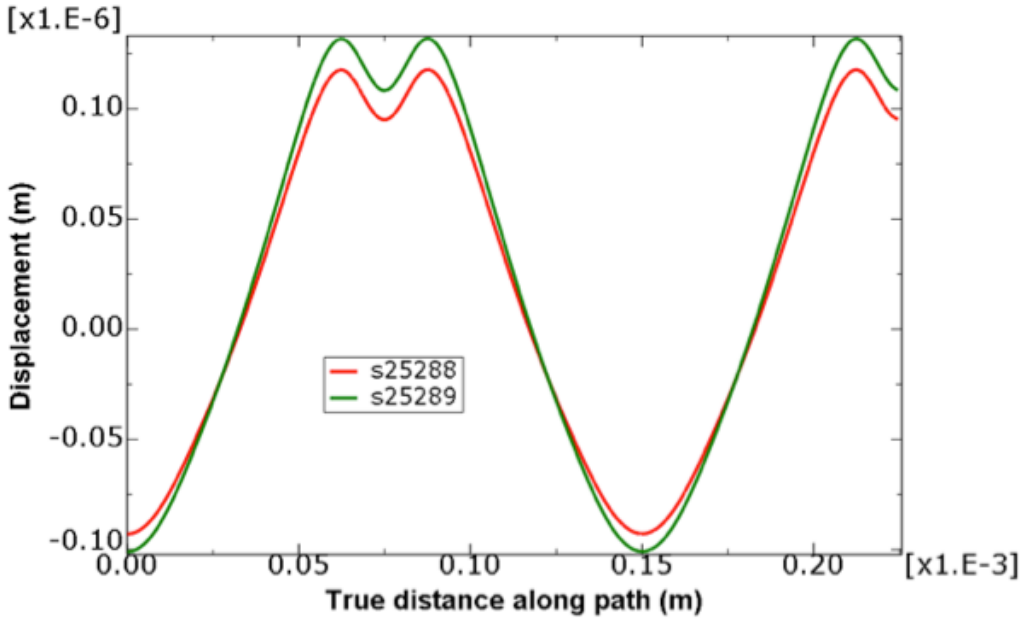


Figure 6.14. Free surface profile for two rippled copper samples at 10 ns after shock breakout (s25288, 12.18 GPa) and (s25289, 12.65 GPa).

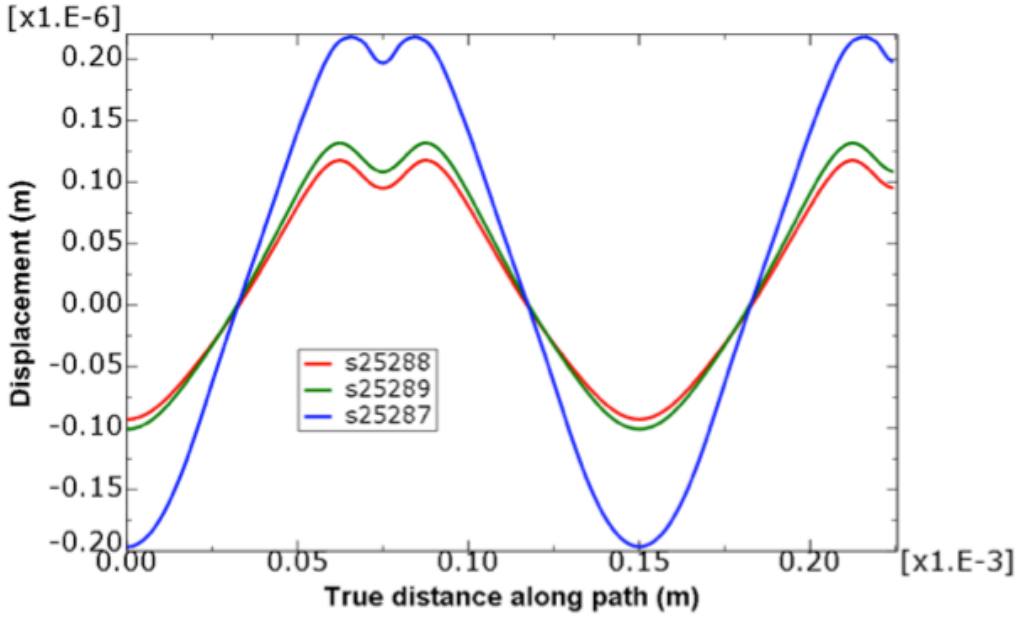


Figure 6.15. Free surface profile for three rippled copper samples at 10 ns after shock breakout (s25287, 15.47 GPa), (s25288, 12.18 GPa), and (s25289, 12.65 GPa).

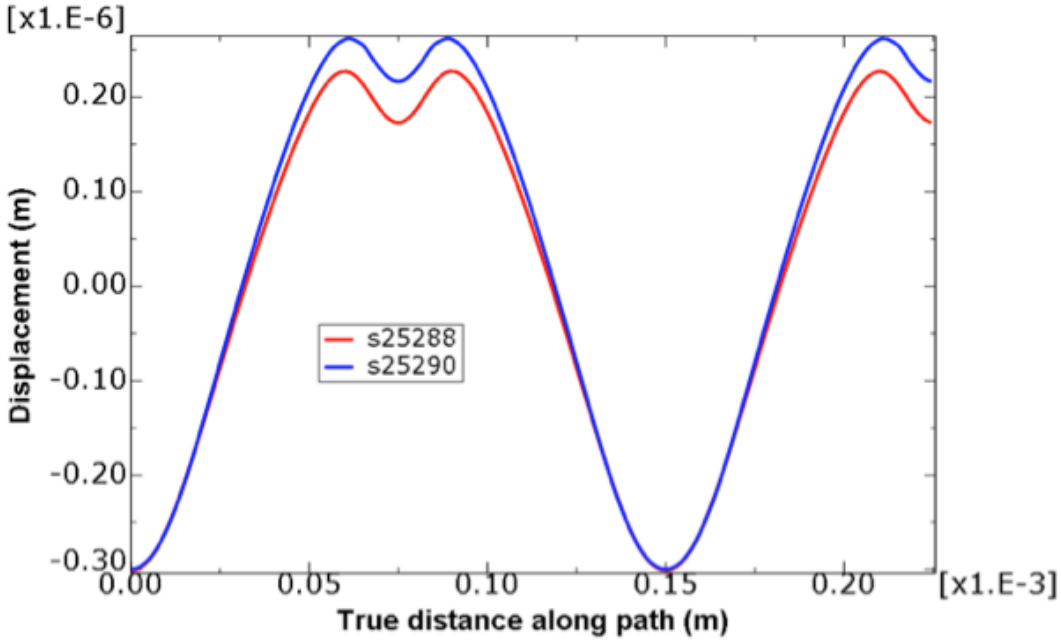


Figure 6.16. Free surface profile for two rippled copper samples at 14 ns after shock breakout (s25288, 12.18 GPa) and (s25290, 12.18 GPa).

Since the ablated surface of the specimen is perturbed (rippled), the shock front also gets perturbed as it can be seen from a wave like curvature in the von Mises stress and pressure plots in figure 6.2. In figure 6.2, the shock front that passes from the base of the perturbed sample is ahead of the shock front that passes from the peak. Therefore, there is a difference in time (delta t) for peak and base shock front to reach free surface also seen in figure 6.12. This can also be seen in the line VISAR images obtained from the experiment.

Experimental time difference for base and peak shock front was measured directly from the line VISAR and was compared to the time differences obtained from finite element simulations. Also, these time differences were then compared with different levels of strength to understand the effect of material strength on the shock front perturbation when it reaches the free surface. The initial time difference for the peak and base shock fronts can be easily calculated with basic calculation of longitudinal wave speed. Using the basic elastic wave speed for longitudinal wave speed, time for peak and base shock front to reach free surface can be calculated which is given by $t = \frac{x}{U_p}$, where $t$ is time, $x$ is the distance that shock front has travelled to reach the free surface, and $U_p$ is the particle velocity. Assuming pressure is equivalent to axial stress, the relationship between axial stress and $u_p$, $\sigma_{xx} = \rho\, U_s U_p$, where $U_s$ is the shock velocity and $\rho$ is the density of the material. Since $\sigma_{xx} \approx P$, $P = \rho\, U_s U_p = \rho\left(C_0 + s\, U_p\right)U_p$, where $C_0$ is the wave speed at zero pressure, $(P)$ is the applied pressure, and $s$ is the slope of $U_s - U_p$ curve.

The initial time difference ($\Delta t$) calculated using the calculated particle velocity for s25287, s25288, and s25289 are 2.15 ns, 2.93 ns, and 2.79 ns respectively. All three samples have the same initial perturbation amplitudes and wavelengths.

Table 6.3 provides the experimental and simulation time difference between the peak and base shock front to reach the free surface. Three different strengths were considered for the simulation results. Time difference, between peak and base shock front, to reach free surface decreases with increased strength and vice versa. Shock front takes some time to reach free surface and it is inversely proportional to the shock speed. Speed of the shock wave is dependent on material strength and applied pressure.

Table 6.3: Experimental and simulation results for the time difference for peak and base shock front to reach free surface. Simulation results are shown for three different strength levels.

| **Experimental and Simulated Δt** | | | | |
|---|---|---|---|---|
| **Shot #** | **Experimental Δt** | **Simulation time (Δt)** | | |
| | | **Baseline Strength** | **Increased Strength** | **Decreased Strength** |
| | **(ns)** | **(ns)** | **(ns)** | **(ns)** |
| **25287** | 2.1+/-0.05 | 2.3 | 1.9 | 2.7 |
| **25288** | 3.3+/-0.06 | 3.1 | 2.9 | 3.6 |
| **25289** | 2.8+/-0.05 | 2.6 | 2.2 | 3.4 |

This research work involves understanding hydrodynamic instability, which is obtained from an initially perturbed sample and it can be understood by studying the evolution of free surface profiles. Shock front that propagates from an initially perturbed sample, when reaches the free surface, imprints the perturbation. This imprinted perturbation on the free surface starts growing via hydrodynamic instability. Additionally, from figures 6.2-6.4, it is seen that the obliquity of the shock waves at left

(shock front under the initial surface perturbation valley) and right (shock front under the initial surface perturbation valley) leads to a higher stress at the center (shock front under the initial surface perturbation peak) of the rippled sample resulting in increase of both pressure and von Mises stress. However, this is not observed in the shock front that passes from a flat surface, which leads to a higher triaxiality than the perturbed one. Triaxiality study is performed to see this difference in flat and initially perturbed specimens.

The triaxiality of the stress state is known to greatly influence the amount of plastic strain that a material may experience before ductile failure occurs. Mathematically, triaxiality is defined as $\frac{\sigma_{hyd}}{\sigma_{eq}}$ where $\sigma_{hyd}$ is the hydrostatic stress and $\sigma_{eq}$ is the von Mises or equivalent stress.

Figures 6.17 and 6.18 show a countour plot of triaxiality for a perturbed and a flat sample where the perturbed sample is s25289 before shock breakout at 25 ns and at 40 ns (3.1 ns before shock breakout and 11.9 ns after shock breakout) simulation time. The flat sample is not the actual sample and is taken just for comparison. Sample thickness, loading and boundary conditions were kept constant and referred to the rippled specimen s25289. Both simulations were performed using baseline strength. Higher triaxiality corresponds to higher hydrostatic stress (or lower von Mises equivalent stress). From the contour plot, it can be seen that triaxiality for the perturbed sample is significantly smaller compared to an equivalent flat sample.

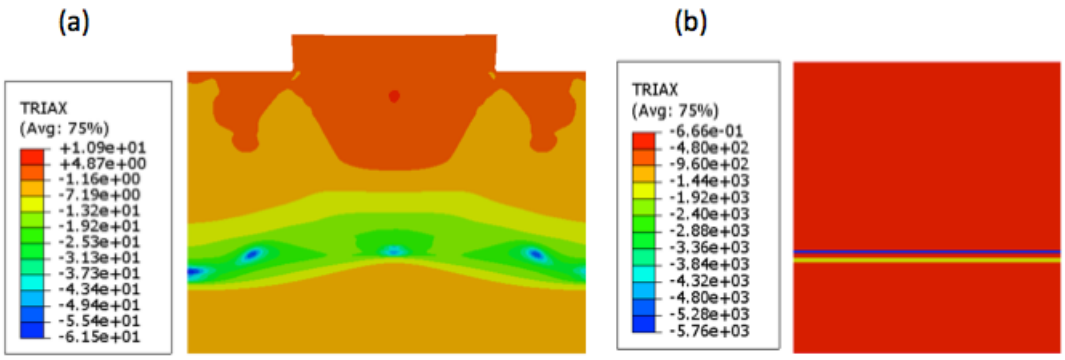


Figure 6.17. Triaxialities of (a) perturbed sample (s25289, 12.65 GPa) and (b) flat sample (12.65 GPa) at simulation time 25 ns (3.1 ns before shock breakout).

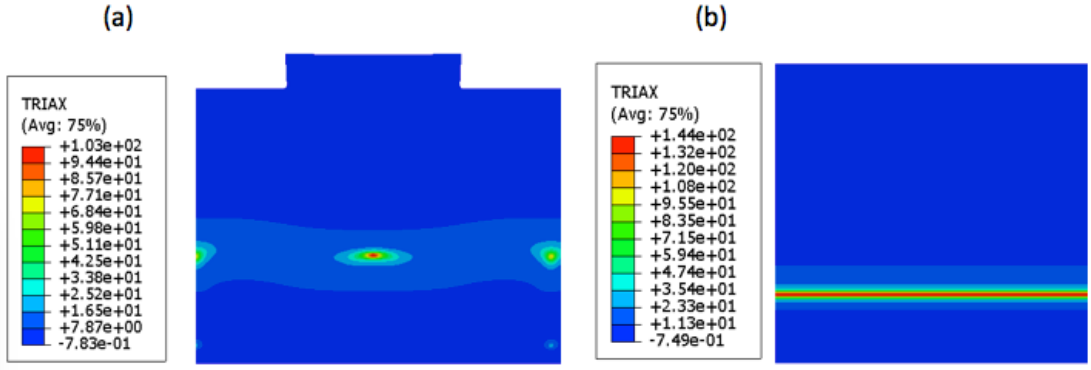


Figure 6.18. Triaxialities of (a) perturbed sample (s25289, 12.65 GPa) and (b) flat sample (12.65 GPa) at simulation time 40 ns (11.9 ns after shock breakout).

From all the results obtained from free surface profiles, it can be clearly seen that strength has significant effects on perturbation growth. Higher strength reduces the perturbation growth while lower strength amplifies it. Therefore, hydrodynamic instability growth can be controlled with material strength and since it should be possible to reduce significantly the perturbation growth by increasing the material strength. Also, material strength has an effect on second harmonics. Sometime after shock front breakout, the presence of second harmonics is seen, which is amplified by the material strength. This is clearly evident in the free surface profiles at steady state where the

higher strength has stronger second harmonics whereas lower strength show weaker presence of second harmonic. In some cases, when the surface profile was captured after 6.2 and 12.7 ns after the shock breakout, second harmonics were not even seen for the lower strength. Evolution of free surface profiles at different times indicated that at certain time after shock breakout, surface profile inverts itself and grows continuously. Also, the presence of second harmonics was seen during the inversion process. Applied pressure also had an effect on the perturbation growth where higher applied pressure increased the perturbation growth significantly.

All the samples simulated using the PTW model spall during experiments because the intensity of the laser pulse (pressure) was very high. In ductile fracture, the spallation process is controlled by localized plastic deformation. Spall damage is a plasticity-controlled phenomenon, and the dynamic plasticity of a material is affected by anisotropy and local plastic response. Many studies have been conducted to show that damage is driven by strain localization [5,57]. Recently, Krishnan [5] used a modified crystal plasticity framework with an added Gurson-Tvergard-Needleman (GTN) damage model to perform 3-D finite element simulations of spall damage in bicrystals and multicrystals of copper showing strain localization at and around grain boundaries that show damage. This research also performed an analysis of nucleation and early growth of spall damage of Krishnan's work [5] on shock loaded copper multicrystal. The details of this analysis are discussed in the next chapter.

# 7. ANALYSIS OF INCIPIENT SPALL DAMAGE

Krishnan [5] performed an analysis of incipient and intermediate spall damage, where he developed a physics based constitutive model to predict and characterize the influence of local microstructure on spall damage via microstructurally explicit simulations. He implemented crystal plasticity with a GTN damage model as the constitutive model for deviatoric and damage response, and a Mie-Grüneisen EOS for the volumetric response, via a user subroutine (VUMAT) in ABAQUS$^{TM}$/Explicit and used this model to predict early damage sites [5].

The main focus of this chapter is to provide in-depth analysis of the nucleation and early growth of spall damage for a shock loaded copper multicrystal, with emphasis on characterizing microstructural sites that are predicted to localize damage. This work is a continuation of Krishnan's work [5] on understanding and predicting the early stages of spall damage evolution. Spall damage nucleation and localization sites predicted by the microstructural explicit simulation performed by Krishnan [5] were examined to study the local parameters that lead to damage localization at those sites. The model predictions are then compared to experimental results.

As discussed in the introduction, the intrinsic microstructural features that tend to localize damage in pure polycrystalline metals are usually grain boundaries and triple joints [2,35,54]. Misorientation angle has been shown to have a significant effect on void nucleation at grain boundaries [35,53,54], but how this parameter might affect nucleation and growth of damage at triple junction still needs to be elucidated. Analysis of the simulation results obtained by Krishnan [5] on a copper multicrystal is performed here,

with emphasis on misorientation effects. The outcomes of this analysis are discussed in the next section.

## 7.1. Analysis of the Incipient Void Nucleation Sites at Triple Junctions

Krishnan set up a finite element model to simulate the traditional flyer-plate impact experiment of a copper multicrystal [5]. He reconstructed the 3-dimensional microstructure of multicrystalline sample to create this model from 20 different serial sectioned images spaced 50 μm between slices using AVIZO™ software. He then performed a finite element analysis on this 3-D reconstructed multicrystal using crystal plasticity with a modified GTN based damage model that he developed for the ABAQUS™/Explicit solver. Shock conditions used for the multicyrstal copper sample for finite element simulation performed by Krishnan [5] are provided in table 7.1. The first step on this stage of the research is to capture the phenomenon of spall damage at its incipient stage by examining contour plots of the fraction of nucleated voids, as predicted by the GTN damage model, at different times and finding the locations where these voids first nucleate by comparing the simulated sites to the experimental microstructure.

Table 7.1: Shock conditions for the copper multicrystal analyzed in [5].

| **Shock conditions for copper multicrystal** | | | | | | | | |
|---|---|---|---|---|---|---|---|---|
| **Shot #** | **Laser Energy** | **Pulse width** | **Flyer** | **Target** | **Max Pressure** | **Yield Strength** | **Spall Strength** | **Strain Rate** |
| | **(J)** | **(ns)** | **(mm)** | **(mm)** | **(Gpa)** | **(Mpa)** | **(Gpa)** | **(s-1)** |
| 19803 | 86 | 1250 | Cu (0.5) | Cu (1.0) | 3.56 | 100.7 | 1.64 | 1.92e5 |

The phenomenon of spall damage is captured at its early stage by plotting the volume fractions of nucleated voids after the release waves interact. Shock front breaks out during the simulation at 210 ns. Around 315 ns, (105 ns after the shock breakout), the release waves interact. Nucleated voids were clearly seen at around 360 ns, which is 45 ns after the release wave interaction. Iso-surface plots of volume fraction of nucleated voids were plotted at 360, 380, and 400 ns as shown in figure 7.1. Figure 7.1 shows that at 360 ns very few voids were nucleated and therefore, analysis of nucleated voids was done at 380 ns.

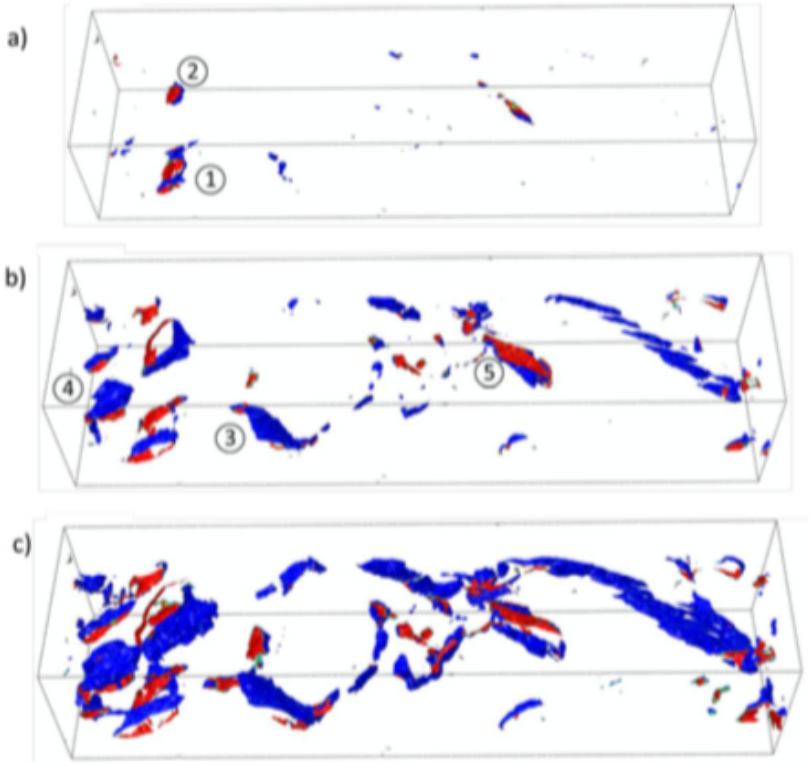


Figure 7.1. Iso-surface plot of void fraction at Time (a) 360 ns - incipient spall, (b) 380 ns - void nucleation, and (c) 400 ns – growth of nucleated voids [5].

The void distribution observed in the iso-surface plot is then compared to serial sectioned images by overlaying the iso-surface plot on the serial section slices used to create the 3-

D reconstruction. The overlaid images showed that the simulations predicted that voids nucleate predominantly at grain boundaries and triple junctions. Some of the examples of void nucleation sites found in the triple junctions are presented in figure 7.2. These nucleation sites are compared with the experimentally observed damage sites. Void nucleation sites from the simulation and the experimental damage sites are in the same locations.

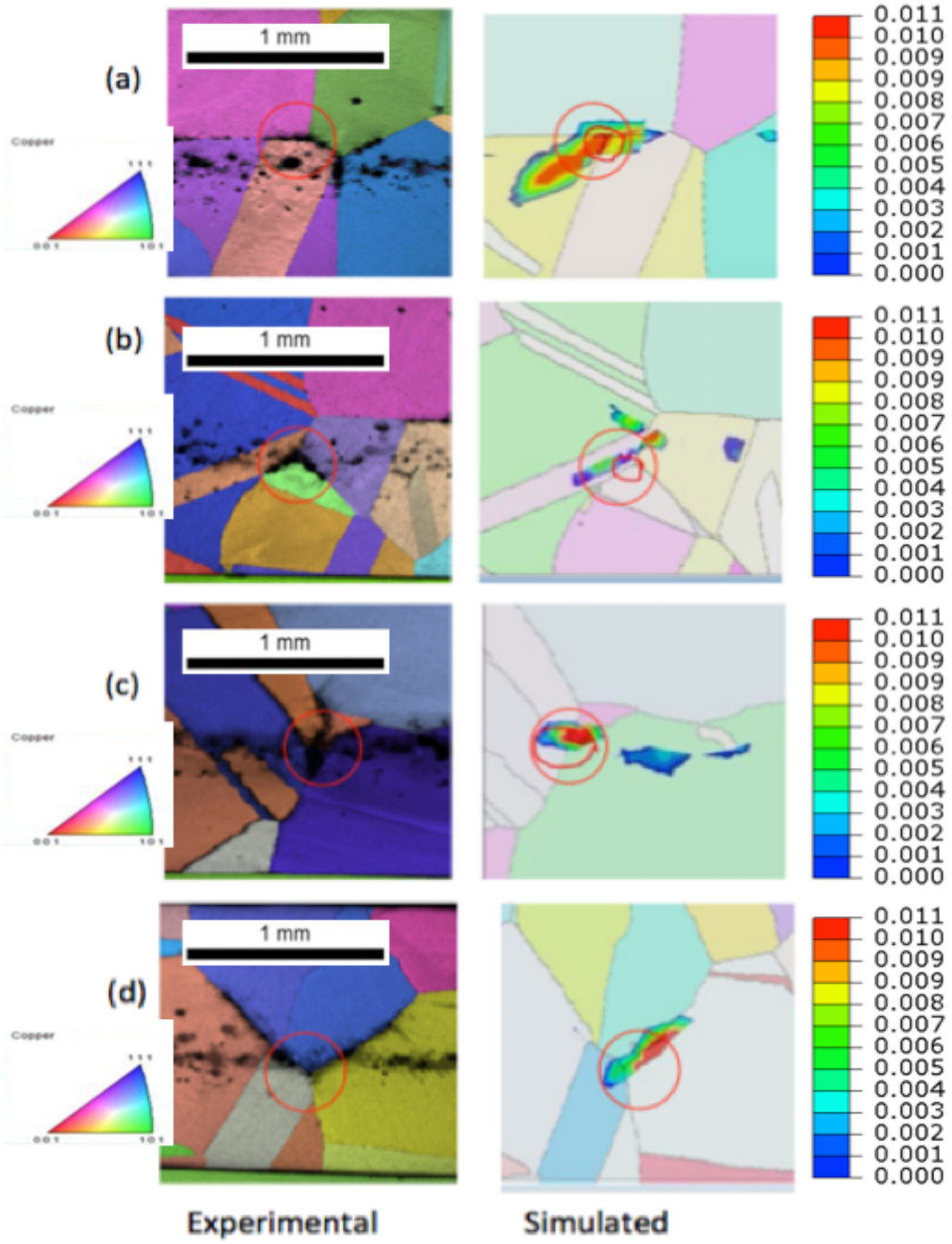


Figure 7.2. Comparison of experimental damage sites and finite element simulation nucleated voids showing that early nucleation is predicted to occur at triple junctions.

A total of 32 voids found at triple junctions at simulation time 360 and 380 ns were chosen for detailed examination. These 32 voids were chosen because they capture

the phenomenon of incipient spall damage. Table 7.2 shows the crystallographic characteristics of the microstructural sites at which the 32 different voids were found. In particular, given that these sites are triple junctions, axis/angle pairs are provided for each boundary connected to the triple junction, as well as the coincidence site lattice ∑ value of each boundary, if applicable.

Table 7.2: Misorientation angles and CSL features of selected void nucleation sites.

| Void # | Angle (Degrees)/axis pairs | | | Sigma | | Deviation | |
|---|---|---|---|---|---|---|---|
| | GB 1 to 2 | GB 2 to 3 | GB 3 to 1 | GB 1 to 2 | GB 2 to 3 | GB 1 to 2 | GB 2 to 3 |
| 1 | 58.9<br>[ -18, -18, 17 ] | 52.5<br>[ -19, -4, -22 ] | 28.5<br>[ 24, -13, 12 ] | 3 | | 1.7 | |
| 2 | 43.1<br>[22, 11, -8] | 42<br>[4, -22, 3] | 59.7<br>[ 1,1,1 ] | | | | |
| 3 | 59.6<br>[1, 1, -1] | 31.7<br>[-12, 1, 13] | 39.7<br>[-21, -2, 21] | 3 | 27a | 1 | 2.2 |
| 4 | 51.2<br>[14, 21, -9] | 52.4<br>[3, -22, 14] | 58.7<br>[13, 12, -13] | | | | |
| 5 | 53.6<br>[-14, -3, -16] | 58.9<br>[-17, -17, -18] | 40.6<br>[-9, 4, 4 ] | | 3 | | 1.9 |
| 6 | 59.6<br>[-18, 17, -17] | 40.3<br>[0, 19, 17] | 59.5<br>[17, 16, -18] | 3 | 9 | 0.9 | 2.5 |
| 7 | 52.6<br>[19, 4, -23] | 59.9<br>[1, 1, -1] | 40.3<br>[20, -9, 9] | | 3 | | 0.8 |
| 8 | 39.1<br>[-21, 22, 0] | 59.9<br>[1, -1, 1 ] | 35.2<br>[0, 7, -15 ] | 9 | 3 | 1 | 0.6 |
| 9 | 52.4<br>[18, 20, -3 ] | 59.9<br>[18, 17, -18 ] | 39.7<br>[-10, 7, 27 ] | | 3 | | 1.2 |
| 10 | 15.3<br>[-18, 11, 0 ] | 37.9<br>[-4, -3, -4 ] | 44.9<br>[-3, 14, 11 ] | | 7 | | 4.8 |
| 11 | 39.5<br>[19, -10, -17] | 40.3<br>[-17, -8, -23 ] | 53.2<br>[13, 15, -21 ] | | | | |
| 12 | 59.9<br>[18, -17, -18 ] | 41.8<br>[ 2, -9, -7 ] | 28.8<br>[20, -7, -1 ] | 3 | | 1.3 | |
| 13 | 38.2<br>[-13, 18, 17 ] | 60<br>[16, 17, 17 ] | 22.4<br>[11, 17, -13 ] | 7 | 3 | 4.9 | 1 |

| | | | | | | | |
|---|---|---|---|---|---|---|---|
| 14 | 31.8 | 59.7 | 48.2 | 5 | 3 | 5.1 | 0.7 |
| | [0, 1, 0 ] | [-1, -1, 1 ] | [25, 14, 3 ] | | | | |
| 15 | 47 | 39.8 | 50.8 | | | | |
| | [-8, 27, -9 ] | [-17, -8, -23 ] | [-3, -15, -14 ] | | | | |
| 16 | 59.2 | 23.1 | 36.8 | 3 | | 2.4 | |
| | [-13, -12, -13 ] | [14, 17, 21 ] | [-11, 16, 16 ] | | | | |
| 17 | 58.9 | 47.4 | 43.3 | 3 | | 3 | |
| | [10, -9, -10 ] | [-9, -21, 17 ] | [-8, 9, 6 ] | | | | |
| 18 | 30.3 | 59.9 | 48.5 | | 3 | | 1.8 |
| | [-2, 30, -3 ] | [16, 15, -15 ] | [11, 6, 2 ] | | | | |
| 19 | 60.2 | 55.7 | 34.2 | 3 | | 6.7 | |
| | [-12, 9, -10 ] | [10, -7, -15 ] | [26, 14, 1 ] | | | | |
| 20 | 53.5 | 17.6 | 59.8 | | | | |
| | [-23, 20, 1 ] | [-17, 21, -5 ] | [-1, -1, -1 ] | | | | |
| 21 | 59.8 | 49.2 | 28.1 | 3 | | 2.4 | |
| | [12, -11, 11 ] | [-18, -3, 10 ] | [12, 13, 24 ] | | | | |
| 22 | 60 | 36.5 | 44.5 | 3 | | 1.3 | |
| | [17, 17, -18 ] | [-6, 20, 7 ] | [27, 9, 1 ] | | | | |
| 23 | 59.6 | 51.9 | 21.3 | 3 | | 1.1 | |
| | [-16, 17, -17 ] | [15, -25, 9 ] | [ 20, 3, -1 ] | | | | |
| 24 | 58.9 | 34.1 | 39 | 3 | | 1.2 | |
| | [-1, 1, 1 ] | [ 11, -4, -9 ] | [-7, 22, -18 ] | | | | |
| 25 | 45.5 | 17.3 | 50.4 | | | | |
| | [3, -15, 20 ] | [-15, 18, -5 ] | [12, 13, -4 ] | | | | |
| 26 | 36.8 | 44.1 | 60 | | | | |
| | [-8, -7, 18 ] | [9, -14, 12 ] | [ 1,1,1 ] | | | | |
| 27 | 52.2 | 44.3 | 35.4 | | 37b | | 2.1 |
| | [7, 8, -1 ] | [26, -9, -1 ] | [6, -17, 22 ] | | | | |
| 28 | 60.7 | 43.8 | 50.6 | 43c | | 0.9 | |
| | [18, -19, -12 ] | [ 14, -20, 17 ] | [18, 19, -6 ] | | | | |
| 29 | 21.8 | 17.3 | 17.9 | 13a | 31a | 3.9 | 2.1 |
| | [-18, 1, 3 ] | [17, 15, 20 ] | [17, -4, -21 ] | | | | |
| 30 | 59.8 | 60.2 | 45.6 | 3 | 43c | 0.6 | 1 |
| | [-1, 1, -1 ] | [3, -2, -3 ] | [ 3, -16, 22 ] | | | | |
| 31 | 46.2 | 49.2 | 33 | | | | |
| | [-8, -16, 3 ] | [-8, -9, 2 ] | [-3, -8, 7 ] | | | | |
| 32 | 54.1 | 44.6 | 57.9 | | | | |
| | [21, 20, 2 ] | [17, 3, -24 ] | [-16, 20, 11 ] | | | | |

The number of sites collected is enough to quantify some meaningful statistics. In particular, given that high angle grain boundaries have been found to be preferred sites for spall damage nucleation [22], it would be interesting to see if this trend translates to the triple junctions identified here. In particular, the junctions were classified in terms of the number of high angle boundaries in them. Figures 7.3 and 7.4 show histogram plots produced by using the data from table 7.2.

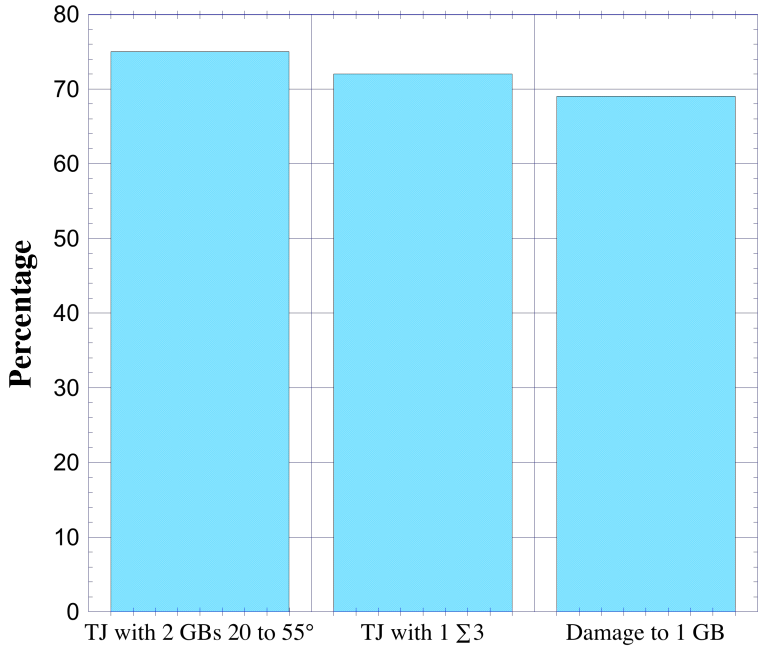


Figure 7.3. Characteristics of triple junctions where damage nucleated first according to the simulations.

From figure 7.3, it can be observed that voids nucleated largely at triple junctions primarily (75%) with two grain boundaries with misorientation angles ranging from $20° - 55°$, which is the same range shown to have high probability for have damage according to Wayne [22]. In addition, voids also nucleated often at triple junctions that had at least 1 $\sum 3$ grain boundary, i.e., a twin boundary. The simulations also showed that

voids nucleate at triple junctions and they tend to propagate preferentially into one of the boundaries connected to them. This is seen from the analysis of 32 voids nucleated at triple junctions and is represented in figure 7.3, where damage propagated largely (69%) to one preferential grain boundary after nucleating at triple junctions. Statistics of this damage propagated to a preferred grain boundary after nucleating at a triple junction are provided in figure 7.4 where the characteristics of these boundaries are also in qualitative agreement with polycrystal copper samples studied by Wayne [22] and Brown [58].

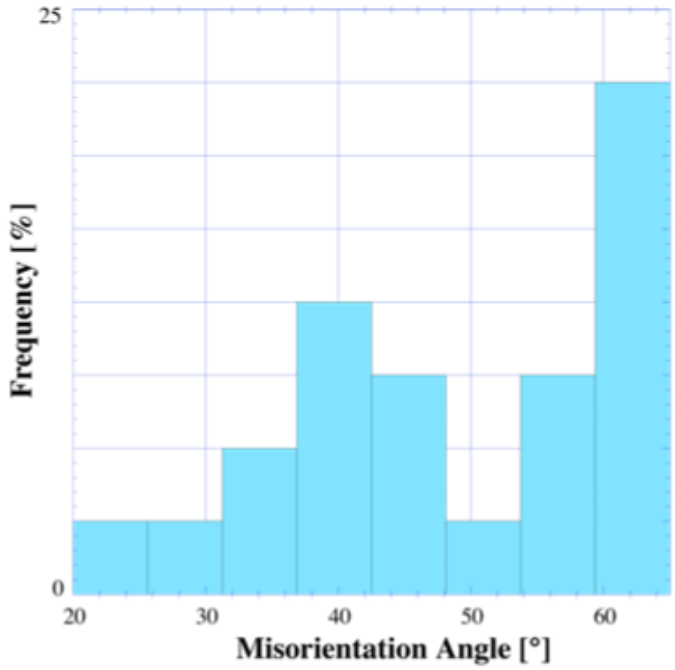


Figure 7.4. Frequency of misorientation angles of the boundaries into which damage was propagated after nucleating at triple junctions.

To better understand the void nucleation at triple junctions, the effect of triaxiality on the void nucleation and growth at the nucleation sites can be studied. Void growth can be enhanced by the superposition of hydrostatic and tensile stresses on a plastic deformation field [89-94]. Triaxiality plays a more significant role in void growth and

shape change in the early stages of plasticity. Therefore, stress triaxiality is one of the primary factors, besides strain sensitivity, that influences void growth. Calculated variables such as von Mises stress, pressure, equivalent plastic strain and triaxiality are studied to understand void nucleation and growth at triple junctions since it can be useful to understand why voids nucleated at these locations. These variables predicted by the simulation are studied here to try to find correlations between them and nucleation sites within the microstructure.

It is important to make a connection between the variables described above and the models used to predict damage. In that regards, since the GTN model is rate independent, Krishnan [5] used the yield surface for rate independent crystal plasticity as a plastic potential to incorporate the damage model into crystal plasticity. A damage parameter is used in this plastic potential to calculate the contribution of void volume fraction to the plastic strains which is given by [5]

$$D = 1 - \sqrt{1 + (q_1 f^*)^2 - 2q_{1f}^* \cosh\left(\frac{3}{2} q_2 T_x\right)} \tag{7.1}$$

where $D$ is the damage parameter, $f^*$ is void volume fraction, $q_1 \; and \; q_2$ are material parameters and $T_x$ is the stress triaxiality defined as $\frac{\sigma_{Hyd}}{\sigma_{eq}}$, $\sigma_{Hyd}$ is the hydrostatic stress and $\sigma_{eq}$ is the von Mises equivalent stress. Plastic strain increment applied in the crystal plasticity with added GTN damage model in the simulation is given by [5]

$$d\varepsilon^{p\alpha} = \frac{d\gamma^{\alpha} sym(\boldsymbol{s^{\alpha}} \otimes \boldsymbol{m^{\alpha}})}{1-D} + \frac{d\gamma^{\alpha}\left[f^* q_1 q_2 \sinh\left(\frac{3q_2 T_x}{2}\right)\sigma : sym(\boldsymbol{s^{\alpha}} \otimes \boldsymbol{m^{\alpha}})\right]}{2\sigma_y (1-D)^3} \tag{7.2}$$

where $\gamma^{\alpha}$ is the shear strain, $s^{\alpha}$and $m^{\alpha}$ are unit slip direction vector and unit normal vector to the slip plane respectively, $\sigma$ and $\sigma_y$ are Cauchy and yield stress respectively.

The first term in equation (7.2) is the contribution to the plastic strain increment by crystallographic slip and the second term is a volumetric damage strain increment from the contribution by voids formed under tension. From equation (7.1), we can say that increasing triaxiality, increases the damage parameter ($D$) and this damage parameter is very sensitive to stress triaxiality. Equation (7.2) provides the description used for the plastic strain increment, which can result in significant increase when the damage parameter ($D$) is increased, as can be seen in figures 7.5 and 7.6, which were obtained at 380 ns.

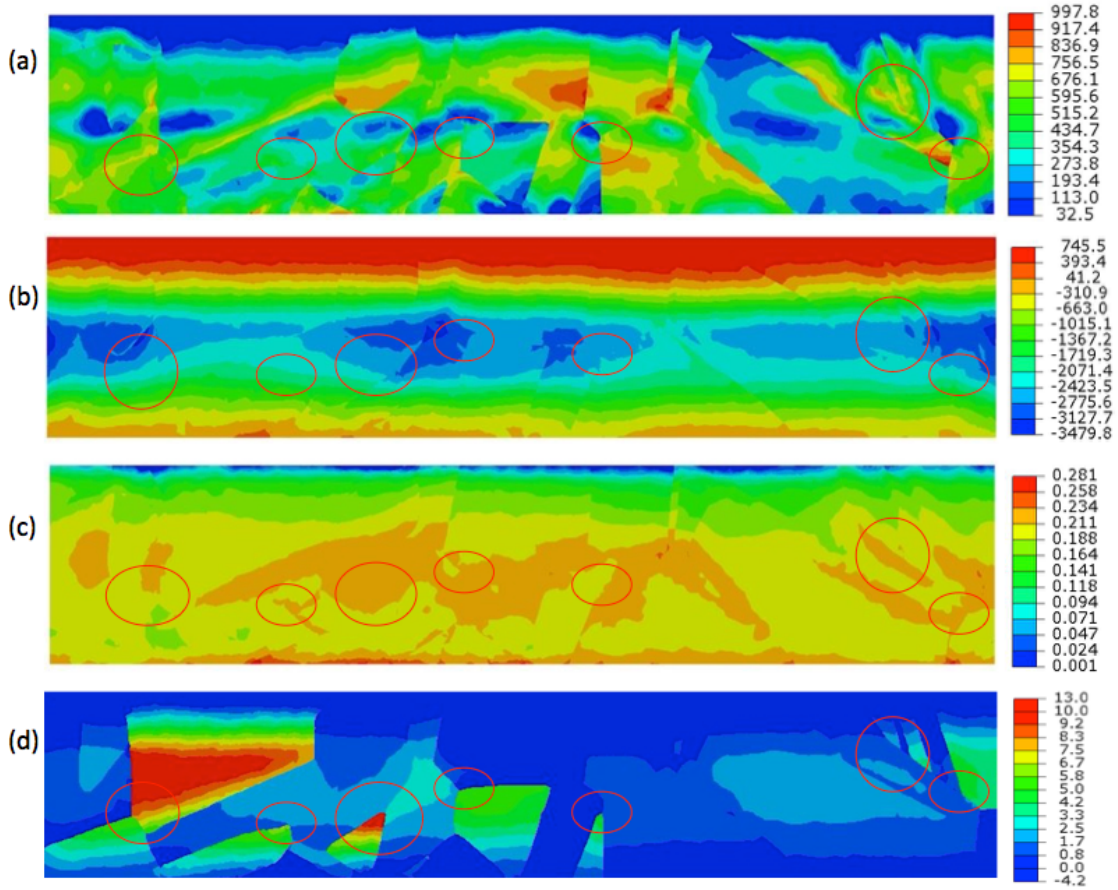


Figure 7.5. (a) von Mises stress, (b) pressure, and (c) equivalent plastic strain, and (d) stress triaxiality for a copper multicrystal. Circles in red represent the nucleation sites at triple junctions.

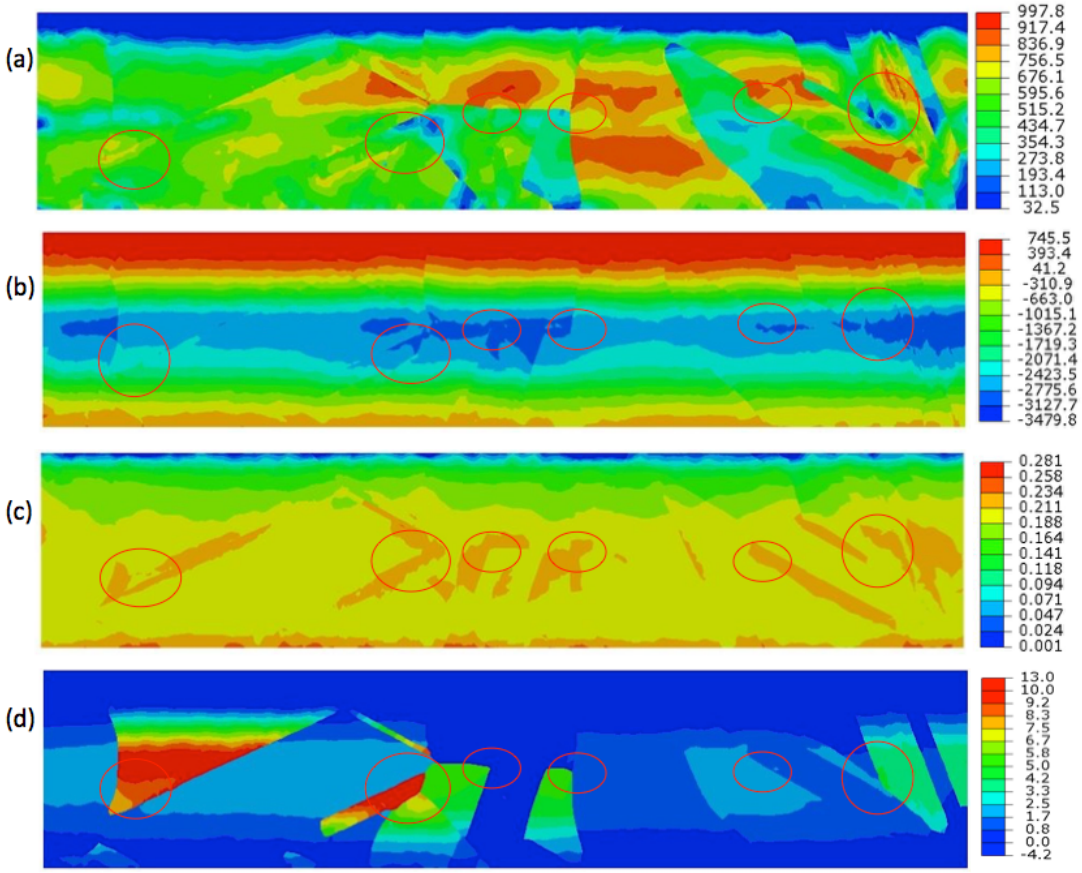


Figure 7.6. (a) von Mises stress, (b) pressure, and (c) equivalent plastic strain, and (d) stress triaxiality for a copper multicrystal. Circles in red represent the void nucleation sites at triple junctions.

In crystal plasticity, plastic strain rate is proportional to the deviatoric stress tensor and that von Mises provides the magnitude of it therefore increase in equivalent plastic strain increment can lead to the increase in von-Mises stress. This is seen in figures 7.5 and 7.6. As triaxiality is defined as pressure over von Mises stress, the higher value of pressure leads to a higher value of triaxiality, which is also seen in figures 7.5 and 7.6. Krishnan [5] used a model where void nucleation and growth criteria are updated from the plastic strain increment (Equation (7.2)) and is given by [5]

$$df_{nuc} = \left[\left(\frac{f_N}{s_N\sqrt{2\pi}}\right)\exp\left(-\frac{1}{2}\left(\frac{\varepsilon_{eq}^{p}-e_N}{s_N}\right)^2\right)\right] d\varepsilon_{eq}^{p} \tag{7.3}$$

$$df_{gr} = (1 - f^*)d\varepsilon_{kk}^p \tag{7.4}$$

where $f_N, s_N,$ and $e_N$ are statistical strain measurements pertaining to void nucleation and equivalent plastic strain increment. We can see from equations (7.3) and (7.4) that void nucleation is associated to equivalent plastic strain increment and void growth is associated to mean plastic strain increment and void volume fraction, both sensitive to triaxiality as per equations (7.1) and (7.2). Hence, high stress triaxiality can result in increase of equivalent plastic strain increment, which is seen in the microstructural features such as triple junctions in figures 7.5 and 7.6.

The stress triaxiality predicted by the simulation is studied here to try to find correlations between that parameter and nucleation sites within the microstructure. Figures 7.7 and 7.8 are captured at 380 ns when the voids are nucleated and are growing towards s preferentially oriented grain boundary. These figures show that the high stress triaxiality is found around the triple junctions where the voids have already been nucleated - representing the growth of these voids. These locations were then compared to EBSD scanned images with damage sites and the results are in agreement with the observed damage sites.

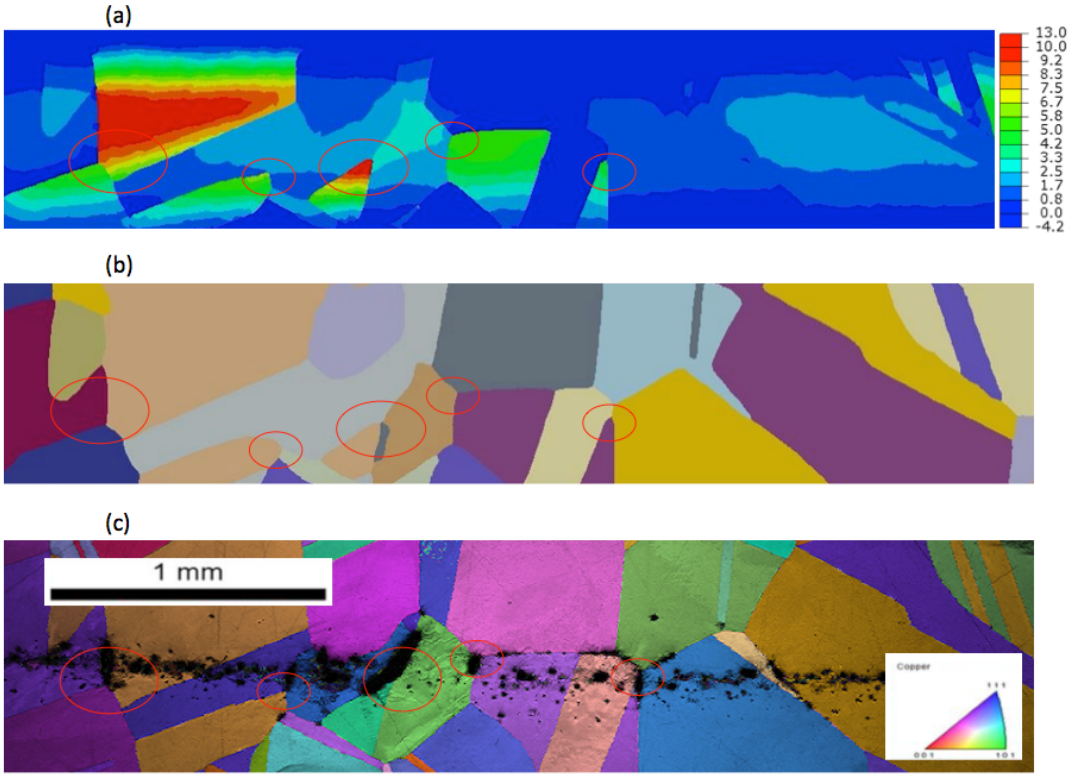


Figure 7.7. (a) Stress triaxiality for a copper multicrystal, (b) microstructure images without damage, and (c) EBSD scan image of damage sites. Circles in red represent the void nucleation sites at triple junctions.

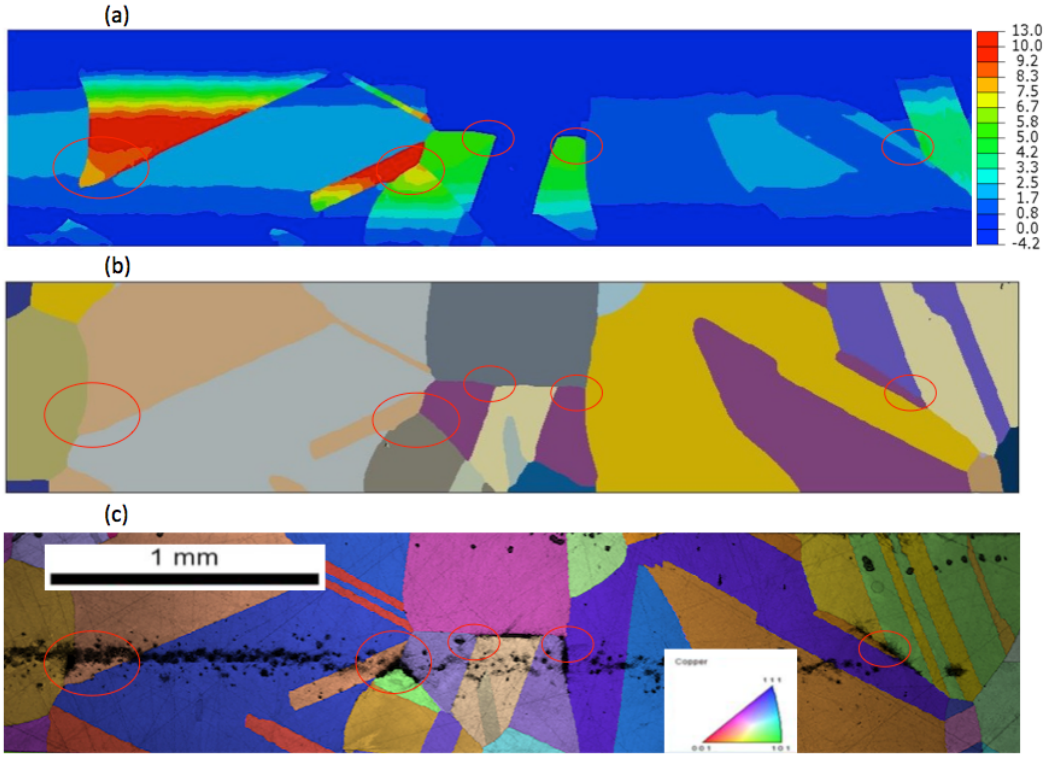


Figure 7.8. (a) Stress triaxiality for a copper multicrystal, (b) microstructure images without damage, and (c) EBSD scan image of damage sites. Circles in red represent the void nucleation sites at triple junctions.

Analysis done on void nucleation at triple junctions show similar trends as the statistical analyses performed by Wayne [22] and Brown [58] for copper polycrystal. Microstructural features that have a high degree of influence on the damage nucleation were found to be triple junctions and misorientation angles associated to them. In triple junctions, damage nucleate due to very high strain localization at the junction. Analysis performed on the voids nucleated at triple junctions show that misorientation angles between $20° - 55°$ have high probability of damage. Additionally, triple junctions with twin boundaries were often observed as void nucleation sites. Furthermore, it was also seen that damage propagates to a preferential grain boundary after nucleating at the triple

junctions and the statistics of those grain boundaries are also in agreement with statistical analyses performed by Wayne [22] and Brown [58] for spalled copper polycrystals.

# 8. CONCLUSIONS

The finite element simulations performed to study strength effects on the RM hydrodynamic instability, and to gather statistics on the characteristics of void nucleation sites of copper multicrystals, along with comparisons with experimental data for both cases, lead to the following conclusions:

[1] An isotropic, hypoelastic constitutive formulation was used for the deviatoric response of copper under shock loading based on the PTW strength model and the Mie-Grüneisen EOS for the volumetric response. This constitutive framework was implemented as a user subroutine in ABAQUS$^{TM}$/Explicit to perform simulations to study strength effects on the RM hydrodynamic instability.

[2] The material constants for the PTW model used in the constitutive framework were calibrated using parametric sweeps and optimal values were determined that were best fits to the shock compression loading and initial release portions of experimental velocity histories of flat samples obtained using VISAR. To calibrate the PTW parameters, initially, a comparison of experimental and simulated velocity profiles was done, which showed that the simulation result varied during the initial shock compression loading and initial release. Key PTW parameters such as strain hardening constant $(p)$, yield stress factors at zero and very high temperature ($y_0$ and $y_\infty$) and medium strain hardening constant ($y_2$) were changed to get a better agreement ($R^2 \approx 1$) between simulation and experimental results. The change in these parameters increased the strength dependence on strain rate and plastic strain. Also, discrepancy at the second half of the release between the experimental and simulation result was seen, which was due to the tensile stresses leading to spallation, which was not incorporated into the model.

[3] A relationship between the pressure pulse history at the loading surface and laser energy used during the experiments was also obtained. This relationship was well-ditted by a quadratic polynomial and was useful in obtaining the pressure boundary condition needed for simulation.

[4] The validation of the constitutive model was done by comparing the simulation results with experimental TIDI results for rippled (perturbed) samples. Finite element simulation results show that they are within the experimental error except for the one case where the difference was 20%. This error was found 12.7 ns after shock breakout, which suggested that spallation might have occurred due to the tensile stresses generated by the interaction of two release waves since 12.7 ns provides enough time for spallation to occur.

[5] The shock front was perturbed due to the initial perturbation present in the ablated surface of the sample. The shock front coming from the peak of the surface perturbation was behind the shock front coming from the valley, which created the difference in time for peak and base shock front to reach the free surface.

[6] The effect that strength has on the continuum material response and hydrodynamic instability growth was studied through a set of parametric simulations with different levels of strength response. The results showed clearly that evolution of hydrodynamic instabilities can be affected by material strength from the increase and decrease in amplitude with the level of strength.

[7] Clear differences between sine and square waves has effect in the amplitude growth were found. For the same amplitude and wavelength, a pure sine wave will grow less than a square wave for the same driving force. This is explained by Fourier mode

interpretation where each mode of square wave grows according to its own scaling law and adds to the total, whereas a sine wave has a single mode, hence, a single contribution to the amplitude growth.

[8] Presence of higher harmonics both in experimental and simulation results was seen at certain time after the shock breakout. Higher strength amplified the second harmonic whereas lower strength decreased it, which indicated a clear effect of strength on the presence of the second harmonic.

[9] Analysis of void nucleation was performed based on results from a microstructurally explicit simulation of spall damage evolution in a multicrystalline copper sample. Results from the simulations indicate that triple junctions are the preferred sites for early damage nucleation.

[10] Analysis of crystallographic characteristics of triple junctions where simulations showed early damage nucleation was performed using existing experimental data. This analysis revealed that a high percentage of them (75%) had at least two-grain boundaries with misorientation angles between 20 and 55°. Additionally, triple junctions with twins are often associated to void nucleation. The statistical results performed on the void nucleation are in agreement with Wayne's [22] statistical analysis performed on copper polycrystals, which suggests that the nature of the boundaries connecting at a triple junction seems to be an indicator for their tendencies to localize spall damage.

[11] Simulations also showed that after nucleating at a triple junction, damage typically propagated preferentially into one of the boundaries connected to the triple junction. Statistics on the crystallographic characteristics of those boundaries also show the similar trends found in Wayne's [22] result for copper polycrystal, where higher

frequency of the damage propagated to the grain boundary with misorientation angle between 20 to 55°.

# 9. FUTURE WORK

[1] Further refinement of the finite element simulation, adding a damage aware model to the PTW model would help better understand the spallation process during the shock loading. Adding the damage to the PTW model will help calibrate and validate the model more accurately as spallation occurs during the experiment.

[2] Hydrodynamic instability studies in copper polycrystal are not able to elucidate the mechanisms for perturbation growth in anisotropic materials. Studies on the effect of hydrodynamic instability on anisotropic copper rippled samples will provide a better understanding of microstructural heterogeneity and anisotropy and their effects on the growth of hydrodynamic instabilities.

[3] Simulation and experiments on rippled samples with different wavelength and amplitudes can be performed, which would help to understand effects of these parameters on hydrodynamic instability growth.

[4] Simulation and experiments on perturbed samples can be performed varying the thickness of the specimen and keeping the laser energy constant. This would help better understand the effect of sample thickness in the growth of hydrodynamic instability and on the effects of strength on the amplitude of the perturbed shock front as it arrives at the free surface.

REFERENCES


1. “Advanced Simulation and Computing and Institutional R & D Programs”. National Nuclear Security Administration, n.d. Web. 21 Mar. 2016]

2. Meyers, M.A., Dynamic Behavior of Materials. 1994, New York: John Wiley & Sons, Inc.

3. Hashemian, S., S. DiGiacomo, P. Peralta, H. D'Armas, S.-N. Luo, E. Loomis, D.L. Paisley, R. Dickerson, D. Byler, and K.J. McClellan. Effects of Microstructure on Spall Damage Localization in Shock Loaded Copper Multicrystals. in TMS Annual Meeting. 2008. New Orleans, LA: TMS.

4. Peralta, P., et al., Characterization of Incipient Spall Damage in Shocked Copper Multicrystals. Int. J. Damage Mechanics, 2009(18): p. 393-413.

5. Krishnan, K., 3D Modeling of Incipient Spall Damage in Shocked FCC Multicrystals , PhD Thesis in Mechanical and Aerospace Engineering 2013, Arizona State University: Tempe,AZ.

6. S. Atzeni, J. Meyer-ter-Vehn, “The Physics of Inertial Fusion: BeamPlasma Interaction, Hydrodynamics, Hot Dense Matter: BeamPlasma Interaction, Hydrodynamics, Hot Dense Matter,” Vol. 125. Oxford University Press, 2004

7. N. Barton, J. Bernier, et. al., "A multiscale strength model for extreme loading conditions," J. of App. Phys, 2011, 109.

8. J.F. Barnes, P.J. Blewett, R.G. McQueen, “Taylor instability in solids,” J. App. Phys., 1974, 45:727-732.

9. A.R. Piriz, J.J. Lopez, O.D. Cortazar, “Rayleigh-Taylor instability in elastic solids,” Phys. Rev. E, 2005, 72:056313.

10. A.R. Piriz, J.J. Lopez, N.A. Tahir, “Rayleigh-Taylor instability in elastic-plastic solids,” J. App. Phys., 2009, 105:116101.

11. H. Park, B.A. Remington, et. al., "Strong stabilization of the Rayleigh-Taylor instability by material strength at megabar pressure," Physics of Plasmas, 2010, 17.

12. G. Dimonte, C.E. Frerking, M. Schneider, B. Remington, “Richtmyer-Meshkov instability with strong radiatively driven shocks,” Phys. Plasmas, 1996, 3:614-630.

13. A.R. Piriz, J.J. Lopez, N.A. Tahir, “Richtmyer-Meshkov instability as a tool for evaluating material strength under extreme conditions,” Nuclear Instr. and Meth. in Phys. Research, 2009, 606:139-141.

14. A.R. Piriz, J.J. Lopez, “Richtmyer-Meshkov instability in elastic-plastic media,” Phys. Rev. E, 2008, 78:056401.

15. G. Dimonte, G. Terrones, F.J. Cherne, et. al., “Use of the Richtmyer-Meshkov Instability to Infer Yield Stress at High-Energy Densities,” Phys. Rev. Lttrs., 2011, 107:264502.

16. Y. Aglitskiy, M. Karasik, A.L. Velikovich, et. al., “Observed transition from Richtmyer-Meshkov jet formation through feedout oscillations to Rayleigh-Taylor instability in a laser target,” Phys. Of Plasmas, 2012, 19:102707.

17. W.T. Buttler, D.M. Oro, et. al., “Unstable Richtmyer-Meshkov growth of solid and liquid metals in vacuum,” J. Fluid Mech., 2012, 703:60-84.

18. P. Peralta, E. Loomis, et. al., "Grain orientation on dynamic strength of FCC multicrystals at low shock pressures: a hydrodynamic instability study," Phil. Mag. Letters, 2015, 95:67-76.

19. Martineau, R.L., A Viscoplastic Model of Expanding Cylindrical Shells Subjected to Internal Explosive Detonations, 1998.

20. DiGiacomo, S., Characterization Of Plasticity And Damage In Shock Loaded Copper At Various Microstructural Length Scales, MS Thesis in Mechanical and Aerospace Engineering, 2008, Arizona State University: Tempe, AZ.

21. Meyers, M.A., A model for Elastic Precursor Waves in the Shock Loading of Polycrystalline Materials. Mater. Sci. Eng., 1977. 30(2): p. 99-111.

22. Wayne, L., Three Dimensional Characterization of Spall Damage at Microstructural Weak Links in Shock-Loaded Copper Polycrystals, MS Thesis in Mechanical and Aerospace Engineering2009, Arizona State University: Tempe,AZ.

23. Loomis, E., P. Peralta, and D.C. Swift, Modeling of Elastic Waves in Dynamically Loaded NiAl Bicrystals. J. Eng. Mat. Tech., 2007. 129: p. 513-522.

24. Graef, M.D. and M.E. McHenry, Structure of Materials: An Introduction to Crystallography, Diffraction, and Symmetry. 2007, New York: Cambridge.

25. Loomis, E., The Effect of Grain Boundaries on the Deformation Mechanisms of Nickel Aluminide During Laser-Induced Shock Loading, PhD Thesis in Mechanical and Aerospace Engineering 2005, Arizona State University: Tempe. p. 255.

26. Antoun, T., et al., Spall Fracture. 2002, New York: Springer.

27. R. Kinslow, High velocity impact phenomena (Academic Press, New–York/London, 1971)

28. E.N. Loomis, S.R. Greenfield, R.P. Johnson, et. al., "Investigations into the seeding of instabilities due to x-ray preheat in beryllium-based inertial confinement fusion targets," Phys. Of Plasmas, 2010, 17:056308.

29. Isbell, W.M., Measuring the Dynamic Response of Materials. 2005, London: Imperial College Press

30. Stevens, A.L., L. Davison, and W.E. Warren, Spall Fracture in Aluminum Monocrystals: A Dislocation-Dynamics Approach. J. Appl. Phys., 1972. 43(12): p. 4922-4927.

31. E.N. Loomis, "LANL/ASU Summit on Richtmyer-Meshkov Strength Project," LANL, 2014, LA-UR-14-21052.

32. Luo, S.N., et al., High Pressure Research, 2004. 24: p. 409.

33. Cochran, S. and D. Banner, Spall Studies in Uranium. J. Appl. Phys., 1977. 48.

34. Follansbee, P.S. and U.F. Kocks, A Constitutive Description of the Deformation of Copper Based on the use of Mechanical Threshold. Acta Metallurgica, 1988. 36: p. 81-93.

35. Johnson, G.R. and W.H. Cook. A Constitutive Model and Data for Metals Subjected to Large Strains, High Strain Rates and High Temperatures, in Proceedings of the 7th International Symposium on Ballistics. 1983.

36. Khan, A.S. and R.Q. Liang, Behavior of Three BCC Metals over Wide Range of Strain Rates and Temperatures: Experiments and Modeling. International Journal of Plasticity, 1999. 15: p. 1089-1109.

37. Steinberg, D.J., S.G. Cochran, and M.W. Guinan, A Constitutive Model for Metals Applicable at High-Strain Rate. J. Appl. Phys., 1980. 51(3): p. 1498-1504.

38. Steinberg, S.E. and C.M. Lund, A Constitutive Model for Strain Rates from $10^4$ to $10^6$ $s^{-1}$. Journal de Physique Colloques, 1988. 49.

39. Zerilli, F.J. and R.W. Armstrong, Dislocation-Mechanics-Based Constitutive Relations for Material Dynamics Calculations. J. Appl. Phys, 1987. 61: p. 1816-1825.

40. Bodner, S.R. and Y. Partom, Constitutive equations for elastic-viscoplastic strain-hardening materials. Journal of Applied Mechanics, 1975: p. 385-389.

41. Dean L. Preston, Davis L. Tonks, and Duane C. Wallace, Model of plastic deformation for extreme loading conditions. Journal of Applied Physics 93, 211 (2003); doi: 10.1063/1.1524706

42. M.C. Price, A.T. Kearsley, M.J. Burchell, Validation of the Preston-Tonks-Wallace strength model at strain rates approaching $\sim 10^{11}$ $s^{-1}$ for Al-1100, tantalum and copper using hypervelocity impact crater morphologies. International Journal of Impact Engineering 52 (2013) 1-10

43. Davidson RF, Walsh ML. Constitutive modeling for hypervelocity cratering. Proceeding of the APS meeting on the Shock Compression of Condensed Matter (Los Alamos National Laboratory report # LA-UR-95e2746); 1995.

44. E. Voce, J. Inst. Met. 74, 537 1947/48.

45. D. C. Wallace, Irreversible Thermodynamics of Overdriven Shocks in Solids, Phys. Rev. B 24, 5597 1981.

46. D. C. Wallace, Nature of the Process of Overdriven Shocks in Metals, Phys. Rev. B 24, 5607 1981.

47. R. O. McQueen and S. 1'. Marsh, Ultimate Yield Strength of Copper, J. Appl. Phys. 33.654 (1962)

48. G. Terrones, "Fastest growing linear Rayleigh-Taylor modes at solid/fluid and solid/solid interfaces," Phys. Rev. Lttrs, 2005, 71:036306.

49. J. Forbes, "Shock Wave Compression of Condensed Matter," Springer, 2012.

50. A.R. Piriz, J.J. Lopez, "Comment on Viscous Rayleigh-Taylor Instability Experiments at High Pressure and Strain Rate," Phys. Rev. Lttrs., 2010, 179601.

51. V.V. Burtsev, A.I. Lebedev, A.L. Mikhailov, et. al., "Use of Multiframe Proton Radiography to Investigate Fast Hydrodynamic Processes," Combustion, Explosion, and Shock Waves, 2011, 47:627-638.

52. J.L. Belof, R.M. Cavallo, et. al. "Rayleigh-Taylor Strength Experiments of the Pressure Induced Phase Transition in Iron," LLNL-PROC-492911, 2011.

53. A.L. Ortega, M. Lombardini, D.I. Pullin, D.I. Meiron, "Numerical simulation of the Richtmyer-Meshkov instability in solid-vacuum interfaces using calibrated plasticity laws," Phys. Rev. Lttrs. E., 2014, 89:033018.

54. K. T. Gahagan, D. S. Moore, D. J. Funk, J. H. Reho, and R. L. Rabie, "Ultrafast interferometric microscopy for laser-driven shock wave characterization" Journal of Applied Physics 92, 3679 (2002).

55. S. R. Greenfield, D. C. Swift, and A. C. Koskelo, "Transient Interferometric Studies of Shocked Bicrystals", AIP Conference Proceedings 706, 1269 (2004).

56. Scott R. Greenfield , Joanna L. Casson and Aaron C. Koskelo "Nanosecond interferometric studies of surface deformations of dielectrics induced by laser irradiation", Proc. SPIE 4065, High-Power Laser Ablation III, 557 (August 16, 2000).

57. Krishnan, K., A. Brown, L. Wayne, J. Vo, S. Opie, H. Lim, P. Peralta, S.N. Luo, D. Byler, K.J. McClellan, A. Koskelo, R. Dickerson, Three-Dimensional Characterization and Modeling of Microstructural Weak Links for Spall Damage in FCC Metals. Metall. and Mat. Trans A., 2014.

58. Brown., Three Dimensional Characterization of Microstructural Effects on Spall Damage in Shocked Polycrystalline Copper, PhD Thesis in Mechanical and Aerospace Engineering 2015, Arizona State University: Tempe,AZ.

59. R. O. McQueen and S. 1'. Marsh, J. Appl. Phys. 33.654 (1962)

60. R. C. Skidmore. Appl. Mater. Res.4, 131 (1965) and B, R. Breed. C. L. Mader. and D. Venable, J. App!. Phys. 38. 3271 (1967)

61. Wayne, L., et al., Statistics of Weak Grain Boundaries for Spall Damage in Polycrystalline Copper. Scripta Materialia, 2010. 63: p. 1065-1068.

62. Curran, D.R., L. Seaman, and D.A. Shockey, Dynamic Failure of Solids. Phys. Reports, 1987. 147(5-6): p. 253-388.

63. Meyers, M.A. and C.T. Aimone, Dynamic Fracture (Spalling) of Metals. Prog. Mat. Sci., 1983. 28: p. 1-96.

64. Cao, F., et al., Orientation dependence of shock-induced twinning and substructures in a copper bicrystal. Acta Materialia, 2010. 58: p. 549-559.

65. Chen, X., et al., Spall Behavior of Aluminum with Varying Microstructures. J. Appl. Phys., 2006. 99: p. 1-13.

66. Escobedo, J.P., et al., Effects of grain size and boundary structure on the dynamic tensile response of copper. Journal of Applied Physics, 2011. 110(3).

67. Minich, R.W., et al., Effect of Microstructural Length Scales on Spall Behavior of Copper. Metall. Mater. Trans. A, 2004. 35A: p. 2663-2673.

68. Vignjevic, R., et al., Effects of Orientation on the Strength of the Aluminum Alloy 7010-T6 During Shock Loading: Experiment and Simulation. J. Appl. Phys., 2002. 92(8): p. 4342-4348.

69. Henrie, B.L., T.A. Mason, and J.F. Bingert. Investigating Incipiently Spalled Tantalum Through Multiple Section Planes and Serial Sectioning in Shock Compression of Condensed Matter 2005. 2005. American Institute of Physics.

70. Brown, A.D., L. Wayne, Q. Pham, K. Krishnan, P. Peralta, S.N. Luo, B. Patterson, S. Greenfield, D. Byler, K.J. McClellan, A. Koskelo, R. Dickerson, X. Xiao, Microstructural Effects on Damage Nucleation in Shock-Loaded Polycrystalline Copper. Metall. and Mat. Trans A., 2015.

71. ABAQUS, ABAQUS Documentation, 2012, Dassault Systèmes, Providence, RI, USA.

72. ABAQUS, Abaqus Theory Manual, 2010.

73. Czarnota, C., et al., Modeling of Dynamic Ductile Fracture and Application to the Simulation of Plate Impact Tests on Tantalum. J. Mech. Phys. Sol., 2008. 56: p. 1624-1650.

74. Barbee Jr., T.W., et al., Dynamic Fracture Criteria for Ductile and Brittle Materials. Journal of Material Science, 1972. 7(3): p. 393-401.

75. Grady, D.E., The Spall Strength of Condensed Matter. J. Mech. Phys. Sol., 1988. 36(3): p. 353-384.

76. Gray, G.T., et al. Influence of Shock-Wave Profile Shape ("Taylor-Wave Versus Square-Topped) on the Shock-Hardening and Spallation Response of 316L Stainless Stell. in Shock Compression of Condensed Matter 2003. 2003. American Institute of Physics.

77. Czarnota, C., S. Mercier, and A. Molinari, Modelling of Nucleation and Void Growth in Dynamic Pressure Loading, Application to Spall Test on Tantalum. Int. J. Fract., 2006. 141: p. 177-194.

78. P.M. Pinsky, M. Ortiz, K.S. Pister, "Numerical Integration of Rate Constitutive Equations in Finite Deformation Analysis," Comp Meth. App. Mech. Eng, 1983, 40:137-158.

79. H. Xiao, O. T. Bruhns, A. Myers, "Existence and uniqueness of the integrable-exactly hypoelastic equation $\tau = \lambda trDI + 2\mu D$ and its significance to finite elasticity," Acta Mech., 1999, 138:31-50.

80. Meyers, H. Xiao, O Bruhns, "Elastic Stress Ratchetting and Corotational Stress Rates," Technische Mechanik, 2003, 23:92-102.

81. R. Lin, "Numerical study of consistency of rate constitutive equations with elasticity at finite deformation," Int. J. Num. Meth. Eng., 2003, 55:1053-1077.

82. J. C. Simo, K. S. Pister, "Remarks on Rate Constitutive Equations for Finite Deformation Problems: Computational Implications," Comp. Meth. App. Mech. Eng., 1984, 46:201-215.

83. EA de Souza Neto, D Peric´ , DRJ Owen, “Computational Methods For Plasticity, Theory And Applications” Civil and Computational Engineering Centre, Swansea University, John Wiley and Sons, 2011.

84. Cerreta, E.K., et al., Early stage dynamic damage and the role of grain boundary type. Scripta Materialia, 2012. 66(9): p. 638-641.

85. Papoulis, A. and S.U. Pillai, Probability, Random Variables and Stochastic Processes. 4th ed. 2002: McGraw Hill.

86. Gleiter, H. and B. Chalmers, High-angle grain boundaries. Progress in Materials Science, 1971. 16: p. 77.

87. J. A. Nucci, et al., Grain boundary misorientation angles and stress-induced voiding in oxide passivated copper interconnects. Applied Physics Letters, 1997. 70: p. 1242.

88. Sutton, A. P. and Ballufi, R. W, “Interfaces in Crystalline Materials,” Vol. 119. New York, Oxford University Press, 1995

89. J. Rice, D. Tracey, On the ductile enlargement of voids in triaxial stress fields, J. Mech. Phys. Solids 17 (3) (1969) 201–217.

90. E. Seppala, J. Belak, R. Rudd, Effect of stress triaxiality on void growth in dynamic fracture of metals: a molecular dynamics study, Phys. Rev. B 69 (13) (2004)

91. Atkins, Fracture in forming, J. Mater. Process. Technol. 56 (1–4) (1996) 609–618.

92. Atkins, Fracture mechanics and metalforming: damage mechanics and the local approach of yesterday and today, Fracture research in retrospect: an anniversary volume in honour of George R. Irwin’s 90th birthday, 1997, 327.

93. M. Oyane, T. Sato, K. Okimoto, S. Shima, Criteria for ductile fracture and their applications, J. Mech. Working Technol. 4 (1) (1980) 65–81.

94. P. Brozzo, B. Deluca, R. Rendina, A new method for the prediction of the formability limits of metal sheets, in: Proceedings of the 7th Biennial Congress of International Deep Drawing Research, Group, 3–1, 1972.

95. J. Lindl, Development of the Indirect-Drive approach to Inertial Confinement Fusion and the Target Physics Basis for Ignition and Gain, Phys. Plasmas, 2 (1995) 3933-3982.

96. F. Addessio, Q. Zuo, T. Mason, "Model for high-strain-rate deformation of uranium-niobium alloys," J. App. Phys., 2003, 93:9644-9654.